Technical Physics Letters, Vol. 28, No. 12, 2002, pp. 1001–1003. Translated from Pis'ma v Zhurnal Tekhnicheskoĭ Fiziki, Vol. 28, No. 23, 2002, pp. 58–62.
Original Russian Text Copyright © 2002 by Aĭdaraliev, Zotova, Karandashev, Matveev, Remennyĭ, Stus', Talalakin, Shustov.

Two-Wavelength Emission from a GaInPAsSb/InAs Structure with a Broken-Gap Isotype Heterojunction and a *p–n* Junction in the Substrate

M. Aĭdaraliev, N. V. Zotova, S. A. Karandashev, B. A. Matveev,
M. A. Remennyĭ, N. M. Stus', G. N. Talalakin, and V. V. Shustov
Ioffe Physicotechnical Institute, Russian Academy of Sciences, St. Petersburg, 194021 Russia
e-mail: bmat@iropt3.ioffe.rssi.ru

Received July 8, 2002

Abstract—An electroluminescent structure of the *P*-$Ga_{0.92}In_{0.08}P_{0.05}As_{0.08}Sb_{0.87}$/*p*-InAs/*n*-InAs type containing a broken-gap *P–p* isotype heterojunction and a *p–n* junction in the substrate volume is obtained and is shown to exhibit emission peaks at λ = 1.9 and 3.1 μm at 77 K and 2.1 and 3.6 μm at 300 K. The longwave luminescence band is due to radiative recombination in the *p*-region of the *p–n* junction. The shortwave luminescence band is due to recombination in the *P*-GaInPAsSb wide-bandgap solid solution layer to which nonequilibrium electrons are supplied from the *p–n* junction in the substrate volume. *© 2002 MAIK "Nauka/Interperiodica".*

Introduction. Previously [1], we reported the synthesis of a five-component solid solution of composition $Ga_{0.92}In_{0.08}P_{0.05}As_{0.08}Sb_{0.87}$ which is isoperiodic with InAs and possesses a bandgap width of 695 meV at 77 K and 640 meV at 300 K. It was demonstrated that the InAs/$Ga_{0.92}In_{0.08}P_{0.05}As_{0.08}Sb_{0.87}$ interface represents a broken-gap heterojunction of type II and that the *P*-GaInPAsSb/*p*-InAs isotype junction possesses rectifying properties. The obtained solid solution was implemented in prototypes of a light-emitting diode and a photodiode characterized by the maximum emission intensity and photosensitivity, respectively, in the region of 1.9 μm [1].

Here, we report on the two-wave emission at λ = 2.1 and 3.6 μm observed in a structure comprising a *P*-$Ga_{0.92}In_{0.08}P_{0.05}As_{0.08}Sb_{0.87}$/*p*-InAs broken-gap isotype heterojunction and a *p–n* junction in the substrate volume.

Sample preparation and characterization. The films of a five-component solid solution of composition $Ga_{0.92}In_{0.08}P_{0.05}As_{0.08}Sb_{0.87}$ were grown by liquid-phase epitaxy on *n*-InAs(111) substrates using a method described previously [1]. The total epilayer thickness was 5 μm. The *p–n* junction, obtained by doping the substrate with zinc to a concentration of 5×10^{17} cm^{-3}, was created in the substrate volume at a distance of 2 μm from the GaInPAsSb/InAs interface.

The sample heterostructures were studied by measuring the photo- (PL) and electroluminescence (EL) spectra. The PL spectra were excited by a GaAs laser (LPI-14) and measured at 77 K in the reflection mode on the epilayer side. The EL spectra were measured using 0.5×0.5 mm plates with a point contact made on the epilayer and a continuous electrode layer deposited onto the InAs substrate.

Results and discussion. Figure 1 presents a PL spectrum of the heterostructure measured at 77 K. This spectrum displays (i) a shortwave emission band with a peak at 655 meV and a full width at half-maximum (FWHM) of 45 meV (in agreement with the data reported previously for an analogous epilayer of zinc-doped $Ga_{0.92}In_{0.08}P_{0.05}As_{0.08}Sb_{0.87}$ [1]) and (ii) a longwave band of emission from the substrate with a peak near 380 meV.

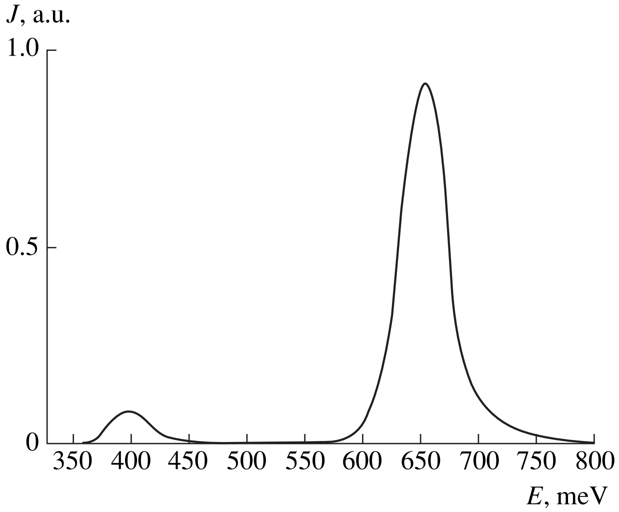

Fig. 1. The typical PL spectrum of a GaInPAsSb/InAs heterostructure measured at 77 K.

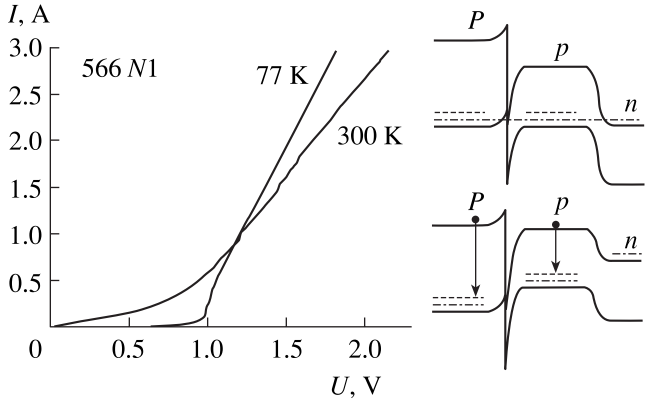

Fig. 2. The direct-bias branches of the current–voltage (*I–U*) characteristics measured at 77 and 300 K and the energy band diagrams of a GaInPAsSb/InAs heterostructure for zero and nonzero direct bias voltage.

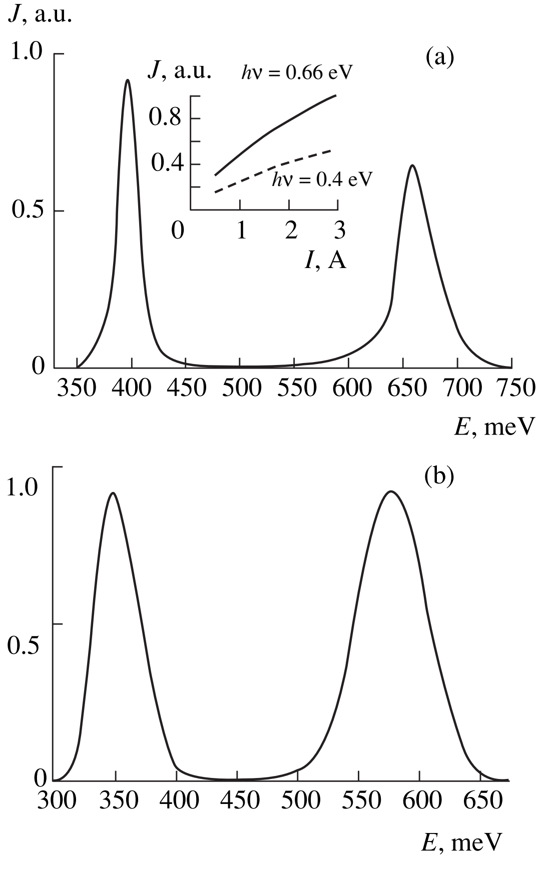

Fig. 3. The EL spectra measured at 77 K (a) and 300 K (b) in a directly biased structure with $I = 3$ A. The inset to Fig. 3a shows the plots of emission intensity versus current passed through the sample structure for both emission bands.

Figure 2 shows the direct branches of the current–voltage (*I–U*) characteristics of the samples and the energy band diagrams of these heterostructures for zero and nonzero direct bias (with positive potential on the wide-bandgap *P*-type layer and negative potential on the substrate). The *I–U* curve exhibits a typical diode character with a cutoff voltage of 0.95 and 0.75 V at 77 and 300 K, respectively. These cutoff voltage values indicate that the applied voltage is sufficient to provide for the complete rectification of bands in the structure: 0.4 V for the *p–n* junction and 0.2 V for the *P–p* isotype junction. The serial resistance of the sample is determined by the bulk of the structure, as confirmed by an increase in this resistance from 0.25 to 0.4 Ω (due to a decrease in the carrier mobility) in response to a temperature increase from 77 to 300 K.

Figure 3 presents the EL spectra measured at 77 K (a) and 300 K (b) with a direct bias. The low-temperature EL spectrum displays two emission bands with peaks at 398 meV (FWHM ≈ 20 meV) and 660 meV (FWHM ≈ 35 meV). Here, the longwave emission band is due to the radiative recombination in the *p*-region of the *p–n* junction. The shortwave luminescence band whose peak position coincides with that of the PL band of the wide-bandgap layer is apparently due to recombination in the bulk of the five-component solid solution layer. The inset to Fig. 3a shows the plots of emission intensity versus current passed through the sample structure for both emission bands. The room-temperature EL spectrum also contains two emission bands with peaks at 350 and 580 meV (Fig. 3b). As the temperature increases from 77 to 300 K, the intensity of both peaks drops by a factor of approximately 50. The temperature coefficient of the emission-band shift amounts to -3×10^{-4} eV/K for both peaks, which corresponds to the temperature coefficient of variation of the bandgap width for InAs. Negatively biased structures (with a positive potential on the substrate) produced no EL signal.

In order to interpret the obtained results, let us consider the energy band diagrams of the heterostructure studied (Fig. 2). The GaInPAsSb/InAs interface represents a single broken-gap isotype *P–p* heterojunction with a band discontinuity on the order of 60 meV [1, 2]. In thermodynamic equilibrium, the heterojunction contains a quantum well for electrons from the substrate side that is related to the electron transition from the valence band of the five-component solid solution to the conduction band of *p*-InAs. For a doping level of 5×10^{17} cm^{-3}, the quantum well width does not exceed 400 Å [3]. In a directly biased heterostructure, the band bending at the heterojunction increases, the depth of the quantum well increases, and the electron density in this well grows. In addition, the valence band top of the five-component solid solution decreases and the conduction band bottom decreases, thus reducing the potential barrier for electrons from the side of the substrate. In the structure studied, the *p–n* junction is situated inside the narrow-bandgap substrate. Evidently, the longwave emission is due to recombination in the *p*-region of the *p–n* junction. The *p*-region thickness does not exceed 2 µm, whereas the diffusion length of electrons reaches 10 µm. Therefore, a certain fraction of nonequilibrium electrons readily reach the *P–p* heterojunction, fill the quantum well, and pass to the solid solution to form a shortwave emission band with a peak at 680 meV.

Thus, we obtained heterostructures of the *P*-$Ga_{0.92}In_{0.08}P_{0.05}As_{0.08}Sb_{0.87}$/*p*-InAs/*n*-InAs type containing a *P–p* broken-gap isotype heterojunction and a *p–n* junction in the substrate volume which exhibit emission at λ = 1.9 and 3.1 μm at 77 K and 2.1 and 3.6 μm at 300 K. Such structures can be used for the creation of two-wavelength light-emitting diodes for gas sensors with working and reference channels.

REFERENCES

1. M. Aĭdaraliev, N. V. Zotova, S. A. Karandashev, *et al.*, Fiz. Tekh. Poluprovodn. (St. Petersburg) **36**, 1010 (2002) [Semiconductors **36**, 944 (2002)].
2. M. P. Mikhaĭlova, G. G. Zegrya, K. D. Moiseev, *et al.*, Fiz. Tekh. Poluprovodn. (St. Petersburg) **29**, 687 (1995) [Semiconductors **29**, 357 (1995)].
3. T. I. Voronina, T. S. Lagunova, M. P. Mikhaĭlova, *et al.*, Fiz. Tekh. Poluprovodn. (St. Petersburg) **32**, 215 (1998) [Semiconductors **32**, 195 (1998)].

Translated by P. Pozdeev

Technical Physics Letters, Vol. 28, No. 12, 2002, pp. 1004–1006. Translated from Pis'ma v Zhurnal Tekhnicheskoĭ Fiziki, Vol. 28, No. 23, 2002, pp. 63–69.
Original Russian Text Copyright © 2002 by Kalanov, Khaidarov, Paizullakhanov.

Temperature Dependence of the Elastic and Inelastic Moduli of $YBa_2Cu_3O_{7-\delta}$ Ceramics

M. U. Kalanov, T. Kh. Khaidarov, and M. S. Paizullakhanov
Institute of Nuclear Physics, Academy of Sciences of the Republic of Uzbekistan, Tashkent, Uzbekistan

Received July 15, 2002

Abstract—Elastic and inelastic moduli of the superconducting yttrium–barium oxide ceramics $YBa_2Cu_3O_{7-\delta}$ (YBCO) were studied using the ultrasonic resonance technique. In the range from room temperature up to the temperature of the ortho–tetra phase transition, the elastic and inelastic moduli of YBCO samples exhibit a number of anomalies. It is shown that these features are related to the behavior of active oxygen in the ceramics, the phase inhomogeneity of the material, and the phase transitions. *© 2002 MAIK “Nauka/Interperiodica”.*

As is known, the measurement of internal friction is among the most structure-sensitive methods used for studying the mechanical properties of materials [1]. For this reason, this method can be applied to the investigation of phase states, phase transitions, and the related mechanical properties of superconducting yttrium–barium oxide ceramics in the high-temperature range. Investigations in the temperature range from 0 to 800°C revealed maxima of internal friction in $YBa_2Cu_3O_{7-\delta}$ (YBCO) at about 100, 250, and 600°C [2]. The peak at 250°C was attributed to the absorption of atmospheric oxygen by the samples, the anomaly at 600°C was assigned to a phase transition, and the nature of the peak at 100°C (the intensity of which depends on the sample heating rate) still remains unclear. Varyukhin *et al.* [3, 4] studied YBCO ceramics in the same temperature range using a combination of methods including the internal friction, DTA, and X-ray diffraction techniques. The peaks of internal friction were observed at about 70, 250, 380, 430, and 680°C and were related to an anomalous behavior of the shear modulus (except for the low-temperature peak at 70°C).

Lemanov *et al.* [5] studied the effect of temperature on the attenuation of ultrasound in YBCO in the megahertz frequency range ($6.2 \leq x \leq 6.8$) and observed a peak of absorption at a certain temperature (in the region of 120–180°C) depending on the signal frequency. The frequency dependence of this absorption peak was indicative of a relaxation character of this feature. However, the appearance of this peak was attributed to the properties of structural defects in the samples because a significant contribution to the absorption at high frequencies is due to the mechanism of ultrasound scattering on structural inhomogeneities [6]. At the same time, Tallon *et al.* [7] reported on the absence of anomalies in the mechanical properties of YBCO ceramics (internal friction, elastic modulus, shear modulus) in the temperature range below the ortho–tetra phase transition. Thus, the existence of anomalies in the internal friction and elastic and shear moduli in the region of the ortho–tetra phase transition can be considered to be reliably established; moreover, there is common agreement as to the mechanism of these anomalies [2–5, 7]. At the same time, the physical nature of anomalies in the mechanical properties of YBCO observed in the low-temperature region is still far from being clear.

In order to fill this gap, we also studied the behavior of the internal friction (Q^{-1}) and the Young modulus (E) of YBCO in the temperature interval from 300 to 1000 K using the ultrasonic resonance technique based on measurement of the bending oscillations of a disk-shaped sample with a thickness of t = 2.78 mm and a diameter of d = 14.02 mm. The measurements were performed in the frequency range from 20 to 40 kHz using an experimental setup described in detail in [1]. The values of the internal friction and elastic modulus were determined using a method also described in [1], based on experimentally measured fundamental frequencies of disk samples. The calculation was performed using the formulas $Q^{-1} = 2[\Delta f_1(n, p)]/f_1(n, p)$ and $E = \rho\{[f_i(n, p)d]/K_i(n, p)\}^2$, where $f_i(n, p)$ is the fundamental frequency of a sample corresponding to the ith oscillation mode, n is the number of nodal rings in the oscillation shape, p is the number of nodal diameters, and $K_i(n, p)$ is the dimensionless frequency parameter dependent on the thickness (t), diameter (d), density (ρ), and the Poisson ratio (ν) of the sample. The oxygen index of the YBCO samples studied was 6.80–6.89 (δ = 0.20–0.11), as determined from the X-ray diffraction measurements performed on a DRON-UM1 diffractometer using Cu$K\alpha$ radiation ($\lambda_{\mathrm{Cu}K\alpha}$ = 1.542 Å). The superconducting transition temperature was T_c = 87–89 K with a transition width of about 1.5 K; the density of samples was about ~4.9 g/cm^3. The samples were heated and cooled at a rate of 0.3–2 K/min. The error of determination of the internal friction (Q^{-1}) was about 6%.

Curves illustrating the temperature-induced variation of the Young modulus (E) and the internal friction (Q^{-1}), measured at a frequency of 39 kHz using a single heating–cooling cycle in the range of temperatures from 300 to 950 K, are presented in the figure. The temperature dependence of the internal friction measured in the heating mode reveals clear maxima at 343, 413, 523, 663, 723, and 833 K. In the cooling mode, the high-temperature peaks are well reproduced, while the low-temperature ones (523 K and below) are not observed. Moreover, the low-temperature peaks of internal friction are not reproduced during the second cycle (either in the heating or in the cooling regime).

The temperature dependence of the Young modulus also has a rather complicated character. In the sample heating mode, the E value sharply drops as the temperature is increased to 390 K, then exhibits a small plateau, and continues to decrease until reaching a minimum at 473 K. In the temperature interval from 473 to 723 K, the modulus exhibits a sharp (more than sevenfold) increase with a small feature ("shelf") at 553 K. Above 723 K, the increase changes to a decrease and the E value exhibits a second minimum at 833 K, after which the growth with temperature is restored. In the cooling mode, no new features are observed in the high-temperature region, while the behavior in the low-temperature region changes dramatically and the room-temperature modulus amounts to only 6– 7% of the initial value. A similar temperature variation of the Q^{-1} and E values was observed when the measurements were performed at a frequency of 26 kHz. An increase in the amount of lattice oxygen in the YBCO ceramics led to a small high-temperature shift of the Q^{-1} and E maxima situated above 500 K.

A comparison of these results to the structural data for the same samples studied at various temperatures shows that the anomalies in the internal friction and the Young modulus take place at temperatures approximately corresponding to the various phase states of YBCO ceramics. Therefore, we may suggest that anomalies in the mechanical properties of the samples observed in the temperature interval studied are determined by the corresponding structural changes accompanying heating and cooling of the samples. For example, the maximum in $Q^{-1}(T)$ and the corresponding minimum in $E(T)$ and $T = 833$ K reflect the well-known phase transition from the orthorhombic to tetragonal phase: in a narrow temperature interval, the Q^{-1} value grows, to peak at 833 K; the background level under the peak also increases severalfold as compared to the average level observed at low temperatures. The positions of the peaks are virtually independent of the frequency. Analogous effects in the region of the phase transitions have been reported by other researchers [2–5, 7].

The peaks of internal friction observed in the regions of 663 and 723 K frequently appear as doublets and strongly depend on the concentration of lattice oxygen in the ceramics [2, 4, 9]. The latter circumstance allows us to suggest that these peaks are due to diffusion processes involving the incorporation of oxygen atoms into the lattice of ceramics or their escape from this lattice. The dependence of the peak height on the oxygen content also confirms this hypothesis. Indeed, the heights of the aforementioned Q^{-1} peaks in the sample with a lower oxygen content increase in the course of each subsequent measurement. This implies that the sample absorbs oxygen from the environment, which accounts for the growth in the peak height. The increase in the oxygen content was also confirmed by the results obtained from a structural analysis: after two heating–cooling cycles, the content of oxygen in the lattice increased from 6.80 to 6.83. In the samples with smaller (but still nonzero) δ values, the peak heights are virtually not subject to change, which implies that the oxygen sorption and desorption processes are in dynamic equilibrium. The anomalous behavior of oxygen, as manifested by the temperature dependences of Q^{-1} and E, is characteristic of many perovskite-like materials [8], in particular, of the YBCO ceramics [9].

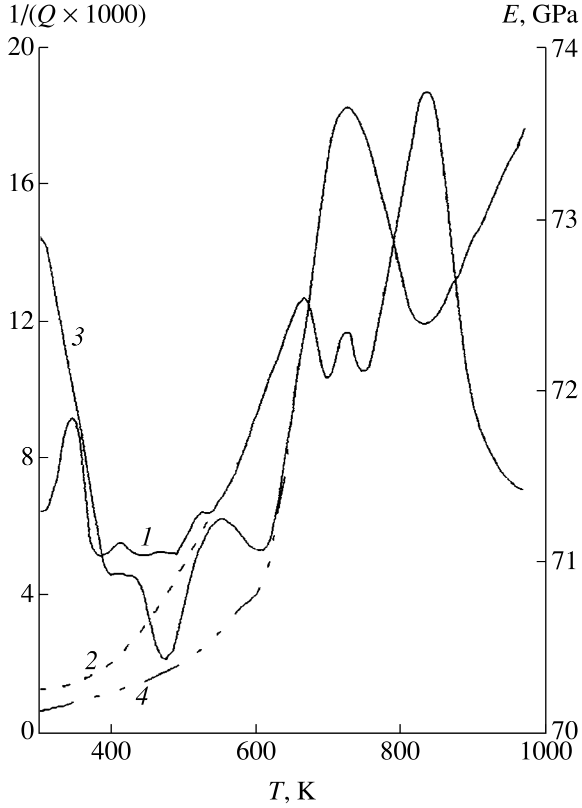

Temperature variation of (*1*, *2*) the internal friction Q^{-1} and (*3*, *4*) the Young modulus E of the YBCO ceramics measured in the course of (*1*, *3*) heating and (*2*, *4*) cooling of the sample in a single thermal cycle between 300 and 950 K.

Being related to the sorption and desorption of oxygen, the diffusion processes taking place in the region of 663 and 723 K render the YBCO ceramics inhomogeneous with respect to the phase state: various orthorhombic phases differing only slightly in the oxygen index δ may coexist in the ceramics at these temperatures. These phases may account for the complicated shape of the internal friction profile. Incorporation of an additional amount of oxygen into the lattice increases the chemical binding of structural elements of the ceramics. This leads to a significant increase in the Young modulus in the temperatures interval from 663 to 723 K. A large width of the $E(T)$ peak at $T = 723$ K is also indicative of the phase inhomogeneity of the YBCO ceramics studied. It should be noted that the interval of temperatures between 663 and 723 K is usually employed by technologists for saturating superconducting YBCO ceramics with oxygen when $7 - \delta < 7$.

The peak of internal friction at 343 K was observed in all the studied samples. Therefore, this peak is not influenced by the content of lattice oxygen in the ceramics. However, the dependence of the peak height on the sample heating rate suggests that this feature is related to the behavior of active oxygen in the near-surface and/or intergranular layers of the ceramics [10]. Since the saturation with active oxygen leads to deformation of these layers, the peak of internal friction observed at 343 can be considered to be of deformation nature [11].

As is known, the deformation of a material can be relieved by annealing. Previously [10], we demonstrated that active oxygen can be easily removed from intergranular layers of ceramics by heating the samples to 500 K. Therefore, the removal of active oxygen relieves deformation of the aforementioned layers, after which the related internal friction peak must vanish; this is actually observed in experiment. Apparently, almost all active oxygen can desorb from the intergranular layers of a slowly (0.3 K/min) heated ceramic, which results in a relief in deformation and leads to vanishing of the internal friction peaks. In the case of a relatively rapid (2 K/min) heating, the oxygen is only partly desorbed, the deformation is incompletely relieved, and the internal friction peak is retained. The loss of any amount of active oxygen from the aforementioned layers leads to weakening of the chemical bonds between granules. This leads to a sharp drop in the Young modulus within the temperature interval from room temperature to ~500 K during the first heating. The absence of the Q^{-1} peak at 343 K in the second heating, as well as the anomalies in the low-temperature behavior of E, are also explained by the oxygen being desorbed from the intergranular layers of ceramics during the preceding heating. Indeed, the Q^{-1} peak height and the anomalies of E can be restored by keeping the samples under normal conditions ($T = 300$ K; $RH = 50\%$) for 7–8 days after heating.

Thus, the elastic and inelastic moduli of YBCO samples exhibit a number of anomalies in the range from room temperature to the temperature of the ortho–tetra phase transition. These anomalies are related to the behavior of active oxygen in the ceramics, the phase inhomogeneity of the material, and the phase transitions.

REFERENCES

1. V. M. Baranov, *Ultrasonic Measurements in Atomic Engineering* (Atomizdat, Moscow, 1973).
2. V. M. Arzhavitin, V. I. Golovin, G. F. Tikhinskiĭ, *et al.*, Sverkhprovodimost: Fiz., Khim., Tekh. **2** (10), 153 (1989).
3. V. N. Varyukhin, Yu. M. Ivanchenko, A. V. Reznikov, and S. B. Strongin, Ukr. Fiz. Zh. **34** (5), 713 (1989).
4. V. G. Bar'yakhtar, V. N. Varyukhin, and A. B. Nazarenko, Sverkhprovodimost: Fiz., Khim., Tekh. **3** (6), 1145 (1990).
5. V. V. Lemanov, A. B. Sherman, G. O. Andrianov, and I. Érgashev, Fiz. Tverd. Tela (Leningrad) **32** (7), 2161 (1990) [Sov. Phys. Solid State **32**, 1258 (1990)].
6. Yu. A. Burenkov, V. I. Ivanov, A. B. Lebedov, *et al.*, Fiz. Tverd. Tela (Leningrad) **30** (10), 3188 (1988) [Sov. Phys. Solid State **30**, 1837 (1988)].
7. J. L. Tallon, A. H. Schuitema, and N. E. Tapp, Appl. Phys. Lett. **52** (6), 507 (1988).
8. P. S. Galasso, *Structure, Properties, and Preparation of Perovskite-Type Compounds* (Pergamon, New York, 1969).
9. Naiping Zhu, Z. Phys. B **70** (4), 409 (1988).
10. M. U. Kalanov, M. S. Paĭzullakhanov, V. M. Rustamova, *et al.*, Pis'ma Zh. Tekh. Fiz. **23** (1), 13 (1997) [Tech. Phys. Lett. **23**, 13 (1997)].
11. A. S. Nowick and B. S. Berry, *Anelastic Relaxation in Crystalline Solids* (Academic, New York, 1972; Atomizdat, Moscow, 1975).

Translated by P. Pozdeev

Technical Physics Letters, Vol. 28, No. 12, 2002, pp. 1007–1010. Translated from Pis'ma v Zhurnal Tekhnicheskoĭ Fiziki, Vol. 28, No. 23, 2002, pp. 70–77.
Original Russian Text Copyright © 2002 by Kogut.

Effect of the Ellipticity of a Dielectric Resonator on the Induced Whispering Gallery Modes

A. E. Kogut

Usikov Institute of Radiophysics and Electronics, National Academy of Sciences of Ukraine,
Kharkov, Ukraine

e-mail: maksim@ire.kharkov.ua; koguts@ic.kharkov.ua

Received July 25, 2002

Abstract—The influence of ellipticity of a dielectric resonator on the whispering gallery (WG) oscillation modes induced by a lumped radiation source was studied. Dependence of the spectral characteristics of resonators and the spatial distributions of oscillation fields on the WG mode propagation direction is experimentally determined. © *2002 MAIK "Nauka/Interperiodica".*

Spherical and hemispherical dielectric resonators featuring whispering gallery (WG) oscillation modes possess unique properties in the millimetric wave range, the most important property high intrinsic Q values [1]. This makes such resonators advantageous for the development of highly stable oscillators and power summators operating in the millimetric wave range [2]. High electrodynamic characteristics of the spherical dielectric resonators featuring WG modes are determined by the absence of sharp interfaces and by narrow regions of localization of the oscillation fields at the resonator surface [3].

The central symmetry of a dielectric resonator is violated by its ellipticity, which can lead to a number of interesting effects involving a change in the spectral characteristics and in the spatial distribution of the induced oscillation fields [4]. From the standpoint of geometric optics, variation of the minor and major axes of the ellipsoid may result in the appearance of a preferred direction of the radiation beam propagation in the resonator and in the formation of surface regions closed to the oscillation fields [5].

Investigation of the self-oscillations of ellipsoids of revolution can provide a basis for studying the characteristics of induced oscillations of the WG-mode type in dielectric resonators with ellipticity. A convenient object for this type of investigation is a dielectric ellipsoid possessing insignificant differences in the lengths of geometric axes as compared to the oscillation wavelength. By moving the radiation source along one of the curvilinear coordinates, one can change the direction of wave propagation in a resonator with a small curvature gradient and follow the dynamics of variation of the spectral and energy characteristics of the induced oscillations. In this way, it is possible to pass from the spectrum of a resonator with electrodynamic properties close to those of a dielectric sphere to the spectrum of oscillations characteristic of an ellipsoidal resonator and perform a comparative analysis of their properties. The curvature gradient means the difference in the surface curvature of the ellipsoid in various regions. Evidently, the aim of such an analysis can be reached provided that the angle of deviation of the waves propagating along the ellipsoidal dielectric resonator surface are sufficiently small.

Figure 1 shows a schematic diagram of the object used in the experiments. A dielectric elongated biaxial ellipsoid (*1*) and a radiation source (*2*) were mounted in a special holder (not depicted in Fig. 1). The ellipsoid (made of Teflon) has the minor semiaxes $|OA| = |OB| = 19$ mm and the major semiaxis $|OC| = 20$ mm. The radiation source was the open end of a metallic waveguide with a rectangular (7.2 × 3.4 mm) cross section. The problem of matching the metallic waveguide to the environment (including the dielectric resonator) was solved by filling the waveguide with a dielectric material (Teflon). The open waveguide end was spaced at 1–1.5 mm from the resonator surface. The resonator holder was made of a material (porous foamed plastic) with a permittivity close to that of vacuum.

The experiments were performed in the 27–36 GHz frequency interval. The resonance frequencies were determined with the aid of a panoramic standing wave ratio (SWR) meter. The SWR data were used to adjust the level of coupling between the primary radiation source and the induced oscillation fields in the resonator studied and to determine the resonance response amplitudes. The oscillation modes were identified and the mode field distributions on the ellipsoid surface were determined using the probe technique [6]. The spectra of induced oscillations were measured in the course of variation of the azimuthal coordinate φ_i of the radiation source in the resonator cross-sectional plane

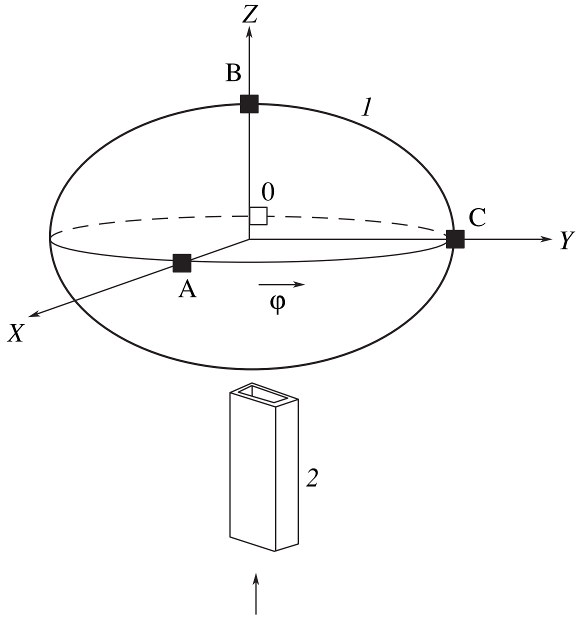

Fig. 1. Schematic diagram of the experimental system (see text for explanations).

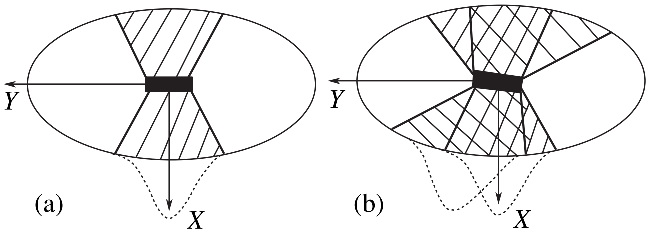

Fig. 2. Schematic diagrams showing the regions of localization of the WG mode fields on the surface of an ellipsoidal dielectric resonator.

XOY determined by the intersection of the minor and major axes (Fig. 1). The radiation source position is characterized by the coordinate φ_i counted from the plane formed by the intersection of the minor semiaxes (this plane coincides with the waveguide *E*-plane).

For an arbitrary coordinate φ_i of the radiation source, the spectrum of induced oscillations of the WG-mode type in the dielectric resonator studied simultaneously contains $\mathrm{TM}_{nml}(E_r \neq 0)$ and $\mathrm{TE}_{nml}(E_r = 0)$ modes. Here, E_r is the radial component of the electric field strength and (n, m, l) are the indices showing the number of field variations in the polar (θ), azimuthal (φ), and radial (r) coordinates, respectively. The efficiency of excitation of the oscillation modes with TE polarization is small as compared to that for the TM modes; for this reason, the former modes were not considered in this study. The resonance TM oscillation response exhibits an almost periodic variation on the frequency scale, with the distance between the neighboring resonances being close to 1.4 GHz.

For $\varphi_i = 0$, the fields of TM oscillations on the resonator surface are localized in the regions having the shape of nonuniform belts (cross-hatched area in Fig. 2a). The arrangement of the radiation source relative to the ellipsoid axes is indicated in Fig. 2 by a black rectangle. The field belts exhibit narrowing in the regions of the source and its image. Between these, the belt expands, to reach a maximum width of 31 mm at a resonance frequency of $f = 33.864$ GHz. The minimum belt width is close to the length of the wide waveguide wall (7.2 mm). The minor axes of the ellipsoid lie in the central cross section of the oscillation field belt. The oscillation field intensity maximum for a mode with a single variation of the field in the transverse cross section occurs at the center of the belt width. In the experiment, this point is detected from the maximum change in the resonance amplitude in response to a small absorbing inhomogeneity being introduced into the oscillation field. The oscillation field intensity distribution is qualitatively depicted by the dashed profile in Fig. 2a. Note that, for the given dimensions of the system, no higher azimuthal modes with $m > 1$ are excited in the dielectric resonator studied.

Even an insignificant change in the source coordinate φ_i relative to zero leads to a decrease in the resonance response frequency, and the oscillation field belt exhibits deformation. The resonance response increases in width, representing a set of smaller resonances. The results of identification of the corresponding oscillations showed that they correspond to a single mode with the same indices n, m, l and differ only in frequency. These oscillations represent waves propagating along the dielectric resonator surface by various trajectories differing in shape and length.

The simultaneous appearance of a series of curvilinear dielectric waveguide channels was confirmed by the results of investigation of the spatial distribution of oscillation fields at the ellipsoid surface (Fig. 2b). Each of these oscillations corresponds to a nonuniform field belt. These belts exhibit common regions of narrowing (in the vicinity of the source and its image) and are spatially separated at the periphery of the expanded part. Accordingly, the maxima of the field intensities are displaced relative to each other. In the region of maximum expansion of the field belt, the oscillation fields partly overlap and the entire combination represents a field spot having the shape of a nonuniform belt with pronounced narrowings and intermediate expansion. The dimensions of the total belt of these oscillation fields depend on the number of partial oscillations and are determined by the coordinate φ_i of the radiation source.

Figure 3 illustrates the dependence of the relative resonance response amplitude A/A_m (normalized to maximum) on the φ_i value. From this profile, it is possible to judge the number of oscillations corresponding to the same mode that are simultaneously excited in the dielectric resonator studied and the relative efficiency of excitation of these oscillations. As can be seen, the maximum number of resonance oscillations ($N = 7$) is observed in the interval of φ_i from 30° to 70° ($f \approx$ 33,86 GHz). As the φ_i value increases further to 90°, the number of excited oscillations decreases to reach $N = 3$ in the limiting case of $\varphi_i = 90°$.

The resonance response of oscillations induced upon increasing the coordinate φ_i of the radiation source coordinate in the entire interval from 0° to 90° occupies the low-frequency region of the spectral curve corresponding to their common mode, since the component waves propagate in the resonator along the trajectories possessing long lengths. The efficiency of the excitation of such oscillations decreases with increasing φ_i. It can be suggested that a lower efficiency of excitation is determined by higher radiation energy losses related to the curvature gradient on the dielectric resonator surface. It should be noted that each oscillation corresponds to a point of maximum excitation efficiency on the $A/A_m(\varphi_i)$ profile. For various oscillations, corresponding to the same mode and differing only in the frequency, the maximum efficiencies of excitation are observed at different coordinates φ_i.

More complete information about the energy losses of oscillations in a given dielectric resonator is provided by the intrinsic Q value. However, under the experimental conditions studied, determination of this characteristic was hindered by the smeared character of the resonance curve, which was related to the simultaneous excitation of several oscillations with close frequencies.

The results of determination of the field belt widths for oscillations of the WG-mode type on the surface of the dielectric resonator studied showed that this width can vary from one to a few wavelengths. In accordance with this, we may conclude that the size of the WG-mode beam propagating along the resonator surface changes as well. Previously, analogous regularities in the distribution of oscillation fields formed by a WG-mode beam were observed in quasioptical hemispherical dielectric resonators and interpreted in terms of geometric optics [3]. In connection with this, the results of the electrodynamic investigations conducted in this work can also be explained within the framework of geometric optics (ray approximation). When the waveguide H-plane is perpendicular to the plane determined by the intersection of the minor axes in the biaxial ellipsoid, the extreme rays originate from the source at equal angles and are incident onto the resonator surface also at equal angles because the surface curvature at the incidence points is the same. Propagating along the surface along nearly conical trajectories, the extreme rays travel the same distances and arrive at the source image. This corresponds to focusing of the WG-mode waves, which was previously observed for a dielectric hemisphere situated on a flat metal mirror [3]. Otherwise, a difference in the curvature of the resonator surface at the points of incidence of the extreme ray leads to dissimilar ray trajectories in the ellipsoid; they differ in shape, pathlength, and configuration with respect to the geometric axes of the resonator. The shapes on the oscillation field belts are determined by the direction of ray propagation along the resonator surface with a curvature gradient.

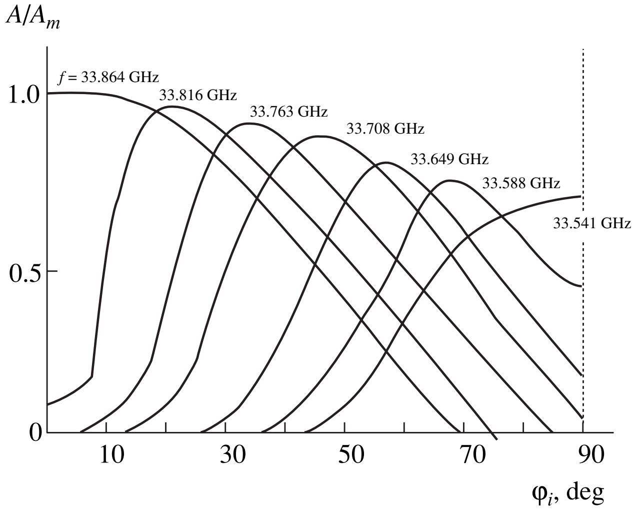

Fig. 3. Plots of the resonance oscillation response amplitude A (normalized to the maximum value A_m) versus the radiation source coordinate φ_i.

The efficiency of excitation of various oscillations is determined by the positions of the component field intensity maximum relative to the trajectory of the central ray originating from the radiation source. Obviously, a maximum excitation efficiency corresponds to the case when the central ray passes through the point of maximum field intensity. This circumstance accounts for the dynamics of variation of the excitation efficiency depending on the coordinate φ_i observed for oscillations corresponding to the same mode of the resonator studied.

Thus, it was demonstrated that the spectral characteristics of an ellipsoidal dielectric resonator with respect to induced oscillations of the WG-mode type and the corresponding spatial distributions of the oscillation fields depend on the position of the wave source relative to the geometric axes of the resonator and are determined by the resonator parameters and the radiation source characteristics. The oscillation excitation efficiency in such a resonator depends on the propagation direction of the corresponding WG-mode waves and is determined by the curvature gradient of the ellipsoidal resonator surface.

REFERENCES

1. M. Gastine, L. Courtois, and I. L. Dormann, IEEE Trans. Microwave Theory Tech. **MTT-15** (12), 694 (1967).
2. S. N. Khar'kovskiĭ and A. E. Kogut, in *Proceedings of the 7th Crimean Conference "Microwave Engineering and Telecommunicational Technology," Sevastopol', 1997*, Vol. 2, p. 361.
3. A. E. Kogut, V. V. Kutuzov, Yu. F. Filippov, and S. N. Khar'kovskiĭ, Izv. Vyssh. Uchebn. Zaved., Radioélektron. **40** (2), 19 (1997).
4. M. E. Il'chenko, V. F. Vzyatyshev, L. G. Gassanov, *et al.*, *Dielectric Resonators*, Ed. by M. E. Il'chenko (Radio i Svyaz', Moscow, 1989).
5. L. A. Vainshtein, *Open Resonators and Open Waveguides* (Sov. Radio, Moscow, 1966; Golem Press, Boulder, 1969).
6. R. A. Valitov, S. F. Dyubko, B. I. Makarenko, *et al.*, *Measuring on Millimetric and Submillimetric Waves: Methods and Technique,* Ed. by R. A. Valitov and B. I. Makarenko (Radio i Svyaz', Moscow, 1984).

Translated by P. Pozdeev

Technical Physics Letters, Vol. 28, No. 12, 2002, pp. 1011–1014. Translated from Pis'ma v Zhurnal Tekhnicheskoĭ Fiziki, Vol. 28, No. 23, 2002, pp. 78–86.
Original Russian Text Copyright © 2002 by Lebedev, Strel'chuk, Savkina, Bogdanova, Tregubova, Kuznetsov, Sorokin.

Investigation of the p^--3C-SiC/n^+-6H-SiC Heterostructures with Modulated Doping

A. A. Lebedev, A. M. Strel'chuk, N. S. Savkina, E. V. Bogdanova, A. S. Tregubova, A. N. Kuznetsov, and L. M. Sorokin
Ioffe Physicotechnical Institute, Russian Academy of Sciences, St. Petersburg, 194021 Russia

Received July 17, 2002

Abstract—A heterostructure of the p^--3C-SiC/n^+-6H-SiC type with modulated doping was synthesized by sublimation epitaxy in vacuum. Features of the current–voltage characteristics and the electroluminescence spectra show evidence of quantum confinement effects in a triangular quantum well at the heterojunction. The results indicate that the proposed technology employing sublimation epitaxy in vacuum can be used to obtain quantum-confined structures based on silicon carbide. *© 2002 MAIK “Nauka/Interperiodica”.*

Introduction. Silicon carbide (SiC), a compound that possesses a large variety of polytypes, is a highly promising material for creating various heterostructures. In recent years, a number of investigations have been reported on the synthesis of epitaxial heterostructures of the 6H-SiC–3C-SiC and 4H-SiC–3C-SiC types using various techniques [1–4]. Recently [1], we studied, for the first time, the electrical characteristics of *p–n* junctions of the *p*-3C-SiC/*n*-6H-SiC type and constructed an energy band diagram that has proved to be close to the theoretically predicted one [5]. The obtained diagram confirmed, in particular, the principal possibility of obtaining a structure featuring a two-dimensional electron gas (2DEG) at the boundary between the two component semiconductor layers.

However, realization of the system with 2DEG requires the use of heterostructures with a modulated doping profile [6], since the system must comprise a wide-bandgap *n*-type semiconductor doped to a high level and a narrow-bandgap semiconductor with an almost intrinsic conductivity. Then, the quantum well bottom in this system is situated below the Fermi level, which makes electron transitions from the wide-bandgap semiconductor to the quantum well with the formation of 2DEG possible.

This study aimed to synthesize such p^--3C-SiC/n^+-6H-SiC heterostructures and characterize their electrical properties.

Sample preparation. The heteropolytype *p–n* structures were grown by sublimation epitaxy in vacuum (SEV) [7] on the (0001)Si face of 6H-SiC substrates (Fig. 1). The process was conducted under the conditions of excess silicon content in the growth zone, which is known to favor the formation of an epitaxial 3C-SiC layer on the hexagonal substrate [8]. The structural perfection of the epitaxial layers was evaluated from X-ray topographs measured in the X-ray backscattering mode using the CuK_α radiation.

As can be seen from an analysis of the X-ray topographs of these deposits (Fig. 1), the epitaxial layer was composed of several twins, each with a total area above 5 mm^2. In order to reduce the ohmic resistance at the contact to *p*-type regions, a p^+-3C-SiC layer was grown on the *p*-3C-SiC surface. The ohmic contacts on the *n*- and *p*-type layers were prepared through magnetron

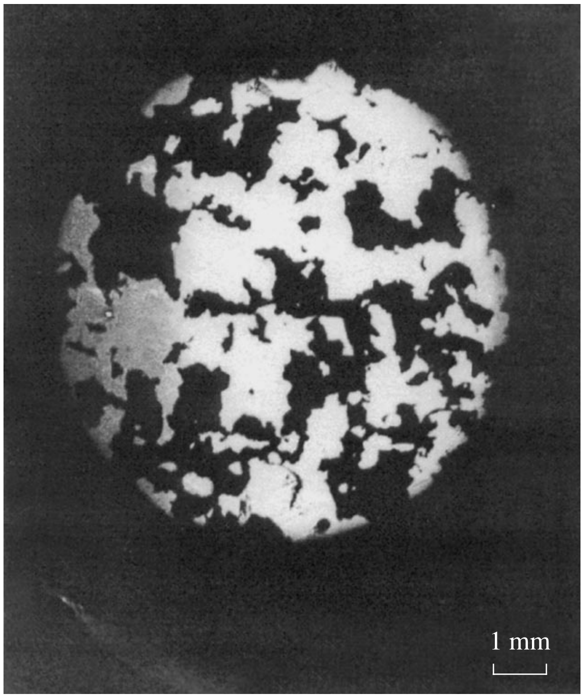

Fig. 1. Typical X-ray topograph of a 3C-SiC–6H-SiC heterostructure (CuK_α radiation; 101.14 reflection).

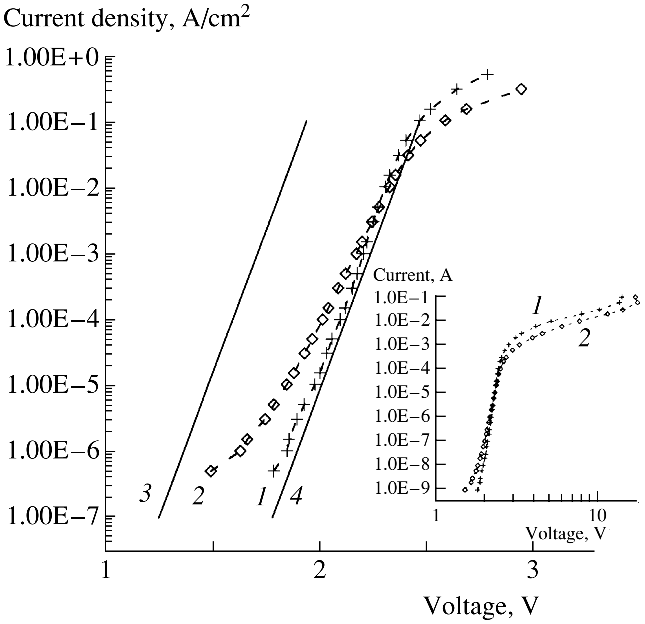

Fig. 2. Experimental current–voltage characteristics of two samples of the p^{-}-3C-SiC/n^{+}-6H-SiC heterojunction, N1 (*1*) and N2 (*2*), and the $J = J_0\exp[qU/(nkT)]$ curves calculated using a model [9] with $n = 2$ for the homopolytype *p–n* structures (*3*) 3C-SiC ($J_0 = 2.3 \times 10^{-18}$ A/cm²) [10] and (*4*) 6H-SiC ($J_0 = 6 \times 10^{-23}$ A/cm²) [11]. The inset shows the *I–U* curves of samples N1 (*1*) and N2 (*2*) measured in the region of high currents.

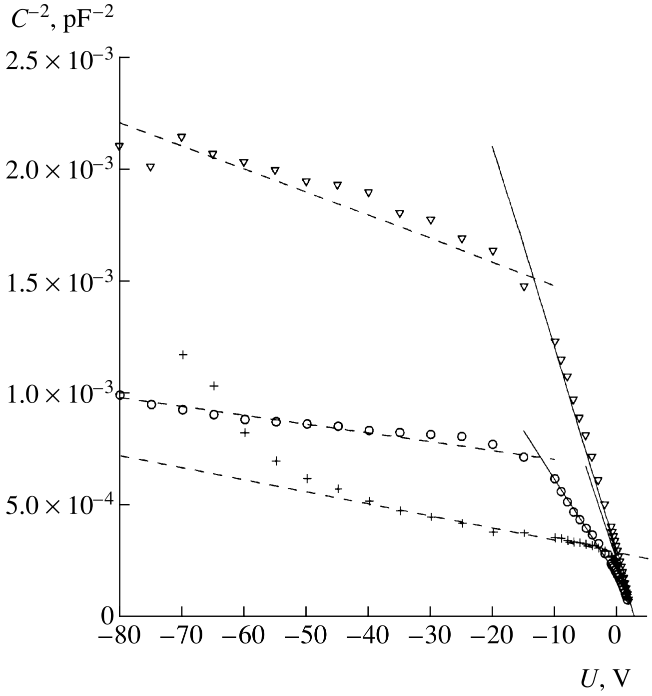

Fig. 3. Capacitance–voltage characteristics of the heterodiodes measured in various regions of a p^{-}-3*C*-SiC/n^{+}-6*H*-SiC structure (circles present the data for sample N2).

sputter deposition of Ni and Al+Ti films, followed by fusion in vacuum at 900 and 1500°C, respectively. Diode structures with a working area diameter of ~500 μm were obtained by ion plasma etching in SF_6.

Results. Figure 2 presents the current–voltage (*J–U*) characteristics of the heterostructures studied. It should be noted that, in the region of small current densities, the dependence is close to the exponential law $J = J_0\exp[qU/(nkT)]$ (Fig. 2) with an ideality factor of $n > 2$. In the best samples (N1), the n value approaches 2 and (as was also reported in [1]) the *J–U* curve is close to that of the 6H-SiC based homopolytype *p–n* structures.

Figure 3 shows typical capacitance–voltage (*C–U*) characteristics measured in various regions of the samples. As can be seen, the plots consist of two parts rectified in the C^{-2} versus U coordinates, which serves as evidence of a sharp *p–n* junction. Is is also seen that the N_a–N_d values exhibit scatter in both parts of the C^{-2} versus U plots for various diodes. The lower part of the *C–U* characteristics corresponds to a slightly doped p^{+}-3C-SiC layer with N_a–N_d ~ 4–5 × 10^{16} cm^{-3}. The N_a–N_d values determined from the slope of the C^{-2} versus U plots were close to those determined using the mercury probe on the initial surface prior to growing the p^{+}-3C-SiC layer. The thickness of the slightly doped layer was about 0.7 μm. The upper part of the *C–U* characteristics corresponds to a strongly doped p^{+}-3C-SiC under contact layer with N_a–N_d ~ (0.4–1) × 10^{18} cm^{-3}. The contact potential difference (*Ud*) determined by extrapolating the C^{-2} versus U plots to zero was ~2.43 V, which is close to the values reported in [1].

When a direct current was passed through the sample structures, the samples exhibited inhomogeneous electroluminescence (EL) at the periphery of the diode mesastructures (light of different colors was emitted from various regions of the diode). An additional contribution was found to proceed from an emission from a region below the contact, which was reflected and scattered from the rear crystal surface. The EL spectra of the diode structures exhibit three emission bands, belonging to the red (1.8–2.1 eV), green (about 2.36 eV), and violet (about 2.9 eV) spectral regions. In addition to these, the spectra of various structures contain one of two peaks (at 2.6 or 2.73 eV) from the blue spectral region. The relative intensities of the EL bands varied from one sample to another.

Figure 4 shows the EL spectrum of a sample structure with a maximum emission (2.357 eV) in the green spectral region. No correlation was observed between the positions of the emission peaks and the direct current density. Also presented in Fig. 4 are the EL spectra of the 3C/3C- and 3C/6H-SiC structures studied previously [1, 12]. The green ($h\nu_{max}$ = 2.296 eV) and violet emission bands were attributed to the annihilation of free excitons in the bulk of 3C-SiC (according to [13], $h\nu_{max}$ = 2.296 eV; note that no correlation between the position of this EL band and the current density was observed in [1, 13]) and in the bulk of 6H-SiC, respectively. The red and both blue EL bands can be due to the radiative recombination of charge carriers in 3C-SiC (red emission) and 6H-SiC (blue emission) [14] with the participation of a level related to the presence of Al in the epilayer. We believe that the violet and green emission bands in the EL spectra of the structures studied (as well as in those reported in [1, 2]) are due to the annihilation of a free exciton in 6H- and 3C-SiC. Note that the green peak (2.357 eV) is shifted approximately by 60 meV toward shorter waves relative to that (2.296 eV) reported in [1] (Fig. 4).

Discussion of results. As is known, quantum confinement leads to the formation of local levels in a quantum well, provided that all the necessary technological conditions are satisfied. The local levels are situated above the conduction band bottom of the narrow-bandgap semiconductor (Fig. 5). As a result, the EL bands of a given material may exhibit a shift toward the shortwave region.

Let us estimate the shift that can be expected for the 3C-SiC–6H- SiC heterojunction studied. According to the well-known formula for the energies of quantum levels in a triangular quantum well [15],

$$\begin{aligned}\varepsilon_N &= (\hbar^2/2m^*)^{1/3}(2/3\pi qE)^{2/3}(N+3/4)\\ &= A_N(E^2/m^*/m_0)^{1/3},\end{aligned}\tag{1}$$

where $N = 0, 1, 2, \ldots$; A_N is a coefficient determined by the constants ($A_0 = 4.56 \times 10^{-7}$, $A_1 = 8.01 \times 10^{-7}$, $A_3 = 1.09 \times 10^{-6}$), E [V/m] is the electric field strength in the quantum well, Q is the electron charge, and $m^*/m_0 = 0.3$ [2] is the ratio of the effective electron mass in 3C-SiC to the free electron mass. The E value can be estimated as the maximum field strength in the p–n junction:

$$E = Ud/W_0 \sim 2 \times 10^7 \text{ V/m},$$

where Ud is the contact potential difference in the p–n structure and W_0 is the thickness of the space charge region at a zero external voltage. Substituting the A, E, and m^*/m_0 values into formula (1), we obtain an estimate for the energy position of the ground state in the quantum well: $\varepsilon_0 = 0.050$ eV. The experimentally determined shift of the peak due to the exciton EL somewhat exceeds the theoretical estimate:

$$\Delta h\nu = \varepsilon_0 + \delta,$$

where $\delta \sim 0.01$ eV. It is possible that a nonzero δ can be related to a decrease in the energy of exciton binding in the Coulomb field of the quantum well.

In the structures studied, it is unlikely that the holes can be injected from p^--3C-SiC to n^+-6H-SiC. Therefore, the EL bands characteristic of 6H-SiC are most probably related to the formation of p-6H-SiC inclusions in the early stages of epitaxial growth of the p-3C-SiC layer [16].

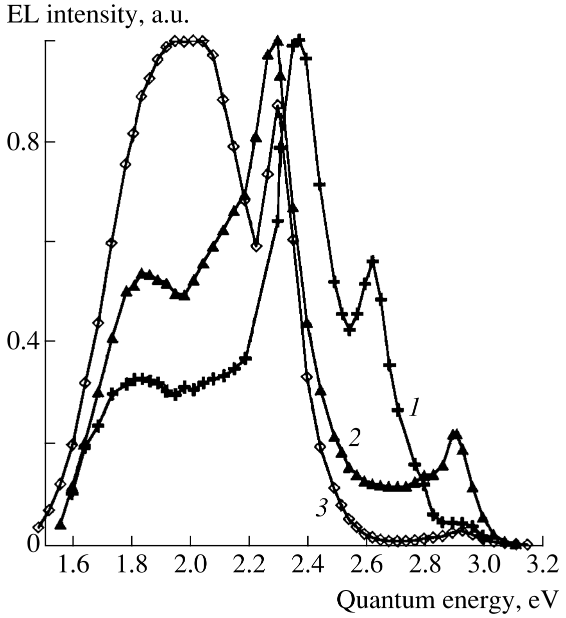

Fig. 4. Room-temperature electroluminescence spectra of heterostructures of (*1*) the p^--3C-SiC/n^+-6H-SiC sample N2 studied in this work (J = 23 A/cm^2) and the samples of (*2*) the p^+-3C-SiC/n^+-3C-SiC (J = 50 A/cm^2) and (*3*) p^+-3C-SiC/n^+-6H-SiC (J = 3000 A/cm^2) structures (data from [1]).

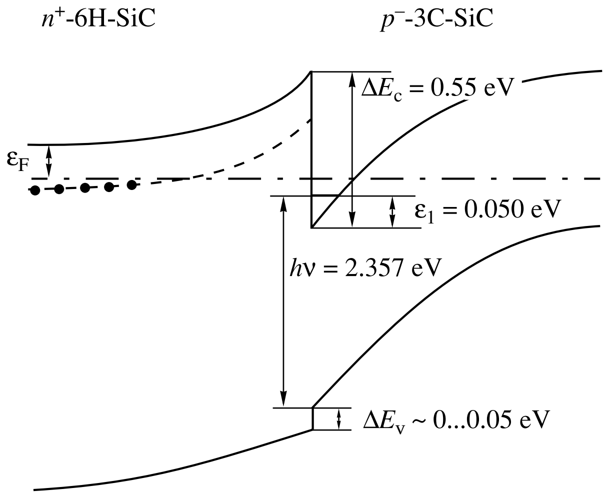

Fig. 5. Energy band diagram of the p^--3C-SiC/n^+-6H-SiC structure studied.

Conclusion. The quantum confinement effect in a triangular quantum well at the p^--3C-SiC/n^+-6H-SiC heterojunction was observed for the first time. Such a structure can serve as a basis for an SiC-based high electron mobility transistor (HEMT). Although a high-quality heterojunction was obtained only on a part of the epitaxial layer, the results show that the SEV technology can be used for quantum-confined structures based on silicon carbide.

Acknowledgments. The authors are grateful to N.S. Averkiev and V.P. Kochereshko for fruitful discussions.

This study was supported by the Russian Foundation for Basic Research (projects nos. 00-02-16688 and 01-02-17657).

REFERENCES

1. A. A. Lebedev, A. M. Strelchuk, D. V. Davydov, *et al.*, Appl. Surf. Sci. **184**, 419 (2001).
2. A. Fissel, U. Kaiser, B. Schroter, *et al.*, Appl. Surf. Sci. **184**, 37 (2001).
3. R. S. Okojie, M. Xhang, P. Pirouz, *et al.*, Appl. Phys. Lett. **79**, 3056 (2001).
4. A. A. Lebedev, G. N. Mosina, I. P. Nikitina, *et al.*, Pis'ma Zh. Tekh. Fiz. **27** (24), 57 (2001) [Tech. Phys. Lett. **27**, 1052 (2001)].
5. F. Bechstedt, P. Kackell, B. Adolph, and J. Furthmuller, Phys. Status Solidi B **202**, 35 (1997).
6. *Molecular Beam Epitaxy and Heterostructures*, Ed. by L. L. Chang and K. Ploog (Martinus Nijhoff Publ., Dordrecht, 1985).
7. N. S. Savkina, A. A. Lebedev, D. V. Davydov, *et al.*, Mater. Sci. Eng. B **77** (1), 50 (2000).
8. Yu. A. Vodakov, G. A. Lomakina, and E. N. Mokhov, Fiz. Tverd. Tela (Leningrad) **24**, 1377 (1982) [Sov. Phys. Solid State **24**, 780 (1982)].
9. S. T. Sah, R. N. Noyce, and W. Shockley, Proc. IRE **45**, 1228 (1957).
10. A. M. Strel'chuk, V. S. Kiselev, and S. F. Avramenko, Mater. Sci. Eng. B **61–62**, 437 (1999).
11. A. M. Strel'chuk, Fiz. Tekh. Poluprovodn. (St. Petersburg) **29**, 1190 (1995) [Semiconductors **29**, 614 (1995)].
12. A. M. Strel'chuk, N. S. Savkina, A. N. Kuznetsov, *et al.*, Mater. Sci. Eng. B **91–92**, 321 (2002).
13. Yu. M. Altaĭskiĭ, S. F. Avramenko, O. A. Guseva, and V. S. Kiselev, Fiz. Tekh. Poluprovodn. (Leningrad) **13**, 1978 (1979) [Sov. Phys. Semicond. **13**, 1152 (1979)].
14. A. A. Lebedev, Fiz. Tekh. Poluprovodn. (St. Petersburg) **33**, 129 (1999) [Semiconductors **33**, 107 (1999)].
15. L. D. Landau and E. M. Lifshitz, *Course of Theoretical Physics*, Vol. 3: *Quantum Mechanics: Non-Relativistic Theory* (Nauka, Moscow, 1974; Pergamon, New York, 1977).
16. A. A. Lebedev, N. S. Savkina, A. M. Strel'chuk, *et al.*, Mater. Sci. Eng. B **46**, 141 (1997).

Translated by P. Pozdeev

Technical Physics Letters, Vol. 28, No. 12, 2002, pp. 1015–1017. Translated from Pis'ma v Zhurnal Tekhnicheskoĭ Fiziki, Vol. 28, No. 23, 2002, pp. 87–94.
Original Russian Text Copyright © 2002 by Zakharov, Zimnyakov.

Wavelet Analysis of Fluctuations of Laser Radiation Scattered from Interphase Boundaries in Porous Media

P. V. Zakharov and D. A. Zimnyakov
Saratov State University, Saratov, Russia
e-mail: p3axapob@mail.ru

Received July 16, 2002

Abstract—The method of wavelet analysis is used to study fluctuations in the intensity of laser radiation scattered from interphase boundaries in the layer of a porous medium (paper) during evaporation of a volatile liquid with which the layer was impregnated. The analysis was performed using the Morlet wavelet as the base transformation function. The obtained wavelet spectra reflect characteristic features in the development of the evaporation front that correspond to various stages of the process of nonstationary mass transfer in the porous layer–volatile liquid system studied. *© 2002 MAIK "Nauka/Interperiodica".*

Nonstationary mass transfer processes in heterophase systems, such as the process of liquid phase evaporation from a porous medium, can be studied using various methods, in particular, spectral analysis of fluctuations in the intensity of coherent radiation scattered from the system. The role of dynamic scatterers in this case is played by the moving local boundaries between the liquid and gaseous phases in the pores. A "global" interphase boundary formed in the course of evaporation exhibits a fractal character [1–3]. The fractal properties determine the main characteristics of the nonstationary scattering system (representing an ensemble of local interphase boundaries), such as the effective concentration of dynamic scatterers in the analyzed volume [4]. The development of an evaporation front in the layer of a porous medium impregnated with a readily evaporating liquid is followed by degradation of this front as a result of breakage of the system of liquid-saturated pores into separate clusters, which is accompanied by significant changes in the statistical and spectral characteristics of the dynamic scattering signal [4].

An analysis of such nonstationary signals can be performed, for example, by calculating the Fourier spectra of the fragments of signal patterns separated by a sliding window of a certain size. In order to provide for an acceptable time resolution, the width of this window has to be smaller than the characteristic time of variation of the statistical and spectral characteristics studied. However, this method can lead to significant distortions (related to the so-called "leakage" effect) in the shape of the "instantaneous" spectrum of the signal calculated for the values selected inside the sliding window [5]. An alternative approach to the analysis of such essentially nonstationary signals is offered by the study of instantaneous values of the signal amplitude and phase based on the Gilbert transformation [6] or the wavelet transformation [7–11] of the signal using a properly selected base wavelet function.

We have studied the possibility of applying wavelet transformation to an analysis of the signal of dynamic light scattering monitored in the course of the evaporation of a volatile liquid from a porous medium layer. Figure 1a shows a schematic diagram of the experimental setup used to measure the fluctuations of the signal intensity related to the scattering of coherent radiation from the moving local interphase boundaries inside the porous layer. Coherent radiation of a He–Ne laser was focused onto the sample surface by a long-focus lens such that a maximum laser spot size did not exceed 200 μm. The probing radiation power did not exceed 0.5 mW, which excluded the possibility of additional heating of the sample during the experiment.

The scattered light transmitted through the porous layer was detected by a monochrome CCD camera (EDC-1000L, Electrim Corp., USA), without an objective lens, placed behind the sample. The distance from the porous layer to the camera during the experiment was 600 mm. The samples were sheets of paper of various thickness (0.07–0.14 mm) and porosity (0.50–0.85) impregnated with ethyl alcohol or acetone. In the course of the experiment, the CCD camera registered a sequence of patterns corresponding to various realizations of the observed speckle fields. The time interval between shots was significantly smaller than the correlation time of the intensity fluctuations in the speckle pattern studied.

Figure 1b presents typical patterns of the scattered light intensity at arbitrarily chosen points within the detection zone varying with the time of evaporation of the liquid phase from the sample. The time patterns were obtained by preliminary processing of the sequence of images.

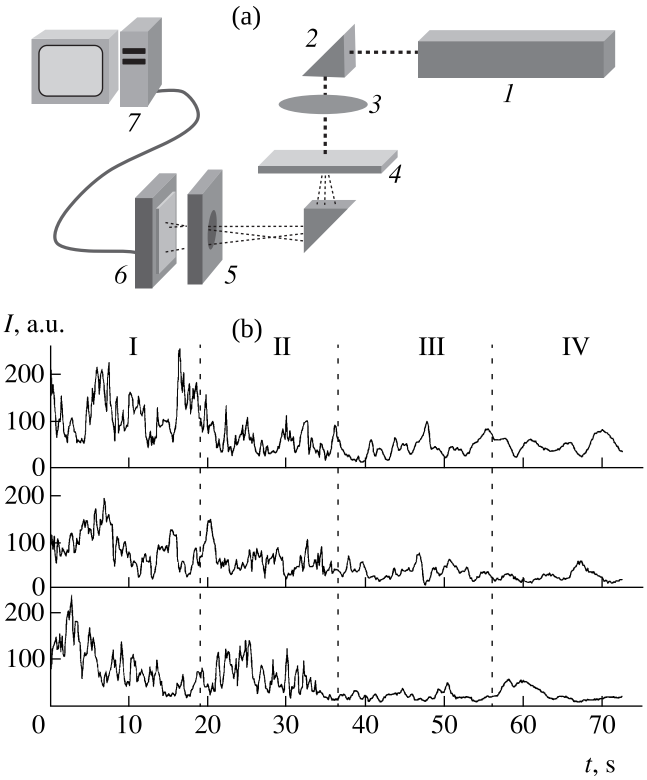

Fig. 1. (a) Schematic diagram of the experimental setup used to study the dynamic light scattering in the course of nonstationary mass transfer: (*1*) monomode He–Ne laser; (*2*) deflecting prism; (*3*) focusing lens; (*4*) sample; (*5*) diaphragm; (*6*) monochrome CCD camera; (*7*) computer. (b) Typical time patterns of the scattered light intensity at various points in the observation plane.

Subsequent processing of the time series of the signal intensity $I_n = I(n\tau)$ ($n = 0, 1, \ldots, N$) was performed by calculating the wavelet coefficients:

$$W_\psi(f, t) = |a(f)|^{-1/2}\tau\sum_{n=0}^{N} I_n\psi^*\left[\frac{n\tau - t_0}{a(f)}\right]. \qquad (1)$$

Here, $W_\psi(f, t_0)$ is the wavelet coefficient for a frequency f [Hz] at a time instant t_0 [s], τ is the period of discretization of the speckle field intensity values, N is the number of elements in the time series, ψ is the base wavelet function (symbol * indicates complex conjugation), and $a(f) = k_0/f$ is the scaling parameter determining the frequency dependence (k_0 is the coefficient determining the relation between time and frequency scales).

The base wavelet function ψ was selected in the form of the Morlet wavelet $\psi(\xi) = \exp(jk_0\xi)\exp(-\xi^2/2)$, which possesses the following properties:

(i) The wavelet transformation with a base function of the Morlet type is closely related to the Fourier transform of the signal studied [7].

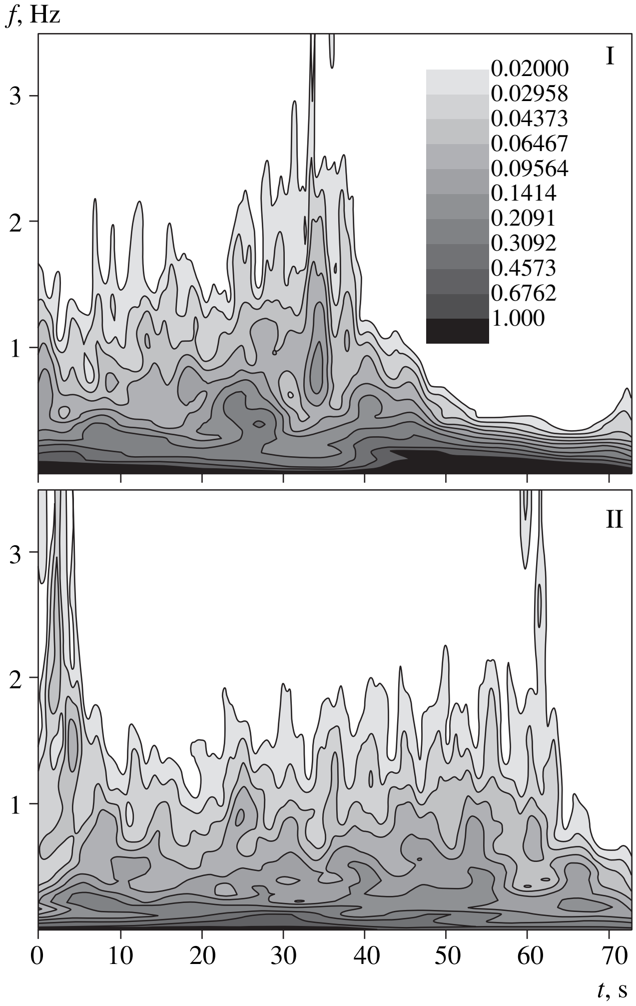

Fig. 2. Typical local spectra of the energy of fluctuations $E(f, t_0)$ in the scattered light intensity for two different samples of paper saturated with acetone: (I) thickness, 88 μm; porosity, 0.56; (II) thickness, 135 μm; porosity, 0.84.

(ii) Use of the Gaussian envelope ensures a high degree of localization of the sliding window used for the analysis of a nonstationary signal in both time and frequency domains and minimizes the frequency–time uncertainty according to Gabor [6].

(iii) Owing to the Gaussian envelope, the Fourier spectrum of the base wavelet function contains no side maxima, which excludes ambiguities in the interpretation of wavelet spectra [10].

The value of $k_0 = 6$ was selected in the preliminary processing stage, proceeding from the condition of maximum resolution in the frequency domain at a minimum acceptable level of noise fluctuations (an increase in k_0 improves resolution at the expense of growing noise).

Using the complex wavelet coefficients, it is possible to calculate a local energy spectrum [10],

$$\begin{aligned} E(f, t_0) &= |W(f, t_0)|^2 \\ &= \mathrm{Re}^2[W(f, t_0)] + \mathrm{Im}^2[W(f, t_0)], \end{aligned} \qquad (2)$$

characterizing the distribution of the process energy over frequencies at various time instants. By analyzing the time variation of $E(f, t_0)$, it is possible to study the dynamics of redistribution of the process energy between various frequency regions.

In this study, the local spectra of fluctuations of the scattered signal intensity E_i obtained for each cell of the CCD matrix were averaged over the whole ensemble ($i = 0, 1, \ldots, 753$). Figure 2 shows the typical local spectra of $E(f, t_0)$ calculated for the signal intensity fluctuations in the course of the liquid phase evaporation from a porous material layer. The spectra are presented for two samples with significantly different values of material porosity and layer thickness. Sample I represents a medium-quality paper for printers, with a relatively smooth surface and a density of 80 g/m^3; sample I is a filter paper characterized by a much greater surface roughness and a higher porosity.

The characteristic frequency band $\Delta f_{0.5}$ of the fluctuations of the scattered light intensity was estimated by determining the frequency interval corresponding to half of the total power of fluctuations. An analysis of this frequency band as a function of the evaporation time t shows that $\Delta f_{0.5}$ exhibits a sharp drop in the initial evaporation stage ($0 < t < 5$ s). This can probably be explained by a transition from the surface to bulk regime of the liquid phase evaporation as a result of degradation of the liquid film on the porous layer surface and the formation of an evaporation front in the volume of the porous medium. The wider frequency band of fluctuations of the scattered light intensity observed in the initial stage for sample II can be explained by the surface front of evaporation being more developed on the rough paper surface.

In the next stage, the evaporation front becomes more developed as it propagates in depth of the porous layer. This is accompanied by spreading of the front and, as a result, by an increase in the number of dynamic scatterers (local boundaries between liquid and gaseous phases in the pores) per unit of effective area of the evaporation front [4]. Under the conditions of multiple scattering of the probing radiation in a porous medium, an increase in the width of the spectrum of fluctuations of the scattered light intensity occurs. Accordingly, the spectral density exhibits an increase in $\Delta f_{0.5}$ up to a maximum value corresponding to the most developed evaporation front (at $t_{\max} \approx 34$ and 53 s for samples I and II, respectively).

In the final stage, the evaporation front exhibits degradation as a result of breakage of the system of liquid-saturated pores into separate clusters. The total number of dynamic scatterers in the region of probing beam scattering sharply drops, which is accompanied by a rapid decrease in the $\Delta f_{0.5}$ value (Fig. 2).

Thus, by the wavelet analysis of fluctuations in the intensity of laser radiation scattered from a porous medium containing liquid and gaseous phases, it is possible to study the evolution of the "global" interphase boundary in the course of nonstationary mass transfer. For quantitative evaluation of the parameters of the scattering system (evaporation front width in various stages of the process, density of local interphase boundaries in the evaporation zone, etc.), one can use a comparison of the results of the wavelet analysis of the signal intensity fluctuations with the results of a statistical modeling of the process of irreversible growth of disordered networks using models analogous to the Eden model [12].

Acknowledgments. This study was supported by the Russian Foundation for Basic Research (project no. 01-02-17493) and by the U.S. CRDF (grant no. REC-006).

REFERENCES

1. *Fractals in Physics*, Ed. by L. Pietronero and E. Tosatti (North-Holland, Amsterdam, 1986; Mir, Moscow, 1988).
2. J. Feder, *Fractals* (Plenum, New York, 1988; Mir, Moscow, 1990).
3. T. M. Shaw, Phys. Rev. Lett. **59**, 1671 (1987).
4. D. A. Zimnyakov, P. V. Zakharov, V. A. Trifonov, and O. I. Chanilov, Pis'ma Zh. Éksp. Teor. Fiz. **74**, 237 (2001) [JETP Lett. **74**, 216 (2001)].
5. Steven W. Smith, *The Scientist and Engineer's Guide to Digital Signal Processing* (California Technical Publ., San Diego, 1999).
6. J. Max, *Methodes et techniques de traitement du signal et applications aux mesures physigues* (Masson, Paris, 1981; Mir, Moscow, 1983).
7. I. Daubechies, *Ten Lectures on Wavelets* (Society for Industrial and Applied Mathematics, Philadelphia, 1992; RKhD, 2001).
8. W. H. Press, S. A. Teukolsky, W. T. Vetterling, and B. P. Flannery, *Numerical Recipes in C: The Art of Scientific Computing* (Cambridge Univ. Press, Cambridge, 1992).
9. P. Goupillaud, A. Grossmann, and J. Morlet, Geoexploration **23**, 85 (1984–1985).
10. N. M. Astaf'eva, Usp. Fiz. Nauk **166** (11), 1145 (1996) [Phys. Usp. **39**, 1085 (1996)].
11. V. I. Vorob'ev and V. G. Gribunin, *Theory and Practice of Wavelet Transforms* (VUS, 1999).
12. M. Eden, in *Proceedings of the Fourth Berkeley Symposium on Mathematical Statistics and Probabilities*, Ed. by F. Newman (Univ. of California Press, Berkeley, 1961), p. 233.

Translated by P. Pozdeev

Technical Physics Letters, Vol. 28, No. 12, 2002, pp. 1018–1020. Translated from Pis'ma v Zhurnal Tekhnicheskoĭ Fiziki, Vol. 28, No. 24, 2002, pp. 1–7.
Original Russian Text Copyright © 2002 by Orlov, Ivina, Drozdov, Alyabina.

Elastic Stress Relaxation in Buffer Layers Based on Porous Strained InGaAs/GaAs Superlattices

L. K. Orlov, N. L. Ivina, Yu. N. Drozdov, and N. A. Alyabina
Institute for Physics of Microstructures, Russian Academy of Sciences, Nizhni Novgorod, Russia
Nizhni Novgorod State University, Nizhni Novgorod, Russia
e-mail: orlov@ipm.sci-nnov.ru

Received April 10, 2002; in final form, July 8, 2002

Abstract—Potential advantages of using relaxed porous InGaAs/GaAs superlattices as buffer layers are considered. The X-ray diffraction patterns and the photoluminescence spectra of multilayer epitaxial InGaAs/GaAs heterostructures upon electrochemical etching are indicative of a partial relaxation of elastic stresses in the component epilayers. The stress relaxation in porous superlattices, used as buffer layers on both porous GaAs and periodic single crystal heterostructures, provides for a small but still significant positive effect related to a decrease in elastic energy accumulated in the growing structure. *© 2002 MAIK “Nauka/Interperiodica”.*

In recent years, considerable effort has been spent in developing methods for obtaining low-defect elastically strained single crystal heterostructures with layer thicknesses and composition parameters exceeding critical values for pseudomorphous growth. In order to solve this problem, it was suggested to use various buffer layers so as to reduce, at least partly, the level of elastic stresses accumulated in heterostructures during the growth process. Under usual conditions, the buffer layer of a solid solution with homogeneous composition allows part of the accumulated elastic energy to be converted into plastic strain energy. This strain is manifested by a network of misfit dislocations with a density of $N_{DN} > 10^5$ cm^{-1} formed at the buffer–substrate interface [1–3], while the buffer layer proper retains a rather high crystal structure perfection: the density of dislocations passing through this layer does not exceed $N_{TD} \sim 10^5$ cm^{-2}.

In most of the known cases, however, this matching procedure is limited by objective factors with respect to the solid solution composition: the content of a variable component in the heterojunction usually cannot exceed ~20% (e.g., for Si in the Ge/GeSi junction [1] or Ge in the Si/SiGe junction [2, 3]). For this reason, the best results are usually obtained using either relaxed layers of variable composition, with the content of one component changing from 0 to 30 at. % [4], or multilayer periodic structures [5]. This allows, in addition to the main effect, the through dislocations to transform, at least partly, into edge dislocations emerging at the crystal side faces.

A less frequently encountered in practice, but still rather promising approach is based on forming a porous layer on the substrate surface and using this layer as a buffer for the subsequent growth of pseudomorphous layers or complex epitaxial heterostructures. Preliminary experiments with the layers of a SiGe solid solution grown on a porous Si substrate [6] and the layers of an InGaAs ternary compound grown on a porous GaAs substrate [7] gave promising results, showing the best structural and electrical characteristics of the obtained heterostructures. The improved crystal structure of the epitaxially grown system of pseudomorphous layers is probably due to decreased elastic action of the substrate. This decrease is related to a reduced area of contact (by edges of the pore spacers) between the growing heterocomposition and the porous buffer layer formed on the substrate surface. Another favorable circumstance is the facilitated sink of misfit dislocations, unavoidably appearing in the growing structure, to the well-developed surface of the porous layer.

Apparently, a new qualitative level in the epitaxial growth of strained heterostructures—with the layer thicknesses and component ratios significantly exceeding the values reached previously—can be provided by combining the advantages of all the buffer layer types mentioned above. To check for this, it is only necessary to show that the creation of a porous surface layer in the preliminarily grown pseudomorphous or partly relaxed heterocomposition can relieve at least partly the elastic energy accumulated in the strained lattice of a single crystal layer. This study was aimed at practical verification of this proposal.

The initial structure, which served as the buffer for growing a more complicated heterocomposition, was a multilayer pseudomorphous periodic $In_{0.2}Ga_{0.8}As$/GaAs(100) structure. Grown on a gallium arsenide substrate, the buffer structure comprised 10 periods, each consisting of a 10- to 15-nm-thick InGaAs layer and a ~70-nm-thick GaAs layer. This structure was characterized by dislocations propagating toward the surface, the total density of which (estimated by etching pits) did not exceed 10^4–10^5 cm^{-2}. A porous superlattice was formed using the conventional method of electrochemical etching in an ethanol–HF mixture under illumination. The level of elastic stresses in the sample structure before and after etching was estimated from the X-ray diffraction data and from the shift of peaks in the photoluminescence spectra.

The X-ray diffraction measurements in the vicinity of a GaAs(400) reflection were performed on a DRON-4 diffractometer using Ge(400) monochromated Cu$K_{\alpha 1}$ radiation. Figure 1 (curve *1*) shows a typical θ/2θ X-ray diffractogram of the initial periodic structure. An analysis of this spectrum shows the presence of a long-period superlattice (manifested by small oscillations of the envelope) and gives evidence of a complicated composition profile of the $In_{0.17}Ga_{0.83}As$ layers in the heterostructure, which is not a significant factor in the case under consideration. The X-ray diffraction pattern observed for a porous superlattice (curve *2*) differs only slightly from the initial diffractogram. This fact indicates that even a rather long etching of the sample did not lead to degradation of the crystal structure of the layers. The fitting of a calculated diffractogram to the experimental pattern using recurrent formulas of the dynamic approximation of the X-ray scattering theory leads to R = 20% (which corresponds to a residual elastic strain value of *RES* = 80%). This result, even despite the relatively small magnitude of relaxation, is essential, especially in view of the fact that the creation of a buffer layer based on pure porous GaAs leads to a decrease in the lattice parameter as compared to that of single crystal GaAs [7], which even increases the elastic energy accumulated in the InGaAs layer grown on this buffer.

The fact of elastic stress relaxation in a porous buffer superlattice is even better illustrated by a comparative analysis of the photoluminescence (PL) spectra of single crystal and porous samples. Figure 2 shows the emission peaks due to the radiative recombination in quantum-confined InGaAs layers measured at the liquid nitrogen temperature. A comparison of the positions of peaks *1* (single crystal) and *2* (porous structure) reveals a small shift of the PL maximum within 0.005–0.008 eV (depending on the etching conditions) toward longer wavelengths, which is indicative of a decrease in the level of elastic stresses accumulated in the initial sample structure. The PL peak position is determined (with neglect of the effect of quantum confinement in the potential wells) by the composition of the InGaAs ternary solid solution and by the strain (contraction) in the plane of the structure. In the case under consideration, an additional shift of the PL peak could appear on the passage from single crystal to porous InGaAs structure as a result of the spatial confinement in the planes of the superlattice [8]; however, t this effect was excluded by using a low etching rate.

Let us estimate the PL shift toward shorter wavelength caused by elastic straining of the $In_{0.2}Ga_{0.8}As$ lattice structure. A total shift of the PL peak is related to a change in the bandgap width of the ternary semiconductor compound due to three-dimensional compression (this factor increases the bandgap) and uniaxial tensile stress in the growth direction (this leads to splitting of the degenerate valence subbands, thus decreasing the bandgap). In a single crystal structure, the former bulk effect dominates, whereby the bandgap width in the $In_{0.2}Ga_{0.8}As$ layer increases from E_g = 1.18 eV [9] (at T = 77 K) for the unstrained bulk material to E_g = 1.24 eV for an elastically strained pseudomorphous layer grown on a GaAs substrate [10]. The decrease in the bandgap width, related to the release of accumulated elastic energy in the porous layers, amounts to 0.005–0.008 eV (Fig. 3). A small (0.005–0.008 eV) longwave shift of the PL peak observed for the porous superlattice is evidence of a small (within 10%) but still significant relaxation of the stain accumulated in the superlattice structure, which agrees (to

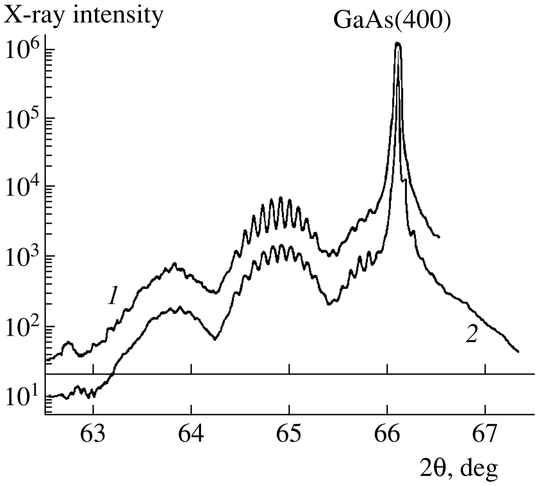

Fig. 1. X-ray diffraction patterns of an InGaAs/GaAs superlattice measured (*1*) before and (*2*) after a 40-min electrochemical etching.

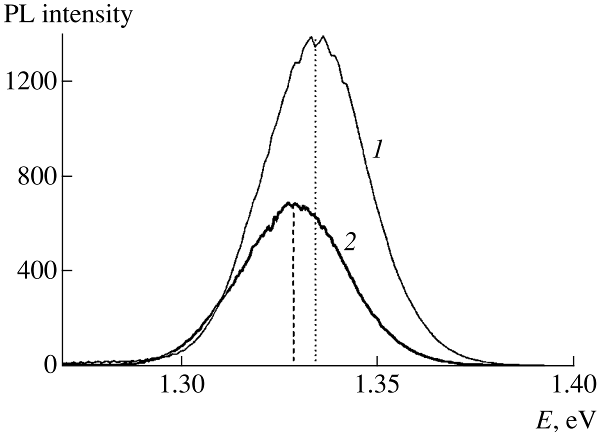

Fig. 2. Typical PL spectra of an InGaAs/GaAs superlattice measured at 77 K (*1*) before and (*2*) after a 40-min electrochemical etching.

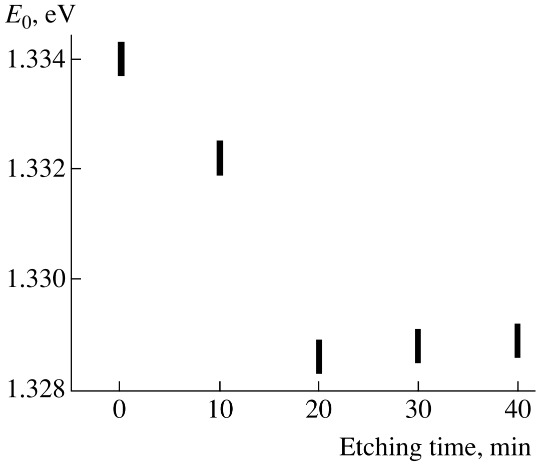

Fig. 3. A plot of the PL peak position versus etching time.

within the experimental error) with the X-ray diffraction data.

Thus, both the X-ray diffraction pattern and the PL peak shift observed for the electrochemically etched multilayer epitaxial InGaAs/GaAs heterostructures are indicative of elastic stress relaxation in this system. This fact shows that, by using porous superlattices as buffer layers, it is possible to obtain a small but still significant positive effect related to a decrease in accumulated elastic energy for the porous layers of both GaAs and periodic single crystal heterostructures.

Acknowledgments. The authors are grateful to B.N. Zvonkov for growing the initial sample structures and to Prof. E.S. Demidov (Nizhni Novgorod State University) and Yu.N. Buzynin (Institute for Physics of Microstructures) for fruitful discussions. This study was supported by the Russian Foundation for Basic Research, project nos. 01-02-16778, 01-02-06232, and 02-02-06577.

REFERENCES

1. M. G. Mil'vidskii, V. I. Vdovin, L. K. Orlov, *et al.*, in *Growth of Crystals* (Consultants Bureau, New York, 1996), Vol. 20, p. 13.
2. L. K. Orlov, V. A. Tolomasov, A. V. Potapov, and V. I. Vdovin, Izv. Vyssh. Uchebn. Zaved., Ser. Mater. Élektron. Tekh., No. 2, 30 (1998).
3. T. G. Yugova, V. I. Vdovin, M. G. Milvidskii, *et al.*, Thin Solid Films **336** (1, 2), 112 (1999).
4. E. A. Fitzgerald and S. B. Samavedam, Thin Solid Films **294** (1, 2), 3 (1997).
5. S. V. Sorokin, S. V. Ivanov, G. N. Mosina, *et al.*, Inst. Phys. Conf. Ser. **155**, 219 (1997).
6. V. Yakovtseva, N. Vorozov, L. Dolgyi, *et al.*, Phys. Status Solidi A **182**, 195 (2000).
7. Yu. N. Buzynin, S. A. Gusev, Yu. N. Drozdov, *et al.*, Poverkhnost, No. 5, 40 (1996).
8. L. K. Orlov and N. L. Ivina, Pis'ma Zh. Éksp. Teor. Fiz. **75**, 584 (2002) [JETP Lett. **75**, 492 (2002)].
9. O. Madelung, *Physics of III–V Compounds* (Wiley, New York, 1964; Mir, Moscow, 1967).
10. L. K. Orlov, N. L. Ivina, R. A. Rubtsova, and Yu. A. Romanov, Fiz. Tverd. Tela (St. Petersburg) **42** (3), 537 (2000) [Phys. Solid State **42**, 548 (2000)].

Translated by P. Pozdeev

Technical Physics Letters, Vol. 28, No. 12, 2002, pp. 1021–1023. Translated from Pis’ma v Zhurnal Tekhnicheskoĭ Fiziki, Vol. 28, No. 24, 2002, pp. 8–14.
Original Russian Text Copyright © 2002 by Mardasova, Abdulvakhidov, Burakova, Kupriyanov.

The Effect of a Constant Electric Field on the Structural Parameters of Ferroelectric $PbSc_{0.5}Nb_{0.5}O_3$ Crystals

I. V. Mardasova, K. G. Abdulvakhidov, M. A. Burakova, and M. F. Kupriyanov
Rostov State University, Rostov-on-Don, Russia
e-mail: kam@rnd.runnet.ru

Received July 10, 2002

Abstract—The effect of a constant electric field on the polarization and structural parameters of ferroelectric lead scandium niobate ($PbSc_{0.5}Nb_{0.5}O_3$) crystals was studied using X-ray diffraction. Application of a constant electric field leads to splitting of the Bragg diffraction peaks. It is shown that this behavior is most probably explained by the formation of a new phase. *© 2002 MAIK “Nauka/Interperiodica”.*

Numerous investigations of lead scandium niobate $PbSc_{0.5}Nb_{0.5}O_3$ (PSN) have shown that the physical properties of PSN crystals depend on the sample prehistory. Variations in the properties of PSN crystals upon high-temperature annealing were previously explained by changes in the order of Sc and Nb atoms occupying positions B of perovskite structure (see, e.g., [1–3]). However, we recently demonstrated [4, 5] that the effects of annealing are more likely due to structural changes on macroscopic (crystal and domain structure) and mesoscopic (block structure) levels.

It is also known that application of a constant electric field to perovskite ferroelectrics leads to modification of the domain structure [6], induces the formation of a new phase [7], and produces a strong piezoelectric deformation of the surface layer [8–10].

We studied by X-ray diffraction the process of polarization switching and determined changes in the structural parameters of PSN crystals under the action of a constant electric field at room temperature.

The PSN crystals were grown by method of bulk crystallization of a solution melt in a temperature range from 1200 to 1117°C. The samples had the shape of rectangular parallelepipeds with linear dimensions from 10 μm to 2.5 mm and the facet orientations (100), (010), and (001). As is known, PSN crystals under normal conditions belong to a rhombohedral system (space group $R3m$) and exhibit spontaneous polarization P_s in the [111] direction of the perovskite unit crystal cell ($P_x = P_y = P_z$).

The X-ray diffraction measurements were performed on an HZG-4B diffractometer equipped with a special sample holder, which allowed the electric field to be applied to the sample and the crystal to be adjusted in the course of measurements. The profiles of the (400) diffraction reflection were measured by $\theta/2\theta$ scanning with a step of 0.005° and a data acquisition time of 2 s at each point. The error of determination of the lattice parameters was ±0.0001 Å. The diffractometer operation and data processing regimes were controlled by a computer. The polarization switching was characterized by changes in the parameters of diffraction profiles under the action of a constant electric field applied in the [100], [010], and [111] directions.

Application of a constant electric field in the [100] direction of a PSN single crystal led to a shift of the (400) Bragg diffraction peak toward smaller angles, which corresponds to an increase in the lattice parameter Δ. As can be seen from the data presented in Fig. 1, the lattice parameter exhibits a nonmonotonic variation depending on the applied field strength E. This is explained by crystal straining as a result of electrostriction. The diffraction profile retains a symmetric shape, while both the halfwidth β and the intensity of the peak (I) exhibit nonmonotonic changes in the interval of E values studied. All five PSN crystals in the series studied showed analogous results.

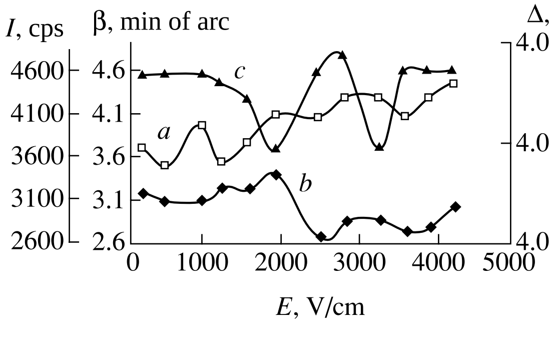

Fig. 1. Plots of the (a) lattice parameter, (b) peak intensity, and (c) peak halfwidth of the (400) diffraction reflection versus the strength of an electric field applied in the [100] direction of a PSN crystal.

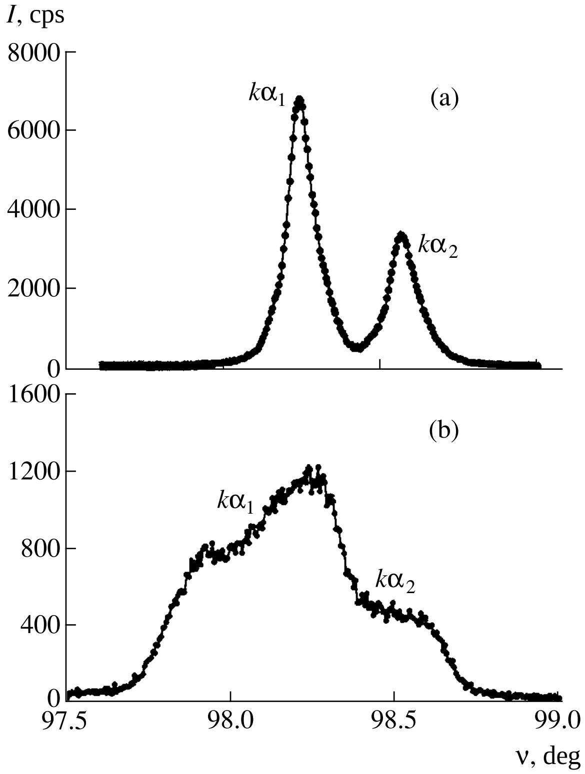

Fig. 2. X-ray diffraction profiles in the region of the (400) reflection for a PSN crystal (a) before and (b) after application of a constant electric field in the [010] direction.

According to the results of polarization-optical measurements, the application of a constant electric field with a strength of 1–4 kV/cm leads to the formation of 71° and 180° domains, with the boundaries representing (100) and (110) twin planes, respectively. A field with $E < 1$ kV/cm gives rise to the formation of 180° domains; as the field strength increases, these domains grow through the crystal in the direction parallel to the field. A change in the field direction to opposite does not significantly change the above pattern. Subsequent etching of the PSN crystals in orthophosphoric acid showed that the domain structure was not the same in various regions of the samples. Neither the interval of field strengths indicated above nor the range of variation of the structural parameters was strictly the same for different PSN crystals and exhibited variations depending on the density of defects, degree of homogeneity, and the temperature interval of crystallization of the samples.

The study of variation of the (400) diffraction reflection profile for the electric field applied in the [010] and [111] directions of the PSN crystals showed analogous behavior. For this reason, the results presented below refer to the samples polarized in the [010] axis.

Figure 2a shows the (400) diffraction reflection profile of a PSN crystal not subjected previously to the field action. Upon the application of a constant electric field, the reflection profile changes neither in shape nor in angular position as the field strength is increased to 1000 V/cm. In such a weak field, the behavior of the PSN crystal is analogous to that of a usual dielectric characterized by a linear dependence of polarization on the field strength. As a rule, exposure to such fields leads to the nucleation of new domains in the samples.

As the applied field strength increases in the interval from 1000 to 5000 V/cm, there appears an anomaly on the (400) diffraction reflection profile from the side of large angles, which makes the diffraction profile asymmetric. In this range of field strengths, the dependence of P_s on E is nonlinear and the number of domains involved in the polarization switching increases with the E value.

When the applied field strength exceeds 5000 V/cm, the shape of the (400) diffraction reflection profile changes from the side of both large and small angles: there appears an additional maximum corresponding to a greater lattice parameter a (Fig. 2b). A further increase in the field strength does not significantly change the polarization. Here, the field action is mostly manifested in increasing deformation of the crystal lattice: depending on the orientation of P_s components (parallel or antiparallel to the field) in the adjacent 180° domains, the field produces either extension or contraction of these domains. This is one of the possible reasons for splitting of the (400) diffraction reflection (Fig. 2b). In the PSN crystals studied, the mutual disorientation of the adjacent 180° domains varied depending on the applied field strength and reached about 5 minutes of arc for the maximum E values.

Another, more probable reason for the observed splitting of the (400) diffraction reflection was that the PSN crystals studied were heterophase, possessing coexisting regions of different phases with close values of the free energy. In such crystals, the growth of one or another phase can be initiated by various external factors, such as electric field, temperature, pressure, etc. The results of preliminary investigations of the phase transitions in PSN crystals with and without an applied electric field showed that the crystals grown in the indicated temperature range are inhomogeneous and contain regions occupied by different phases. In some of the samples, the X-ray diffraction measurements revealed the presence of two different phases existing at room temperature even in the absence of external factors. This accounts for a difference in the lattice parameters reported previously [4].

As can be seen from the data presented in Fig. 3, the (400) diffraction reflection intensity exponentially depends on the applied field strength. This is explained by the fact that, for the field strength exceeding 1000 V/cm, small domains exhibit lateral motion and growth. An increase in the linear dimensions of domains above 1–2 μm gives rise to the primary extinc-

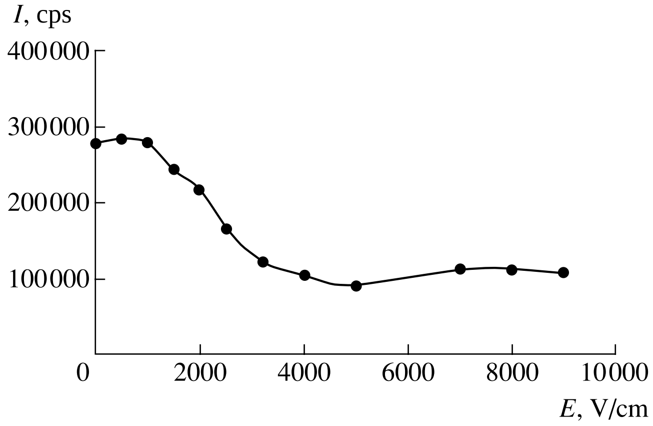

Fig. 3. Plot of the integral peak intensity of the (400) diffraction reflection versus strength of an electric field applied to a PSN crystal.

tion. As a result, the reflection ability decreases as described by the kinematic theory [11]:

$$P = \frac{Q}{2\mu p}\frac{\tanh 2t\sqrt{Q\cot\theta/\lambda(1+\cos^2 2\theta)}}{2t\sqrt{Q\cot\theta/\lambda(1+\cos^2\theta)}},$$

where ρ is the crystal density, μ is the bulk absorption coefficient, t is the crystal thickness, and Q is the integral reflection ability per cm^3.

Thus, the results of our experiments are indicative of the presence of inhomogeneous regions in the PSN crystals with the corresponding values of the free energy, coercive field, and relaxation time. The observed jumplike variations in the structural parameters are due to the inhomogeneity of polarization over the crystal volume. Attempts at interpreting this behavior in terms of the crystallochemical order–disorder in the arrangement of cations in the oxygen octahedra seem to be incorrect without thorough characterization of the real crystal structure prior to the action of external factors.

In concluding, it should be noted that the splitting of diffraction profiles in the region of the Bragg maxima is neither a near-electrode nor a unipolar effect. An analogous effect has to be observed on the electrode side as well. Probably, the splitting effect in our case is screened by strong electric fields in the near-electrode region.

REFERENCES

1. C. G. F. Stenger and A. J. Burggraaf, Phys. Status Solidi A **61**, 275 (1980).
2. C. G. F. Stenger and A. J. Burggraaf, Phys. Status Solidi A **61**, 653 (1980).
3. A. A. Bokov, I. P. Raevskiĭ, and V. G. Smotrakov, Fiz. Tverd. Tela (Leningrad) **25** (7), 2025 (1983) [Sov. Phys. Solid State **25**, 1168 (1983)].
4. K. G. Abdulvakhidov and M. F. Kupriyanov, Kristallografiya **41** (6), 1066 (1996) [Crystallogr. Rep. **41**, 1013 (1996)].
5. K. G. Abdulvakhidov, I. V. Mardasova, and T. P. Myasnikova, Fiz. Tverd. Tela (St. Petersburg) **43** (3), 489 (2001) [Phys. Solid State **43**, 508 (2001)].
6. E. G. Fesenko, *Perovskite Family and Ferroelectricity* (Atomizdat, Moscow, 1972).
7. O. G. Fesenko, *Phase Transitions in Ultrastrong Fields* (Rostov-on-Don, 1984), p. 169.
8. V. P. Dudkevich, I. N. Zakharchenko, and V. S. Bondarenko, Kristallografiya **18** (5), 1095 (1973) [Sov. Phys. Crystallogr. **18**, 690 (1973)].
9. V. P. Dudkevich, I. N. Zakharchenko, and E. G. Fesenko, Fiz. Tverd. Tela (Leningrad) **15** (9), 2766 (1973) [Sov. Phys. Solid State **15**, 1838 (1973)].
10. V. P. Dudkevich, I. N. Zakharchenko, and A. N. Vas'kin, Kristallografiya **20** (1), 82 (1975) [Sov. Phys. Crystallogr. **20**, 45 (1975)].
11. A. Guinier, *Theórie et technique de la radiocristallographie* (Dunod, Paris, 1956; Fizmatgiz, Moscow, 1961).

Translated by P. Pozdeev

Technical Physics Letters, Vol. 28, No. 12, 2002, pp. 1024–1026. Translated from Pis'ma v Zhurnal Tekhnicheskoĭ Fiziki, Vol. 28, No. 24, 2002, pp. 15–19.
Original Russian Text Copyright © 2002 by Zaĭko.

A Model of Liquid Flow in a Channel with Elastic Walls

Yu. N. Zaĭko
Volga Region Academy of State Service, Saratov, Russia

Received July 10, 2002

Abstract—It is suggested to describe a liquid flow in a cylindrical round channel with elastic walls in terms of a two-fluid model used to describe the flow of He II in narrow capillaries near absolute zero. The idea is based on a similar (phonon-like) shape of the spectrum of elementary excitations at small wavenumbers k. The calculations show that the density ρ_n of a normal (i.e., viscous) liquid component (water in a steel tube) at 300 K is about 50 times smaller than the total density. This explains the paradox related to flow in a round tube for which anomalously large Reynolds numbers ($\mathrm{Re} \sim 10^5$) are observed. Since $\mathrm{Re} \sim \rho_n$, real Reynolds numbers must also be about 50 times as small, that is, on the same order of magnitude as those for a flow between planes under otherwise equal conditions. A physical reason for the appearance of superfluidity at high (~300 K) temperatures is a decrease in repulsion between small density fluctuations in the liquid, which is related to their interaction being screened by elastic waves in the channel walls. © *2002 MAIK "Nauka/Interperiodica".*

Recently [1], a generalized variant of the local reaction model [2] was developed, which described a flow of ideal liquid in a narrow cylindrical channel of round cross section having walls resistant only to extension (via additional resistance to bending). The initial system of equations can be written as [1]

$$\begin{aligned} A_t + (Av)_x &= 0, \\ v_t + vv_x + p_x &= 0, \qquad (1) \\ A_{tt} + RA_{xxxx} + A - p &= 0, \end{aligned}$$

where $A = S/\pi a^2$, $S = \pi r^2$ is the cross section of the channel with radius r, a is the equilibrium value of r, v is the longitudinal velocity component (directed in the x axis), p is the pressure, $R = \rho^2/[3(1-\mu^2)\rho_0^2]$ is the dimensionless cylindrical rigidity, ρ is the liquid density, ρ_0 is the channel wall material density, μ is the Poisson coefficient [3], t is dimensionless time, and subscripts denote partial derivatives. Equations (1) were rendered dimensionless by using the following quantities as the time, length, and pressure units, respectively:

$$T = \sqrt{\frac{\rho_0 a^2}{E}}, \quad L = \sqrt{\frac{\rho_0 a d}{2\rho}}, \quad P = \frac{Ed}{2a}, \qquad (2)$$

where d is the wall thickness and E is the Young modulus of the wall; all variables (A, v, and p) are considered as functions of the time t and longitudinal coordinate x.

An analysis of the pattern of linear waves propagating in the system described by Eqs. (1) and their stability for supersonic flows with constant velocity components $v_0 > 1$ was performed previously [1]. The dispersion curves of frequency versus wavenumber, $\omega = \omega(k)$, for the interval of velocities $v_0 \le 1$ are presented in the figure. A characteristic feature of these curves is the phonon-like portion $\omega = k(v_0 \pm 1) \sim k$ for $k \ll 1$ (the branch corresponding to the minus sign in parentheses is not depicted) and the local (roton-like) minimum at $k = k_\mathrm{m}$ for the velocity of sound ($v_0 \approx 1$). At this minimum, the elementary excitation energy varies as $\varepsilon(q) = \hbar\omega \approx \Delta + (q - q_\mathrm{m})^2/2\mu$, where $q = \hbar k$ is the momentum and $\hbar$ is the Planck constant. For illustration, consider the values $q_\mathrm{m} = \hbar k_\mathrm{m}$, $\Delta = \hbar\omega_\mathrm{m}$, and $\mu = (d^2\varepsilon/dq^2)^{-1}$ for a flow of water in a steel tube with radius a = 1 m and wall thickness $d = 5 \times 10^{-3}$ m (curve *1* in the figure):

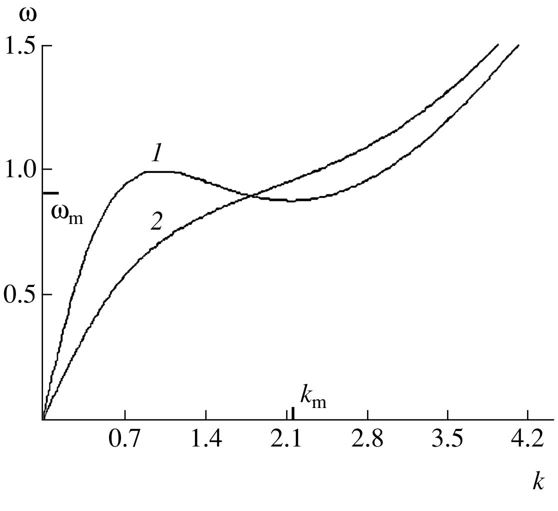

The spectra of excitations $\omega = \omega(k)$ calculated for water flowing in a steel tube with rigidity $R = 5.8 \times 10^{-3}$: (*1*) at velocity of sound $v_0 = 1$ ($k_\mathrm{m} = 2.145$, $\omega_\mathrm{m} = \omega(k_\mathrm{m}) = 0.88$, $\omega''(k_\mathrm{m}) = 0.376$); (*2*) at subsonic velocity $v_0 = 1 \times 10^{-3}$.

1063-7850/02/2812-1024$22.00 © 2002 MAIK "Nauka/Interperiodica"

$\Delta \approx 0.94 \times 10^{-29}$ J $\approx 0.68 \times 10^{-6}$ K, $q_m \approx 0.72 \times 10^{-32}$ kg m/s $\approx 0.68 \times 10^2\, \hbar$/m, and $\mu \approx 0.28 \times 10^{-35}$ kg $\approx 0.93 \times 10^{-10}$ m H_2O. For these values, the characteristic time and length units (2) are $T = 0.987 \times 10^{-5}$ s and $L = 3.12 \times 10^{-2}$ m, which corresponds to the velocity of sound $c = L/T = 3.16 \times 10^3$ m/s.

The aforementioned features of the $\omega(k)$ spectrum give sufficient ground to describe the liquid flow in a tube with elastic walls in terms of the so-called two-fluid model [4] developed for the description of helium II flowing in narrow capillaries at temperatures close to absolute zero. In this model, the total density $\rho = \rho_n + \rho_s$ was considered as the sum of densities of the normal (ρ_n) and superfluid (ρ_s) components. In turn, the density of the normal component was presented as $\rho_n = \rho_n^{ph} + \rho_n^r$, where ρ_n^{ph} and ρ_n^r are the phonon and roton parts related to the corresponding excitations and described by the corresponding parts of the $\omega = \omega(k)$ spectrum.

In order to calculate the latter parts, let us use an expression for the number of elementary excitations in a Bose fluid [4]:

$$n(q) = \frac{1}{e^{\varepsilon(q)/\Theta} - 1} \approx \frac{\Theta}{\varepsilon}, \quad \Theta \gg \varepsilon, \tag{3}$$

where Θ is the absolute temperature (here and below, the Boltzmann constant is taken equal to unity).

For the phonon part of the density, we obtain

$$\rho_n^{ph} = \frac{4}{3}\frac{T^2}{L^2}\frac{E^{ph}}{(v_0 + 1)^2} = \frac{4}{3}\frac{T^2}{L^2}\frac{\Theta}{m(v_0 + 1)^2}\rho, \qquad E^{ph} = N_0 \nu \Theta, \tag{4}$$

where N_0 is the concentration of molecules, ν is the number of atoms in a molecule, E^{ph} is the energy per unit volume of the phonon gas at high temperatures [4], ρ is the liquid density, and m is the molecular mass. In the above example at $\Theta = 300$ K, $\rho_n^{ph} \approx 0.0046\rho$ (for $v_0 = 1$) and $\rho_n^{ph} \approx 0.018\rho$ (for $v_0 \ll 1$).

The roton part ($v_0 = 1$) is as follows [4]:

$$\rho_n^r = \frac{4\pi}{3}\Theta\int_0^\infty \frac{q^4}{\varepsilon^2}\frac{dq}{(2\pi\hbar)^3} \approx \frac{1}{6\pi^2}\frac{T^2}{L^5}\frac{q_m^4}{\omega_m^{3/2}\omega_m''}\Theta \approx 1.15\frac{T^2}{L^5}\Theta \ [\mathrm{kg/m^3}], \tag{5}$$

which corresponds to $\rho_n^r \sim 0.94 \times 10^{-23}$ kg/m^3 in the above example. For the density of rotons defined as $N = \rho_n^r/\mu$, we obtain

$$N = \frac{\rho_n^r}{\mu} = \frac{1}{6\pi^2\hbar}\frac{T}{L^3}\frac{q_m^4}{\omega_m^{3/2}}\Theta = 0.43\frac{T}{\hbar L^3}\Theta \ [\mathrm{m^{-3}}].$$

In the above example, this yields $N \approx 3.36 \times 10^{12}$ m^{-3}, which corresponds to an average roton spacing of $r_0 = (N)^{-1/3} \approx 0.67 \times 10^{-4}$ m. Thus, in this example, $\rho_n^{ph} \ll \rho$ and $N \ll 0.334 \times 10^{29}$ m^{-3} (the concentration of molecules in water). Therefore, we can use the ideal gas approximation. Expression (3) for $n(q)$ obtained in the 3D case is also applicable (at least, for phonons), since the velocity of sound in the system under consideration is sufficiently isotropic: the transverse velocity $c_\perp = 1.1$–1.3×10^3 m/s coincides in order of magnitude with the longitudinal velocity used above.

Formally speaking (with neglect of the wave decay and merge processes), we have to take into account the contribution from the part of the spectrum with $\omega \sim (R)^{1/2}k^2$ for $k \gg 1$. The calculation shows that these excitations contribute with $\rho_n \approx 10^5\rho_n^r$, so that in any case, $\rho_n \approx \rho_n^{ph}$.

From the standpoint of physics, the appearance of superfluidity at high (~300 K) temperatures is related to the following circumstance. The mechanism of energy transfer [1] from liquid flow to elastic waves in the wall leads to a decrease in repulsion between like density fluctuations in the liquid. This can be demonstrated by writing the second equation in system (1) as $dv/dt = -p_x = -(A + A_{tt} + RA_{xxxx})_x = -(1 - \omega^2 + Rk^4)A_x = -(v_0 - \omega/k)^2A_x$. The result is obtained using a dispersion relation following from (1): $(1 - \omega^2 + Rk^4)k^2 - (kv_0 - \omega)^2 = 0$ [1]. A comparison of the modified equation of motion to that written with neglect of the wall mass and rigidity, $dv/dt = -A_x$ (it should be recalled that A_x plays the role of density in this model), leads to the conclusion that the interaction of density waves in the flow with the elastic waves in the wall leads to the aforementioned decrease in the repulsion of fluctuations, provided that $v_0 < v_{0s} = \min\{\omega(k)/k\}$ (violation of the latter condition leads to a loss of the system stability). As a result, a certain fraction of the liquid acquires superfluid properties, which implies the ability to flow via channels without losing energy to friction (viscosity) at a velocity satisfying the above condition [4]. In the case corresponding to curve *1* in the figure, this corresponds to $v_{0s} = 3.373 \times 10^{-1}$. Another manifestation of a decrease in the repulsion of fluctuations is the possibility of soliton propagation in the system studied [2].

Within the framework of the two-fluid model, the second equation in system (1) describes the velocity $v \equiv v_s$ and the pressure $p \equiv p_s$ of the superfluid component. An equation for the normal component u can be derived by assuming this component (as well as the superfluid one) to be incompressible, ignoring dissipation (entropy S = const), and retaining a single term, reflecting the normal component viscosity η, in the momentum flux density tensor. In the dimensionless units adopted, we obtain [3]

$$\begin{gathered}\frac{\rho_n}{\rho_s}[u_t + uu_x] = -p_{nx} + \nu u_{xx}; \quad \rho_s \equiv \rho, \\ \nu = \frac{2\eta}{d\sqrt{E\rho_0}},\end{gathered} \tag{6}$$

where p_n is the pressure of the normal component ($p = p_s + p_n$). In the particular case under consideration, $\rho_n/\rho_s \sim 10^{-2}$ and $\nu \sim 10^{-8}$, which implies that $p_n \ll p_s$ and allows the p_n term to be omitted in the last equation of system (1).

The results obtained above solve the paradox related to flow in a round tube for which anomalously large Reynolds numbers ($\mathrm{Re}^{\exp} \sim 10^5$) are observed [3]. Since $\mathrm{Re} = v_0 a\rho/\eta$, real Reynolds numbers are also about two orders of magnitude lower: $\mathrm{Re}/\mathrm{Re}^{\exp} = \rho_n/\rho \sim 10^{-2}$.

REFERENCES

1. Yu. N. Zaĭko, Pis'ma Zh. Tekh. Fiz. **27** (16), 27 (2001) [Tech. Phys. Lett. **27**, 677 (2001)].
2. G. L. Lamb, Jr., *Elements of Soliton Theory* (Wiley, New York, 1980; Mir, Moscow, 1983).
3. L. D. Landau and E. M. Lifshitz, *Course of Theoretical Physics*, Vol. 6: *Fluid Mechanics* (Nauka, Moscow, 1986; Pergamon, New York, 1987).
4. E. M. Lifshitz and L. P. Pitaevskiĭ, *Course of Theoretical Physics*, Vol. 5: *Statistical Physics* (Nauka, Moscow, 1978; Pergamon, New York, 1980), Part 2.

Translated by P. Pozdeev

Technical Physics Letters, Vol. 28, No. 12, 2002, pp. 1027–1029. Translated from Pis'ma v Zhurnal Tekhnicheskoĭ Fiziki, Vol. 28, No. 24, 2002, pp. 20–24.
Original Russian Text Copyright © 2002 by Sokolovskiĭ.

Negative Differential Resistance in a Reverse-Biased Diode with Inhomogeneous Base

B. S. Sokolovskiĭ
Lviv National University, Lviv, Ukraine
e-mail: sokol@iap.franko.lviv.ua

Received July 18, 2002

Abstract—The possibility of a negative differential resistance (NDR) region appearing in the reverse branch of the current–voltage characteristic of a semiconductor diode with a wide-bandgap layer in the base is theoretically predicted. The NDR formation is related to the fact that increasing reverse bias leads to a decrease in the thermal production of charge carriers in the narrow-bandgap part of the base (with a thickness on the order of the Debye screening length). It is shown that the NDR region appears, provided that the carrier lifetime in the diode base is determined by the Auger processes. *© 2002 MAIK “Nauka/Interperiodica”.*

Previously [1], an analytical model of a semiconductor diode with a wide-bandgap layer in the base was developed. By significantly decreasing the reverse diffusion current, this wide-bandgap layer increases the efficiency of various devices employing *p*–*n* junctions, in particular, detectors of weak electromagnetic radiation fluxes. It is theoretically proved below that, in cases when the distance between the wide-bandgap layer and the space charge region is on the order of the Debye screening length, a negative differential resistance (NDR) region can appear in the reverse branch of the current–voltage characteristic of the semiconductor diode.

Consider an asymmetric n^+–p junction, the *p*-type base of which (with an acceptor concentration of N_a) contains a wide-bandgap layer adjacent to the ohmic contact. Let the distance d_{ps} from this layer to the space charge region be much smaller than the electron diffusion length L_n and assume that the bandgap difference between the wide- and narrow-bandgap parts of the base is sufficiently large, so that the diffusion current in the *p*-type base is determined only by the charge carrier production rate G_{ps} (more precisely, G_{ps} is the difference between the carrier production and recombination rates) in the narrow-bandgap part of the base. For $d_{ps} \ll L_n$, the densities of nonequilibrium electrons (n) and holes (p) in the narrow-bandgap part of the base are virtually constant:

$$n \cong \frac{n_{is}^2}{N_a}\exp\left(-\frac{e|U|}{kT}\right), \quad p \cong N_a, \tag{1}$$

where n_{is} is the intrinsic carrier density in the narrow-bandgap part of the base and U is the reverse bias voltage applied to the *p*–*n* junction. Taking this into account, the reverse diffusion current related to the carrier production in the *p*-type base can be expressed through the reduced carrier production rate g_{ps} in the narrow-bandgap part of the base:

$$\begin{aligned} j_p(U) &= -ed_{ps}G_{ps} \equiv ed_{ps}g_{ps}\frac{np - n_{is}^2}{n_{is}^2} \\ &= ed_{ps}g_{ps}\left[\exp\left(-\frac{e|U|}{kT}\right) - 1\right]. \end{aligned} \tag{2}$$

A special feature of the current–voltage characteristic determined by the diffusion current transfer mechanism is the appearance of an NDR region on the reverse branch of this characteristic. The appearance of the NDR is related to a decrease in the total density of charge carriers produced in the narrow-bandgap part of the *p*-type base. The decrease is caused by a reduction in the thickness of the narrow-bandgap part of the base. For the n^+–p junction under consideration, with virtually the whole space charge region occurring in the *p*-type base, the narrow-bandgap region thickness d_{ps} in the approximation of a fully depleted layer is [2]

$$d_{ps} = d_{ps}^0 - w_0\left(\sqrt{1 + \frac{|U|}{U_c}} - 1\right), \tag{3}$$

where d_{ps}^0 is the thickness of a quasilinear narrow-bandgap part of the *p*-type region in the equilibrium state, $w_0 \cong \sqrt{2\varepsilon\varepsilon_0 U_c/eN_a} = L_D\sqrt{2eU_c/kT}$ is the equilibrium space charge region thickness, L_D is the Debye screening length in the narrow-bandgap part of the *p*-type region, and $U_c = (kT/e)\ln(N_aN_d/n_{is}^2)$ is the contact potential difference of the *p*–*n* junction. According to relation (3), significant modulation of the thickness of the narrow-bandgap part of the *p*-type region is possible provided that d_{ps}^0 is comparable with w_0.

Small values of the reverse diffusion current in the *p*-type base of the structures under consideration make it necessary to take into account the current related to the charge carrier production in the space charge region, as well as the diffusion current in a strongly doped *n*-type layer, the thickness of which is assumed to be much greater than the hole diffusion length L_p. Using Eqs. (2) and (3), the total reverse current can be expressed as

$$\begin{aligned} j(U) &= e\Big[L_p g_{ns} + (d^0_{ps} + w_0)g_{ps} \\ &+ w_0(\bar{g} - g_{ps})\sqrt{1 + \frac{|U|}{U_c}}\Big]\Big[\exp\Big(-\frac{e|U|}{kT}\Big) - 1\Big], \end{aligned} \tag{4}$$

where $g_{ns} = n^2_{is}/(N_d\tau_p)$ is the reduced carrier production rate in the strongly doped *n*-type region with the donor concentration N_d and the hole lifetime τ_p $\bar{g}$ is the average value of the reduced carrier production rate in the space charge region [2, 3].

According to Eq. (4), a necessary condition for the appearance of NDR is

$$\bar{g} < g_{ps}, \tag{5}$$

the possibility of which strongly depends on the charge carrier production and recombination mechanisms both in the space charge region and in the base. In the case of the Shockley–Reed mechanism, whereby the recombination process takes place on simple doubly charged centers, the carrier production rate in the space charge region is [2, 3]

$$\bar{g}^{SR} = \frac{n^2_{is}}{\tau_{n0}p_1 + \tau_{p0}n_1 + 2\sqrt{\tau_{n0}\tau_{p0}}n_{is}\exp\Big(-\frac{e|U|}{2kT}\Big)}, \tag{6}$$

where $\tau_{n0} = (\alpha_n N_t)^{-1}$ and $\tau_{p0} = (\alpha_p N_t)^{-1}$; α_n and α_p are the rates of electron and hole trapping on the recombination centers, respectively; N_t is the density of recombination centers; and n_1 and p_1 are the densities of electrons and holes in the case when the Fermi level coincides with a recombination level.

Assuming that the Shockley–Reed mechanism also determines the lifetime of carriers in the base and taking into account deviation of the electron concentration from the equilibrium value, we obtain

$$\begin{aligned} &g^{SR}_{ps} \\ &= \frac{n_{is}[N_a + (n^2_{is}/N_a)\exp(-e|U|/kT)]}{\tau_{n0}(N_a + p_1) + \tau_{p0}[(n^2_{is}/N_a)\exp(-e|U|/kT) + n_1]}. \end{aligned} \tag{7}$$

For $|U| \gg kT/e$, Eqs. (6) and (7) imply that $\bar{g} \geq g_{ps}$ (with the equality for $N_a \ll p_1$), which indicates that NDR does not appear in the case of carrier recombination on simple doubly charged centers.

Now let us consider the case when a considerable role in the carrier production and recombination is played by the Auger processes. The average rate $\bar{g}^A$ of carrier production by the Auger mechanism in the space charge region can be expressed through the average densities of nonequilibrium electrons ($\bar{n}$) and holes ($\bar{p}$) [4, 5]:

$$\bar{g}^A = \frac{1}{2}\Big[\frac{\bar{p}}{\tau^{hh}_{Ai}} + \frac{\bar{n}}{\tau^{ee}_{Ai}}\Big] \approx \frac{n_{is}}{2}\exp\Big(-\frac{e|U|}{2kT}\Big)\Big[\frac{1}{\tau^{hh}_{Ai}} + \frac{1}{\tau^{ee}_{Ai}}\Big], \tag{8}$$

where τ^{hh}_{Ai} and τ^{ee}_{Ai} are the carrier lifetimes in the intrinsic semiconductor related to the *h*–*h* and *e*–*e* processes. According to (8), the rate of the Auger recombination process in the space charge region exponentially decreases with increasing reverse bias voltage, rather than tends to saturate (as in the case of the Shockley–Reed mechanism). At the same time, the Auger recombination rate in the narrow-bandgap part of the *p*-type base is

$$\begin{aligned} \bar{g}^A_B &= \frac{1}{2}\Big[\frac{N_a}{\tau^{hh}_{Ai}} + \frac{n^2_{is}}{\tau^{ee}_{Ai}N_a}\exp\Big(-\frac{e|U|}{kT}\Big)\Big] \\ &\approx \frac{1}{2}\frac{N_a}{\tau^{hh}_{Ai}} \quad (\text{at } |U| \gg kT/e). \end{aligned} \tag{9}$$

Taking into account Eqs. (6)–(9), the condition (5) necessary for the appearance of NDR reduces (for $|U| \gg kT/e$) to the following inequality:

$$\frac{n^2_{is}}{\tau_{n0}p_1 + \tau_{p0}n_1} < \frac{N_a}{2\tau^{hh}_{Ai}} + \frac{n^2_{is}}{\tau_{n0}(N_a + p_1) + \tau_{p0}n_1}. \tag{10}$$

Under the assumption of $\tau_{n0} = \tau_{p0}$ and $n_1 = p_1 = n_{is}$, this simplifies to

$$\tau_{n0} > \tau^{hh}_{Ai}\frac{n_{is}(N_a - n_{is})}{N_a(N_a + n_{is})}. \tag{11}$$

Since the lifetime of nonequilibrium carriers τ_{Ap} determined by the Auger recombination process in the *p*-type base for $N_a \gg n_{is}$ is $2\tau^{hh}_{Ai}n^2_{is}/N^2_a$ [5], relation (11) implies that, for $\tau_{n0} \gg \tau_{Ap}$, the NDR will appear provided that the Auger recombination dominates over the Shockley–Reed mechanism. This situation typically takes place in narrow-bandgap semiconductors, such as $Cd_xHg_{x-1}Te$ [6]. For the numerical estimate, consider $Cd_xHg_{x-1}Te$ with $x = 0.21$ and $N_a = 10^{17}$ cm^{-3} at $T = 77$ K, for which $n_{is} \approx 2 \times 10^{14}$ cm^{-3} and $\tau^{hh}_{Ai} \approx 1.2 \times 10^{-3}$ s [6, 7]. According to (11), the NDR in the *p*–*n* structures based on this material will appear provided that the Shockley–Reed lifetime τ_{n0} exceeds 2.4×10^{-6} s, which is usually the case in practice.

Thus, the most favorable materials for the realization of NDR, according to the proposed mechanism, are narrow-bandgap semiconductors in which the carrier lifetime is determined by the Auger recombination process.

REFERENCES

1. B. S. Sokolovskiĭ, Pis'ma Zh. Tekh. Fiz. **26** (7), 51 (2000) [Tech. Phys. Lett. **26**, 292 (2000)].
2. S. Sze, *Physics of Semiconductor Devices* (Wiley, New York, 1981; Mir, Moscow, 1984), Vol. 1.
3. S. V. Bulyarskiĭ, N. S. Grushko, A. I. Somov, and A. V. Lakalin, Fiz. Tekh. Poluprovodn. (St. Petersburg) **31** (9), 1146 (1997) [Semiconductors **31**, 983 (1997)].
4. J. S. Blakemore, *Semiconductor Statistics* (Pergamon, Oxford, 1962; Mir, Moscow, 1964).
5. A. Rogalski and R. Ciupa, J. Appl. Phys. **77** (7), 3505 (1995).
6. N. S. Baryshev, B. L. Gel'mont, and M. I. Imbragimova, Fiz. Tekh. Poluprovodn. (Leningrad) **24** (2), 209 (1990) [Sov. Phys. Semicond. **24**, 127 (1990)].
7. *Physics of II–VI Compounds*, Ed. by A. N. Georgobiani and M. K. Sheĭkman (Nauka, Moscow, 1986).

Translated by P. Pozdeev

Technical Physics Letters, Vol. 28, No. 12, 2002, pp. 1030–1032. Translated from Pis'ma v Zhurnal Tekhnicheskoĭ Fiziki, Vol. 28, No. 24, 2002, pp. 25–29.
Original Russian Text Copyright © 2002 by M. A. Grado-Caffaro, M. Grado-Caffaro.

Effect of the Oxide Thickness on the Operation Speed of a Field-Effect Transistor in Terms of the Carrier Tunneling Rate

M. A. Grado-Caffaro and M. Grado-Caffaro
Sapienza S.L. (Scientific Consultants), C/Julio Palacios 11, 9-B, 28029 Madrid, Spain

Received February 11, 2002; in final form, April 15, 2002

Abstract—A parameter characterizing the dependence of the velocity of electron tunneling through an oxide layer on the layer thickness is introduced. This parameter can be used to study the operation speed of multichannel field-effect transistors with control and floating gates. Estimates of the proposed characteristic quantity for the most typical experimental situations are obtained. *© 2002 MAIK "Nauka/Interperiodica".*

Introduction. The use of metal–oxide-semiconductor field-effect transistors (MOSFETs) in memory elements of low-current microcontrollers provides for a number of significant advantages. Since the operation of these devices is based on the passage of a tunneling current through an oxide layer, the oxide thickness t_{ox} is an important parameter determining the performance of the transistor in various aspects. For example, Ku and Chao [1] considered a relation between this parameter and the useful product yield.

Here, we report on the results of investigating the MOSFET operation speed in terms of a special parameter characterizing the effect of the oxide layer thickness on the velocity v of electron tunneling through this oxide. It is established that this quantity, reflecting the sensitivity with respect to t_{ox}, is identical to a parameter (introduced in a mathematically analogous form) describing a dependence of the tunneling current density on the oxide thickness.

Theory. The expression for the tunneling current through an oxide layer is well known [1–5]. As applied to a multichannel MOSFET based on the Al/SiO$_2$/Si structure, the theory yields

$$j = \frac{e^3 m_0 E^2}{16\pi^2 \hbar m_n^* E_{\text{b}}} \exp\left[-\frac{4(2m_n^* E_{\text{b}}^3)^{1/2}}{3e\hbar E}\right], \qquad (1)$$

where e is the elementary charge, E is the electric field strength in the oxide layer, m_0 is the free electron mass, m_n^* is the effective mass of a tunneling electron, $\hbar = h/2\pi$ is Planck's constant, and E_{b} is the tunneling barrier height from the cathode side. Taking into account the relations $E = v_{\text{ox}} t_{\text{ox}}$ and $j = env$, where v is the effective electron velocity and n is their density in the barrier (see, e.g., [1, 3, 4]), Eq. (1) can be rewritten as

$$v \approx \frac{e^2 m_0 E_{\text{b}}^{-1} v_{\text{ox}}^2}{16\pi^2 \hbar m_n^* n t_{\text{ox}}^2} \exp\left[-\frac{4(2m_n^* E_{\text{b}}^3)^{1/2} t_{\text{ox}}}{3e\hbar v_{\text{ox}}}\right]. \qquad (2)$$

Formula (2) is applicable for the voltage drop across the oxide $v_{\text{ox}} > E_{\text{b}}/e$.

We introduce a parameter characterizing the relative change in the carrier velocity caused by the oxide thickness variation:

$$s \equiv \left|\frac{1}{v}\frac{dv}{dt_{\text{ox}}}\right|. \qquad (3)$$

This quantity can be used, for example, as a criterion when it is necessary to determine the interval of t_{ox} in which the carrier velocity v (and, hence, the MOSFET operation speed) is most sensitive with respect to the oxide layer thickness. By substituting formula (2) into (3) we obtain

$$s \approx \frac{2}{t_{\text{ox}}} + \frac{4(2m_n^* E_{\text{b}}^3)^{1/2}}{3e\hbar v_{\text{ox}}}, \qquad (4)$$

where $m_n^* \approx m_0$ and $E_{\text{b}} \approx 3.2$ eV. Note that the characteristic parameter s is defined as the absolute value of an expression acquiring only negative values.

In order to obtain a numerical estimate of s, let us consider the case of $v_{\text{ox}} = 4$ V corresponding to a real device situation. Indeed, for $v_{\text{ox}} = 4$ V and $t_{\text{ox}} \sim 100$ Å, the tunneling current is quite significant [1, 3, 4], while at $v_{\text{ox}} \approx 3.2$ V (which is close to the limit of applicability of Eq. (1)), this current is still negligibly small. The

1063-7850/02/2812-1030$22.00 © 2002 MAIK "Nauka/Interperiodica"

above value of E_b (3.2 eV) can be calculated proceeding from the known energy difference between the conduction band bottom of SiO_2 and the valence band top of Si, which is 4.3 eV at room temperature (see, e.g., [6–8]). Then, $E_b = E_{c(SiO_2)} - E_{c(Si)} = 4.3–1.1 = 3.2$ eV (Fig. 1). Thus, for $V_{ox} = 4$ V and $E_b = 3.2$ eV, we obtain

$$s \approx 0.98 + \frac{2}{t_{ox}}, \qquad (5)$$

where t_{ox} is expressed in Å and s, in Å^{-1}.

Discussion. Previously [7], we introduced a parameter $s_{\mu n} = |\mu_n^{-1}(d\mu_n/dt_{ox})|$ characterizing the dependence of the differential mobility of electrons $\mu_n = (en)^{-1}(dj/dE)$ on the SiO_2 layer thickness (for the mobility defined as $\mu_n = d\nu/dE$, this corresponds simply to $j = en\nu$). For $s_{\mu n}$, it is also possible to derive an expression of the type of (5) [7] (naturally, with a constant term different from that obtained above for s). The plots of $s_{\mu n}(t_{ox})$ and $s(t_{ox})$ exhibit similar shapes. This is an important circumstance, because the properties of relation (5) turn out to be the same as the behavior of $s_{\mu n}(t_{ox})$, the physical meaning and the possible application of which have been studied in detail [7].

In particular, formula (5) is useful for practical characterization of the operation speed of MOSFETs. The most interesting range of oxide thicknesses is $t_{ox} = 100$–400 Å [1, 3]. In this very interval, the useful product yield was studied with sufficiently large statistics [1].

There is another circumstance that is important for memory elements of microcontrollers operating at low voltages. It was suggested in [1] that a decrease in the transistor source voltage from 5 to 3 V leads to a corresponding drop in the charge pumping voltage, gate control voltage, and voltage across the tunneling layer. The resulting decrease in the current of electrons tunneling to the floating gate (formula (1)) may slow down the readout rate and lead to malfunction of the memory element [1, 3, 4]. An analysis of expression (4) shows that a decrease in V_{ox} leads to an increase in s for a constant t_{ox} value.

Figure 2 shows a curve corresponding to formula (5) in the aforementioned most important interval of the oxide thickness variation, including the region of $t_{ox} \approx 100$ Å [1, 3, 4]. Expression (5) offers a tool for studying the electron tunneling velocity ν as a function of the oxide thickness t_{ox} [7] representing the sum of a constant and a term inversely proportional to t_{ox}.

The characteristic parameter s can be determined in a somewhat different way, namely, as $s = |j^{-1}(dj/dt_{ox})|$. Taking into account that $j = en\nu$, this is equivalent to $s = |\nu^{-1}(d\nu/dt_{ox})|$, as introduced above. By determining s through the current derivative, it is possible to bypass certain difficulties related to a discrepancy between the electron velocity entering into the relation $j = en\nu$ and that obtained according to quantum-mechanical description with wave functions within the framework of the Fowler–Nordheim model (1). Note also that the electron density n (proportional to the probability density determined in terms of the wave functions) does not enter into the expression for s.

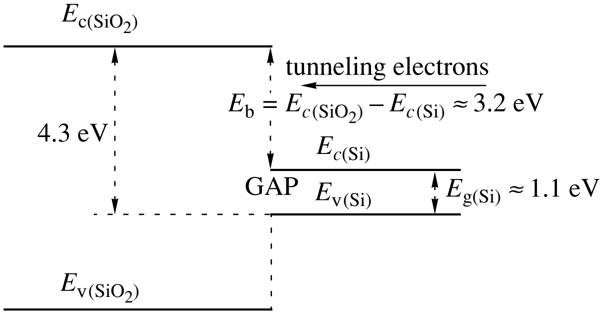

Fig. 1. An energy band diagram of the Si–SiO_2 system.

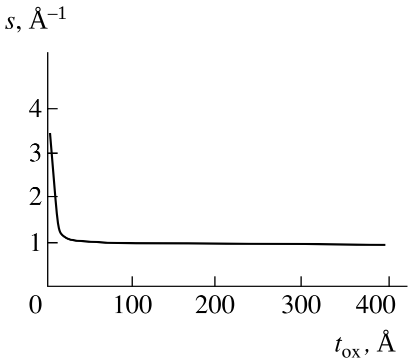

Fig. 2. A plot of the characteristic parameter s versus oxide thickness t_{ox} for $V_{ox} = 4$ V.

Conclusion. Thus, we have introduced a parameter s characterizing the sensitivity of the velocity of tunneling carriers with respect to the oxide layer thickness. According to the obtained expression (5), this parameter is $s \approx 1$ Å^{-1} at $t_{ox} \approx 100$ Å and is almost independent of the oxide thickness for $t_{ox} > 100$ Å. At $t_{ox} \ll 100$ Å, s significantly increases with decreasing oxide thickness (Fig. 2). This behavior is related to a strong dependence of the tunneling current density j on the field strength E. The analysis was performed for an effective electron mass in the oxide $m_n^* = m_0$, which agrees with $m_n^* = 0.84m_0$ reported in [8]. The theoretical part of this study is closely related to [9–12].

REFERENCES

1. J. W. Ku and S. C. Chao, Semicond. Int., May, 105 (1997).

2. S. Sze, *Physics of Semiconductor Devices* (Wiley, New York, 1981; Mir, Moscow, 1984).
3. I. Chen, S. Holland, and C. Hu, IEEE Trans. Electron Devices **ED-32**, 413 (1985).
4. M. A. Grado-Caffaro and M. Grado-Caffaro, Act. Pass. Electron. Comp. **20**, 165 (1998).
5. M. A. Grado-Caffaro and M. Grado-Caffaro, Act. Pass. Electron. Comp. **21**, 57 (1998).
6. B. E. Deal, E. N. Snow, and C. A. Mead, J. Phys. Chem. Solids **27**, 1873 (1966).
7. M. A. Grado-Caffaro and M. Grado-Caffaro, Eur. Phys. J.: Appl. Phys. **5**, 1 (1999).
8. L. F. Mao, J. L. Wei, Ch. H. Tan, and M. Zh. Xu, Solid State Commun. **114**, 383 (2000).
9. J. Tang and K. Hess, J. Appl. Phys. **54**, 5145 (1983).
10. P. Pavan, R. Bez, P. Olivo, and E. Zanoni, Proc. IEEE **85**, 1255 (1997).
11. J. Maserjian and N. Zamani, J. Appl. Phys. **53**, 559 (1982).
12. J. Maserjian, J. Vac. Sci. Technol. **11**, 996 (1974).

Translated by P. Pozdeev

Technical Physics Letters, Vol. 28, No. 12, 2002, pp. 1033–1035. Translated from Pis'ma v Zhurnal Tekhnicheskoĭ Fiziki, Vol. 28, No. 24, 2002, pp. 30–35.
Original Russian Text Copyright © 2002 by Zolotovskiĭ, Sementsov.

The Effect of a Linear Mode Coupling Dispersion on the Wave Packet Dynamics in an Optical Waveguide with Kerr Nonlinearity

I. O. Zolotovskiĭ and D. I. Sementsov
Ul'yanovsk State University, Ul'yanovsk, Russia

Received July 18, 2002

Abstract—The influence of a dispersion of the linear mode coupling coefficient of an optical waveguide (OWG) with Kerr nonlinearity on the dispersion parameters and dynamics of an optical pulse propagating in such a system is studied. In OWGs with a strong linear mode coupling, the presence of a dispersion of the mode coupling may lead to a significant decrease in the energy threshold for nonlinear self-compression of pulses as compared to the case of a single-mode OWG. © *2002 MAIK "Nauka/Interperiodica".*

1. In recent years, special attention has been drawn to the analysis of cases in which radiation transmitted through an optical waveguide (OWG) can be represented as a sum of two interacting waves. This situation is most typical of tunneling-coupled optical waveguides (TCOWGs), periodic structures, and some anisotropic and gyrotropic media [1]. The effective characteristics of dispersion in such systems usually depend on the mode coupling parameter [2].

However, the previous analyses did not take into account dispersion of the coupling coefficient proper and the possible influence of this factor on the dynamics of an optical pulse propagating in a system of distribution-coupled waves. The need for such an analysis is obvious because short pulses are characterized by a broad frequency spectra with extensive mode coupling between various components. This is especially important for TCOWGs for which the coupling coefficient strongly depends on the frequency. Strip TCOWGs based on GaAs crystals may prove of most interest in practical applications [3–5].

Below, we study the effect of a dispersion of the linear mode coupling coefficient on the dynamics of a two-mode wave packet in an TCOWG exhibiting a strong linear coupling of unidirectional waves and possessing a nonlinearity of the Kerr type.

2. The propagation of a two-mode wave packet, with allowance for the linear mode coupling dispersion, mode detuning, group velocity dispersion, and a waveguide medium nonlinearity of the Kerr type, is described by a system of equations for the time envelopes of two ($j = 1, 2$) interacting modes [6, 7]:

$$\frac{\partial A_j}{\partial z} + \frac{\xi_j}{v}\frac{\partial A_j}{\partial \tau} - i\frac{d_j}{2}\frac{\partial^2 A_j}{\partial \tau^2} + i(\gamma_c|A_j|^2 + \gamma_k|A_{3-j}|^2)A_j = -i\sigma A_{3-j}. \qquad (1)$$

Here, $\tau = t - z/u$ is the current time, $2u = (u_1 + u_2)$ is the group velocity of the wave packet, $u_j = (\partial\beta_j/\partial\omega)^{-1}_{\omega_0}$ is the group velocity and β_j is the propagation constant of the jth mode, ω_0 is the carrier frequency of the wave packet, $d_j = (\partial^2\beta_j/\partial\omega^2)_{\omega_0}$ are the group velocity dispersion parameters, $v^{-1} = (u_1 - u_2)/2u^2$ is the detuning of the group velocities of modes, γ_c and γ_k are the parameters of nonlinearity determining the phase self- and cross-modulation of the interacting waves, and $\xi_j = (-1)^j$. The dispersion of the mode coupling is taken into account by replacing the parameter σ (determined by overlap of the waveguide mode profiles) with an operator,

$$\hat{\sigma}_j = \sigma\left(1 - i\xi_j\mu\frac{\partial}{\partial\tau}\right), \qquad (2)$$

where μ is a parameter described by an approximate formula [8],

$$\mu \cong \frac{2}{\omega} + \frac{1}{\sigma}\frac{\partial\sigma}{\partial\omega}. \qquad (3)$$

In writing expression (2), we took into account (unlike in [8]) that the operators $\hat{\sigma}_{1,2}$ of the coupled modes must be complex-conjugated quantities.

The system of equations (1) has to be solved together with a set of initial conditions for the time envelopes A_j determined by the TCOWG excitation conditions. The general form of the initial conditions is given by the relation $A_2(\tau, 0) = \psi A_1(\tau, 0)$, where ψ is a parameter determining the TCOWG excitation type. For $\psi = \pm1$, the two-mode waveguide excitation is symmetric or antisymmetric, while $\psi^{-1} = 0$ implies a single-mode excitation. A solution to Eqs. (1) can be obtained in a strong mode coupling approximation, whereby the

1063-7850/02/2812-1033$22.00 © 2002 MAIK "Nauka/Interperiodica"

mode interaction length $L_\sigma = |\sigma|^{-1}$ is much smaller than the dispersion length $L_d = \tau_0^2/|d|$, the nonlinearity length $L_n = (\gamma I_0)^{-1}$, and the intermode recession length $L_v = v\tau_0$ (here, τ_0 and $I_0 = |A_{10}|^2 + |A_{20}|^2$ are the duration and intensity of a pulse entering the waveguide, respectively; $2d = d_1 + d_2$ and $2\gamma = \gamma_c + \gamma_k$). For TCOWGs based on GaAs crystals, the linear coupling and nonlinearity parameters can be as large as $|\sigma| \cong 10^3$ m^{-1} and $\gamma \cong 10^{-9}$ m/W [3]. This indicates that the given approximation is valid for an initial radiation intensity of $I_0 \le 10^{12}$ W/m^2 (at an OWG cross section area of $S \cong 10^{-7}$ cm^2). Since the material dispersion parameter falls within $|d_j| \cong 10^{-26}$–10^{-27} s^2/m, the given approximation is valid for a pulse duration of $\tau_0 \cong 10^{-14}$ s. Therefore, there is virtually no limitations with respect to the pulse duration.

In the adopted approximation, the time envelope of the corresponding mode can be represented as a sum of two partial pulses:

$$\begin{aligned} A_j &= (-1)^{j+1} a_1(\tau, z)\exp(i|\sigma|z) \\ &\quad + a_2(\tau, z)\exp(-i|\sigma|z), \end{aligned} \tag{4}$$

where a_f are partial pulse amplitudes that slowly vary with the coordinate z. The partial amplitudes obey the equations

$$\begin{gathered} \frac{\partial a_f}{\partial z} - \frac{iD_f}{2}\frac{\partial^2 a_f}{\partial \tau^2} + 2\gamma(|a_f|^2 + s|a_{3-f}|^2)a_f = 0, \\ f = 1, 2, \end{gathered} \tag{5}$$

where $s = \gamma_c/\gamma_k$ and D_f is the effective dispersion given by the formula

$$D_f = d + (-1)^f(1 + (v\sigma\mu)^2)/v^2|\sigma|. \tag{6}$$

This quantity, determining the dispersion of the waveguide medium with respect to the partial pulses, includes both material and intermode dispersion components. Taking into account expressions (4), we obtain the initial conditions for the partial pulse amplitudes,

$$a_f(\tau; 0) = \frac{1}{2}[1 + (-1)^f\psi]A_{10}(\tau, 0), \tag{7}$$

which have to be used in solving Eqs. (5).

3. It follows from Eqs. (5) that, for both symmetric and antisymmetric two-mode excitation ($A_{20} = \pm A_{10}$), the amplitude of one of the partial pulses is zero ($a_1 = 0$ for the symmetric and $a_2 = 0$ for the antisymmetric excitation). In this case, Eqs. (5) degenerate into a common nonlinear Schrödinger equation [7]:

$$\frac{\partial a_f}{\partial z} - \frac{iD_f}{2}\frac{\partial^2 a_f}{\partial \tau^2} + 2i\gamma|a_f|^2 a_f = 0, \tag{8}$$

where subscript $f = 1$ and 2 for the antisymmetric and symmetric excitation, respectively. Equation (8) describes the dynamics of a pulse propagating in a cubically nonlinear medium with nonlinearity parameter γ and effective dispersion D_f.

A characteristic feature of the wave packet propagation in this case is self-action leading to both expansion and compression of the packet. The self-action also leads to the formation of stable wave packets (Schrödinger solitons), the appearance of which is related to a balance between the medium nonlinearity and dispersion [6, 7]. The self-compression takes place in the case of an anomalous effective dispersion ($D_f < 0$) under the condition that $L_n < L_D = \tau_0^2/|D_f|$. If dispersive expansion of the pulse is fully compensated by the self-compression (which takes place for $L_n = L_D$), we observe the formation of a solitonlike pulse with a duration of τ_p and an energy density of $W_s = |D_f|/\gamma\tau_p$. Note that the wave packet propagating in the waveguide is not a soliton in the strict sense because the system of equations (1) cannot be integrated in the general case. This wave packet is essentially a pulse with a periodically varying duration (oscillating about τ_p), rather than a soliton as such.

It is important to note that the self-compressed wave packet can travel, retaining its average duration, over distances significantly exceeding the mode interaction length (for the TCOWG studied, this length is $L_\sigma \cong 1$ mm). If the energy density $W_0 = I_0\tau_0$ introduced into the waveguide is smaller than W_s, the pulse exhibits expansion, while for $W_0 > W_s$, the pulse is self-compressed. In the latter case, which is of practical interest in applications, the degree of self-compression can be estimated as

$$\tau_0/\tau_p \cong 4(\gamma a_{f0}^2\tau_0^2/|D_f|)^{1/2} \cong 8W_0/W_s. \tag{9}$$

4. For an arbitrary initial excitation of the system studied, an expression for the pulse duration can be obtained with the aid of the variation method used in [9–11] to analyze like systems of equations of type analogous to Eqs. (5). Not dwelling on the details of this method, we present the final expression for the duration of a solitonlike pulse: $\tau_s \cong D_{ef}/\gamma_{ef}I_0\tau_0$, where D_{ef} and γ_{ef} are the effective dispersion and nonlinearity parameters given by the formulas

$$\begin{gathered} D_{ef} = d + \frac{2\psi}{(1+\psi^2)v^2|\sigma|}(1 + (v\sigma\mu)^2), \\ \gamma_{ef} = \gamma\left(1 + \frac{1}{2}\frac{\gamma_c - \gamma_k}{\gamma_c + \gamma_k}\left(\frac{\psi^2 - 1}{\psi^2 + 1}\right)^2\right). \end{gathered} \tag{10}$$

In this case, a nonlinear self-compression regime takes place under the condition that $D_{ef}(\gamma_{ef}I_0 + 2D_{ef}/\tau_0^2) < 0$.

Taking into account that $D_{ef} < 0$, the energy threshold for nonlinear self-compression is $I_0 = 2D_{ef}/\gamma_{ef}\tau_0^2$. A numerical estimate for μ can be obtained from the relation $|\mu| \cong 2\pi/\omega_0$, where ω_0 is the central frequency of the pulse entering into the TCOWG [8]. Since the working frequency range is $\omega_0 \cong (1–4) \times 10^{15}$ s^{-1} and $\sigma = 10^2$–10^4 m^{-1}, the contribution to the dispersion parameter related to the dispersion of the mode coupling coefficient falls within $\mu^2|\sigma| \cong (10^{-28}–10^{-25})2\psi/(1 + \psi^2)$ s^2/m.

These estimates are indicative of a rather strong influence of dispersion of the coupling coefficient on the effective dispersion of wave packets in the TCOWG. Therefore, this factor plays an important role in determining the pulse dynamics in such OWGs. In particular, by selecting the central frequency ω_0 and the waveguide excitation conditions, it is possible to decrease the effective dispersion to a level of $|D_{ef}| \cong 10^{-29}–10^{-28}$ s^2/m. This, in turn, allows the initial pulse intensity necessary for the self-compression to be decreased to $I_0 \cong 10^5$ W/m^2 (which is one to three orders of magnitude lower as compared to the threshold intensity typical of single-mode quartz waveguides [6]).

The properties of TCOWGs described above show good prospects for the creation of miniature optical compressors. Indeed, upon introducing a pulse with a duration of $\tau_0 = 10^{-13}$ s and an intensity of $I_0 = 10^{11}$ W/m^2 into such a waveguide with the parameters $\gamma_{ef} \cong 10^{-9}$ m/W and $D_{ef} \cong -10^{-26}$ s^2/m, we obtain a compressed pulse of extremely short width $\tau_s \cong 10^{-15}$ s after a distance as small as $l_s \cong \sqrt{\tau_0^2/|D_{ef}|\gamma_{ef}I_0} \cong 0.1$ m.

Even more impressive results can be expected from TCOWGs based on InSb crystals, as they possess a nonlinearity parameter four times greater than that of GaAs. This factor, together with effective control of the OWG dispersion, allow the energy threshold for nonlinear self-compression of pulses to be reduced to an extremely low level, $I_0 \cong 10$ W/m^2.

REFERENCES

1. A. A. Maĭer, Usp. Fiz. Nauk **165** (9), 1037 (1995) [Phys. Usp. **38**, 991 (1995)].
2. I. O. Zolotovskiĭ and D. I. Sementsov, Opt. Spektrosk. **86** (5), 824 (1999) [Opt. Spectrosc. **86**, 737 (1999)].
3. A. A. Maĭer, Kvantovaya Élektron. (Moscow) **11** (2), 157 (1984).
4. Y. J. Chen and G. M. Carter, Appl. Phys. Lett. **41**, 307 (1982).
5. D. B. Mortimor and J. M. Arkwright, Appl. Opt. **29**, 1814 (1990).
6. G. Agrawal, *Nonlinear Fiber Optics* (Academic, San Diego, 1995; Mir, Moscow, 1996).
7. S. A. Akhmanov, V. A. Vysloukh, and A. S. Chirkin, *The Optics of Femtosecond Pulses* (Nauka, Moscow, 1988).
8. A. A. Maĭer and S. G. Karataev, Kvantovaya Élektron. (Moscow) **23** (1), 43 (1996).
9. E. M. Dianov, Z. S. Nikonova, A. M. Prokhorov, and V. N. Serkin, Pis’ma Zh. Tekh. Fiz. **12** (8), 756 (1986) [Sov. Tech. Phys. Lett. **12**, 311 (1986)].
10. D. Anderson, Phys. Rev. A **27**, 3135 (1983).
11. A. I. Maĭmistov, Kvantovaya Élektron. (Moscow) **18** (6), 758 (1991); **21** (4), 358 (1994).

Translated by P. Pozdeev

Technical Physics Letters, Vol. 28, No. 12, 2002, pp. 1036–1039. Translated from Pis'ma v Zhurnal Tekhnicheskoĭ Fiziki, Vol. 28, No. 24, 2002, pp. 36–42.
Original Russian Text Copyright © 2002 by Kudryavtsev, Tsendin.

Townsend Discharge Instability on the Right-Hand Branch of the Paschen Curve

A. A. Kudryavtsev[a] and L. D. Tsendin[b]
[a] *St. Petersburg State University, St. Petersburg, Russia*
e-mail: akud@ak2138.spb.edu
[b] *St. Petersburg State Technical University, St. Petersburg, Russia*
e-mail: tsendin@phtf.stu.neva.ru

Received July 16, 2002

Abstract—The stability of the Townsend discharge with respect to transverse perturbations on the right-hand branch of the Paschen curve is studied. An expression for the instability increment is obtained which allows the characteristic pinching time of a subnormal discharge under various conditions to be determined. *© 2002 MAIK “Nauka/Interperiodica”.*

The Townsend (spatially homogeneous) discharge at small overvoltages can be realized for large values of the parameter pL, where p is the pressure and L is the interelectrode distance [1]. This allows a homogeneous glow discharge to be obtained at pressures up to atmospheric, which is of importance for various applications. The most promising field of such applications is related to the dc barrier discharge (DBD) between electrodes one or both of which are coated with insulators. At present, extensive research is being aimed at establishing the optimum conditions for obtaining homogeneous DBDs in various gases and various discharge gap geometries (see, e.g., [2–4]). From this standpoint, a most unfavorable factor is the development of instabilities leading to a loss of discharge homogeneity in the transverse direction (across the current).

The passage of the discharge current involves the formation of a space charge and the distortion of a potential distribution. As a result, the current–voltage characteristic of such a subnormal discharge on the right-hand branch of the Paschen curve decays, because the discharge operation requires a lower voltage as compared to that necessary for the discharge initiation (breakdown) [1,10]. Under these conditions, transverse instabilities can develop even at very low discharge current densities (see, e.g., [5–8]). Experiments show that, depending on the discharge conditions, the development of transverse instabilities can lead both to a spatially inhomogeneous stationary discharge and to an oscillatory regime accompanied by relaxation or almost sinusoidal oscillations of the whole discharge [5, 7, 9].

We obtained an expression for the instability increment of a subnormal Townsend discharge with respect to transverse perturbations, which allows the characteristic pinching time of this discharge to be estimated under various conditions.

For the ion-induced electron emission mechanism, the time of development of the transverse instabilities is determined by the drift of ions from anode to cathode, $\tau_i = L/V_i$ [11], while the corresponding electron flight time $L/V_e \ll \tau_i$ can be considered negligibly small. Then, the ion current density on the cathode at a time instant t is

$$j_i(z=0,t) = \int_0^L \alpha(z) j_e(z, t - z/V_i)dz.$$

Using the standard Townsend condition on the cathode, we obtain an equation for this quantity,

$$j_i(z=0,t) = \int_0^L \alpha(z)\gamma j_i(z=0, t-z/V_i) \times \exp\left(\int_0^z \alpha(E(z'))dz'\right)dz, \qquad (1)$$

where α and γ are the first and second Townsend coefficients. For $\gamma \ll 1$, we have $\alpha L \gg 1$ and, hence, the majority of ions form at the anode. Therefore, the term $j_i(z=0, t-\tau_i)$ can be factored out of integral (1). After some transformations, we obtain the following condition for a stationary discharge:

$$j_i(z=0, t+\tau_i) = \gamma j_i(z=0,t) \times \left[\exp\left(\int_0^L \alpha(E)dz\right) - 1\right]. \qquad (2)$$

In order to take into account the space charge, which appears even at a small discharge current, let us consider a small field perturbation δE induced by this factor. This perturbation will primarily influence the ionization coefficient $\alpha(E/p)$: on the right-hand branch of the Paschen curve, this coefficient sharply depends on the field strength and can be conveniently represented as

$$\alpha(E) = \alpha_0 + \alpha'(E_0)\delta E + \alpha''(E_0)(\delta E)^2/2, \tag{3}$$

where $E_0 = U_{br}/L$ is the breakdown field strength and U_{br} is the breakdown (discharge initiation) voltage.

Under the conditions studied, the ion density $n_i = j_i/(eV_i) = j_i/(eb_iE)$ can be considered homogeneous (everywhere except for in a small region ~$1/\alpha$ near the anode) and significantly greater than the electron density (the latter can be ignored). Then, the Poisson equation takes the form $d(\delta E)/dz = 4\pi e n_i$ and leads to the following linear field profile:

$$\begin{aligned}\delta E(z) &= \delta U/L - 4\pi e n_i(z - L/2)\\ &= \delta U/L - 4\pi e j_i(z - L/2)(b_iE_0).\end{aligned} \tag{4}$$

Using Eq. (4) and taking into account condition (2), we obtain an equation determining the unperturbed value of $\delta E_0 = \delta U/L$:

$$\begin{aligned}\int_0^L \alpha(E)dz &= \alpha_0 L + \alpha'\delta U + 2\alpha'' L(\pi e n_i L)^2/3\\ &= \ln(1 + 1/\gamma).\end{aligned} \tag{5}$$

Since the condition of self-sustained discharge upon breakdown is $\alpha_0 L = \ln(1 + 1/\gamma)$, we can use Eq. (4) to determine a decrease in the working discharge voltage as compared to the breakdown value, that is, to describe the current–voltage characteristic of the Townsend discharge with allowance for a small field perturbation [12]:

$$\delta U = 2\alpha'' L(\pi e n_i L)^2/3\alpha'. \tag{6}$$

For the relation $j = eb_iEn_i$, this expression yields a parabolic current–voltage characteristic originally presented in [13]:

$$\delta U = U_{br} - U = 2\pi^2\alpha'' j^2 L^3/3\alpha'. \tag{7}$$

Using the usual approximation

$$\alpha = pA\exp(-Bp/E), \tag{8}$$

we obtain $\alpha' = \alpha Bp/E^2$ and $\alpha'' = \alpha'(Bp/E - 2)/E$. For the right-hand branch of the Paschen curve ($Bp/E > 2$), Eqs. (6) and (7) yield a descending current–voltage characteristic known to be unstable with respect to fluctuations.

Let us study condition (2) with respect to two-dimensional perturbations of the type

$$\begin{aligned}j_i(t, y) &= j_i^0 + \tilde{j}_i(z)\exp(\Omega t + iky),\\ \delta E &= \delta E_0 + \delta\tilde{E}(z)\exp(\Omega t + iky),\end{aligned} \tag{9}$$

where δE_0 is determined according to Eq. (4) and $n_i = j_i^0/eb_iE_0$. Taking into account that the voltage variation δU is independent of the transverse coordinate and using Eq. (4), we obtain

$$\delta\tilde{E}(z) = 4\pi e\tilde{j}_i(z)(L/2 - z)/eb_iE_0. \tag{10}$$

The number of multiplications can be described as

$$\begin{aligned}\int_0^L \alpha(E)dz &= \alpha_0 L + \alpha'\delta U\\ &+ \alpha''\int_0^L (\delta E_0^2(z)/2 + \delta E_0(z)\delta\tilde{E}(z))dz.\end{aligned} \tag{11}$$

For small δE_0, we can use the expansion

$$\exp\left(\alpha''\int_0^L \delta E_0\delta\tilde{E}dz\right) \approx 1 + \alpha''\int_0^L \delta E_0\delta\tilde{E}dz. \tag{12}$$

The integral in the right-hand part of this expansion can be calculated, using Eqs. (4) and (10), as

$$\int_0^L \delta E_0\delta\tilde{E}dz = \frac{L^3}{12}\frac{(4\pi)^2}{(b_iE_0)^2}j_i^0\tilde{j}_i. \tag{13}$$

Substituting $\tilde{j}_i(t + \tau_i) - \tilde{j}_i(t) \approx \tau_i(d\tilde{j}_i/dt)$, we eventually obtain the following relation from Eq. (1):

$$\frac{d\tilde{j}_i}{dt} = \alpha''\frac{L^3}{12}\frac{(4\pi e j_i^0)^2}{\tau_i(b_iE_0)^2}\tilde{j} = \Omega_i\tilde{j}_i. \tag{14}$$

According to Eq. (14), the characteristic time of instability development

$$\tau_{sn} = 1/\Omega_i = \frac{12}{(4\pi e n_i)^2\alpha'' L^3}\tau_i = \frac{3b_iE_0}{4\alpha''(\pi L j_i^0)^2} \tag{15}$$

is determined by the ion drift time and increases with decreasing interelectrode distance L. Formula (15) can be rewritten using conventional variables pL, j/p^2, and α/p. Using the approximation (8), the relation $\alpha'' =$

$\alpha(Bp)^2/E^4$, and the self-sustained discharge condition in the form of $\alpha L \approx \ln(1 + 1/\gamma)$, we obtain a relationship between the discharge parameters in the form of a scaling relation:

$$\tau_{sn} = \frac{3(b_i p)}{4\pi^2}\frac{(E_0/pB)^2}{(\alpha/p)}\frac{(E_0/p)^3}{(j_i^0/p^2)^2}\frac{1}{(pL)^2 p}$$
$$\approx \frac{3}{4\pi^2}\frac{(U_{br}/pBL)^2}{\ln(1/\gamma + 1)}\frac{(U_{br}/pL)^3}{(j_i^0/p^2)^2}\frac{(b_i p)}{(pL)p}. \quad (16)$$

Thus, even a small inhomogeneity of the field related to the space charge leads to a decaying current–voltage characteristic (Eq. (7)) and, hence, to instability of the Townsend discharge. The farther the working value of pL on the right-hand branch of the Paschen curve, the smaller the field distortion by the space charge (and the smaller the discharge current) sufficient for the onset of instability development. The detailed scenario of instability development depends on the external circuit characteristics, discharge gap geometry, and the cathode material. The instability development leads to pinching of the discharge and the establishment of a normal current density at which the discharge occupies only part of the cathode surface [10]. Eventually, a discharge with an average current density of $j < j_n$ separates into columns, in which the current density is close to j_n (which can be several time greater than j) and current-free regions. Besides pinching, a discharge can also feature the development of instabilities leading to oscillations of the total discharge current and voltage [5, 7]. It was shown in [5] that this takes place provided at least one of the following conditions holds: $R < R_d$, $\Omega_i > 1/(RC)$, where R and C are the resistance and capacitance of the discharge–external circuit system and R_d is the differential resistance of the discharge.

Development of the aforementioned instability is hindered by the electron avalanche spreading in the transverse direction. Since this process is determined by the free diffusion of electrons, it might seem that the corresponding large damping factor could suppress the instability development. However, it was demonstrated in [7] that the effective damping is small. During a short time of about $L/(b_eE)$, the avalanche propagating from cathode to anode spreads over a distance of $\Delta y \approx \sqrt{(T_eL)/(eE)}$. This process is repeated after a relatively long period of time $\tau_i = L/V_i$ required for ions generated by the avalanche (mostly at the anode) to drift back to the cathode. In other words, although the multiplication period is $\tau_i + L/(b_eE)$, the diffusion (smearing) takes place only within a small ("electron") part of this process. Since random walk corresponds to adding of the squared displacements, the resulting smearing for the time period $t \gg \tau_i$ is $y^2 = (\Delta y)^2 t/\tau_i = b_iT_et$. This corresponds to diffusion with an effective coefficient $D_a = b_iT_e$ on the order of the ambipolar diffusion coefficient, although plasma is still not formed in the bulk. The corresponding decrement is D_ak^2. Since the increment Ω_i in Eqs. (14)–(16) is independent of the wavenumber, the most dangerous are perturbations with minimum k values determined by the cathode size R. These perturbations correspond to a decrement on the order of D_a/R^2, which is usually smaller than the increment Ω_i of the instability development. This result reflects the well-known fact (see, e.g. [11]) that a homogeneous development of the Townsend discharge on the right-hand branch of the Paschen curve can be realized only provided the breakdown voltage is applied to the gap for a period of time shorter than τ_{sn} given by formulas (15) and (16). This is usually achieved with the aid of a pulsed (sinusoidal) voltage source and electrodes of a special design made of selected materials. It is also believed (see, e.g. [2–4]) that insulator-coated electrodes charged by incident electrons favor improved discharge operation characteristics and facilitate the formation of self-sustained homogeneous high-pressure discharge.

Thus, the duration of operation of a homogeneous Townsend discharge in a subnormal regime is limited by the development of transverse instabilities leading to the formation of a cathode layer and a normal current density. The appearance of the cathode layer formally corresponds to a transition to the point of minimum on the Paschen curve and to "switching off" the exponential dependence of $\alpha(E/p)$ [10]. Under these conditions, nonlocal ionization in the weak field region becomes significant and the Townsend ionization coefficient $\alpha(E/p)$ determined by the local field strength is no longer applicable.

As demonstrated in [14], a necessary condition for stable streamer propagation is that the maximum field strength at the front be on the order of the value at the bending point of the $\alpha(E/p)$ function, which implies that the field at the streamer head must also correspond to the condition of a transition to nonlocal ionization. This circumstance gives us ground to believe that the instability considered above is directly related to the conditions of a transition from avalanche to streamer.

Acknowledgments. One of the authors (L.D.Ts.) gratefully acknowledges the support of the Russian Foundation for Basic Research (project no. 01-02-16874) and NATO (grant SfR 974354).

REFERENCES

1. Yu. P. Raizer, *Gas Discharge Physics* (Nauka, Moscow, 1987; Springer-Verlag, Berlin, 1991).
2. T. Yokoyama, M. Kagoma, S. Kanazawa, *et al.*, J. Phys. D **23**, 374 (1990).
3. F. Massines, A. Rabehi, P. Decomps, *et al.*, J. Appl. Phys. **83**, 2950 (1998).

4. L. Margolini, K. Orlov, U. Kortshagen, *et al.*, Appl. Phys. Lett. **80**, 1722 (2002).
5. V. N. Melekhin and N. Yu. Naumov, Zh. Tekh. Fiz. **54** (8), 1521 (1984) [Sov. Phys. Tech. Phys. **29**, 888 (1984)].
6. V. A. Shveĭgert, Zh. Tekh. Fiz. **63** (5), 29 (1993) [Tech. Phys. **38**, 384 (1993)].
7. I. D. Kaganovich, M. A. Fedotov, and L. D. Tsendin, Zh. Tekh. Fiz. **64** (3), 22 (1994) [Tech. Phys. **39**, 241 (1994)].
8. V. I. Kolobov and A. Fiala, Phys. Rev. E **50**, 3018 (1994).
9. Z. Lj. Petrovich and A. V. Phelps, Phys. Rev. E **47**, 2806 (1993).
10. L. D. Tsendin, in *Encyclopedia of Low-Temperature Plasma*, Ed. by V. E. Fortov (Nauka, Moscow, 2000), Vol. II, pp. 16–18.
11. E. P. Velikhov, A. S. Kovalev, and A. T. Rakhimov, *Physical Phenomena in Gas-Discharge Plasma* (Nauka, Moscow, 1987).
12. B. M. Smirnov, *Physics of Weakly Ionized Gas in Problems with Solutions* (Nauka, Moscow, 1985).
13. A. von Engel, *Ionized Gases* (Clarendon, Oxford, 1955).
14. M. I. D’yakonov and V. Yu. Kachorovskiĭ, Zh. Éksp. Teor. Fiz. **94** (5), 321 (1988) [Sov. Phys. JETP **67**, 1049 (1988)].

Translated by P. Pozdeev

Technical Physics Letters, Vol. 28, No. 12, 2002, pp. 1040–1042. Translated from Pis'ma v Zhurnal Tekhnicheskoĭ Fiziki, Vol. 28, No. 24, 2002, pp. 43–47.
Original Russian Text Copyright © 2002 by Primak, Sotskaya.

Restoration of the Parameters of an Adsorption Layer on the Surface of a Channel Optical Waveguide

I. U. Primak and L. I. Sotskaya
Institute of Applied Optics, National Academy of Sciences of Belarus, Mogilev, Belarus
e-mail: ipo@physics.belpak.mogilev.by

Received May 31, 2002

Abstract—The problem of restoration of the thickness, dielectric permittivity, and surface density of an adsorption layer on the surface of a channel optical waveguide is analytically solved. All properties of the waveguide in the solution are described by a single coefficient, which can be readily determined in experiment. *© 2002 MAIK “Nauka/Interperiodica”.*

Measurement of the concentrations of impurities in gaseous or liquid media with the aid of integral optical sensors of the interference type and adjustment of the working points of directional couplers, modulators, and other spectral elements frequently encounter the problem of restoring the parameters (dielectric permittivity ε_f, thickness d_f, and surface density Γ_f [1]) of a submicron adsorption layer (adlayer) existing on the surface of a channeled optical waveguide (OWG) [2–5]. However, this problem has not yet been solved on a satisfactory level. At the same time, the results of analogous investigations performed for planar waveguides [1, 5–8] suggest that the data on ε_f, d_f, and Γ_f for the aforementioned channel waveguides can be restored from experimentally measured dependences of the type $\beta = \beta(d_f)$, where β is a waveguide mode propagation constant.

Here, we report on an investigation of the asymptotic behavior of the mode characteristics of a waveguide structure comprising a channel optical waveguide (OWG) possessing an arbitrary permittivity profile and an adsorption layer on the waveguide surface. It will be demonstrated that the ε_f, d_f, and Γ_f values can be restored via experimentally measurable increments $\Delta\beta = \beta(d_f) - \beta(0)$ for quasi-TE and quasi-TM modes. All properties of the waveguide in the solution are described by a single coefficient, which can be readily determined in preliminary experiments.

Consider the structure schematically depicted in the figure. The dielectric permittivity of this structure can be represented as

$$\begin{gathered}\varepsilon = \varepsilon_s + \Delta\varepsilon f(\xi, \eta) \quad (y < 0), \\ \varepsilon = \varepsilon_f \quad (0 < y < d_f), \quad \varepsilon = \varepsilon_c \quad (y > d_f),\end{gathered} \tag{1}$$

where $f(\xi, \eta)$ is a function describing the channel OWG profile, $\xi = xw^{-1}$, $\eta = yw^{-1}$, w is a scaling factor characterizing the transverse waveguide dimensions, and ε_s, ε_c, ε_f, and $\Delta\varepsilon$ are real constants. The channel OWGs usually belong to weakly directing ones [9], which implies that

$$\varepsilon_s > \varepsilon_c, \quad \left|\Delta\varepsilon\varepsilon_s^{-1}\right| \ll 1, \quad \left|\Delta\varepsilon(\varepsilon_s - \varepsilon_c)^{-1}\right| \ll 1. \tag{2}$$

Using conditions (2), it is possible to construct solutions for the Maxwell equations in the form of asymptotic expansions of the Poincaré type:

$$H_j = \sum_{m=0}^{\infty} \delta^m H_j^{(m)}, \tag{3}$$

$$b = \sum_{m=0}^{\infty} \delta^m b_m, \tag{4}$$

where H_j ($j = x, y$) are the transverse magnetic field components of a given mode, $\delta = (k_0 w)^{-1}$, $b = (k_0^{-2}\beta^2 - \varepsilon_s)(\Delta\varepsilon)^{-1}$, and k_0 is the wavenumber of vacuum.

Realization of the corresponding procedure for $V = \delta^{-1}(\Delta\varepsilon)^{0.5}$ = const in the zero approximation leads to a

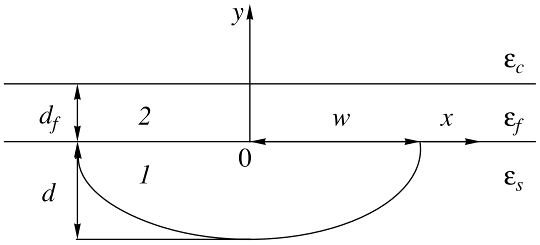

A schematic diagram of the structure studied: (*1*) waveguide; (*2*) adlayer.

scalar waveguide problem [10]:

$$\frac{\partial^2 u}{\partial \xi^2} + \frac{\partial^2 u}{\partial \eta^2} + V^2(f - b_0)u = 0, \quad (u)_{\eta = 0} \equiv 0, \qquad (5)$$
$$\lim_{\xi^2 + \eta^2 \to \infty} u = 0,$$

where $u = H_x^0$ or H_y^0. By considering a higher approximation (see [10]), it is possible to separate all modes into two types, H_x ($H_y^{(0)} \equiv 0$) and H_y ($H_x^{(0)} \equiv 0$), for which

$$b_1 = \varepsilon_f \varepsilon_s^{-1} k_f^{-1}$$
$$\times \frac{\cosh(k_f \bar{d}_f) + k_c k_f^{-1}(\varepsilon_f \varepsilon_c^{-1})\sinh(k_f \bar{d}_f)}{\sinh(k_f \bar{d}_f) + k_c k_f^{-1}(\varepsilon_f \varepsilon_c^{-1})\cosh(k_f \bar{d}_f)} VU \qquad (6)$$
$$(H_y^{(0)} \equiv 0),$$

$$b_1 = k_f^{-1} \frac{\cosh(k_f \bar{d}_f) + k_c k_f^{-1}\sinh(k_f \bar{d}_f)}{\sinh(k_f \bar{d}_f) + k_c k_f^{-1}\cosh(k_f \bar{d}_f)} VU \quad (H_x^{(0)} \equiv 0),$$
$$U = V^{-3} \int_{-\infty}^{\infty} \left(\frac{\partial u}{\partial \eta}\right)^2_{\eta = -0} d\xi \left(\int_{-\infty}^{\infty} \int_{-\infty}^{0} u^2 d\xi d\eta \right)^{-1}, \qquad (7)$$

where $k_c = \sqrt{\varepsilon_s - \varepsilon_c}$, $k_f = \sqrt{\varepsilon_s - \varepsilon_f}$, $\bar{d}_f = k_0 d_f$. Taking into account the condition $\bar{d}_f \ll 1$ (usually valid for real adlayers) and using Eqs (4), (6), and (7), we obtain

$$\varepsilon_f = \frac{\varepsilon_c \varepsilon_s \Delta\beta_y}{\varepsilon_s \Delta\beta_x - k_c^2 \Delta\beta_y}, \quad d_f = \frac{2k_c^2 \sqrt{\varepsilon_s}\Delta\beta_y}{k_0^2(\varepsilon_f - \varepsilon_c)R},$$
$$\Gamma_f = \frac{2k_c^2 \sqrt{\varepsilon_s}\Delta\beta_y}{k_0^2 R}\left(\frac{d\varepsilon_c}{dc}\right)^{-1}. \qquad (8)$$

Here, $\Delta\beta_x$ and $\Delta\beta_y$ are readily measurable (see [3]) increments of $\Delta\beta$ for the H_x and H_y modes, respectively; $R = (\Delta\varepsilon)^{1.5}U$; $d\varepsilon_c/dc$ is the value known for many gases and liquids; and c is the adlayer concentration [1].

Expressions (8) present an analytical solution to the inverse problem under consideration. This solution is much simpler than those reported previously [3, 8] (obtained within the framework of a planar waveguide). An important feature of our solution is that the dependence of the restored quantities ε_f, d_f, and Γ_f on the channel waveguide parameters is described by a single coefficient R. In principle, the R value can be calculated even after solving problem (5). However, this solution implies knowledge of the waveguide permittivity profile. Since experimental determination of the parameters of a real channel waveguide is a separate, and rather difficult, problem [11], it would be expedient to measure the R value rather than calculate this coefficient. The measurement can be taken based on our recent results [10], according to which this quantity for a channel waveguide without an adsorption layer can be expressed as

$$R = 4\sqrt{\varepsilon_s} k_c^3 k_0^{-1} \partial\beta_y / \partial\varepsilon_c. \qquad (9)$$

The right-hand part in Eq. (9) can be estimated by measuring the difference $\overline{\Delta\beta_y} = \beta_y(\varepsilon_c + \Delta\varepsilon_c) - \beta_y(\varepsilon_c)$ at a sufficiently small increment of $\Delta\varepsilon_c$ and by approximately taking $\partial\beta_y/\partial\varepsilon_c = \overline{\Delta\beta_y}/\Delta\varepsilon_c$. Such measurements can be readily performed with the aid of immersion liquids with known ε_c values [12]. Thus, the parameters of an adlayer on the surface of a channel OWG can be restored, based on Eqs. (8), from measurements of the increments of the propagation constants for the quasi-TE and quasi-TM modes provided the coefficient R is preliminarily determined.

Now, we will verify the above restoration scheme by determining the parameters of an adlayer of protein deposited onto the surface of a single-mode ion-exchange channel OWG in glass. For this purpose, we will use a computational experiment aimed at calculating the mode propagation constants $\beta_j(0)$ ($j = x, y$) and $\beta_j(d_f)$ characterizing the channel OWG without and with an adlayer, respectively. The calculation was conducted using a more accurate (as compared to the asymptotic procedure) method of variational separation of variables [13].

Consider a waveguide structure with the parameters $\varepsilon_s = 2.296$, $\Delta\varepsilon = 0.024$ [14], and $\varepsilon_c = 1.777$ at $\lambda_0 = 632.8$ nm. For the permittivity profile of the ion-exchange channel OWG in glass, we use the model [14]

$$f(\xi, \eta) = \exp(-\xi^2)\operatorname{erfc}(\eta F), \qquad (10)$$

where $F = wd^{-1}$ and d is the parameter characterizing the waveguide thickness (see figure). Taking $F = 1$, $V = 5.8$ (for which the channel waveguide is single-mode), and $d\varepsilon_c/dc = 0.501$ ml/g, $\varepsilon_f = 2.062$, $d_f = 6$ nm, and $\Gamma_f = 341$ ng/cm^2 (the latter values correspond to an adlayer of human immunoglobulin [1]). Using the restoration procedures described above, we obtain $R = 4.47 \times 10^{-4}$ (for $\Delta\varepsilon_c = 0.1$), $d_f = 5.83$ nm, $\varepsilon_f = 2.067$, and $\Gamma_f = 336.78$ ng/cm^2. These values of the adlayer parameters correspond to the relative errors

$$|\delta\varepsilon_f||\varepsilon_f - \varepsilon_c|^{-1} = 0.016, \quad |\delta d_f| d_f^{-1} = 0.028,$$
$$|\delta\Gamma_f|\Gamma_f^{-1} = 0.012,$$

which are related to the linear approximations employed in the dependences of $b(\delta)$ and $b_1(\bar{d}_f)$ and the finite differences $\Delta\bar{\beta}_y$ and $\Delta\varepsilon_c$ used in determining R by formula (9). These values of uncertainty indicate that the proposed approach is acceptable.

REFERENCES

1. Ph. M. Nellen and W. Lukosz, Biosens. Bioelectron. **6**, 517 (1991).
2. M. Tabib-Azar and G. Behelm, Opt. Eng. **36** (5), 1307 (1997).
3. B. J. Luff, S. Wilkinson, J. Pichler, *et al.*, J. Lightwave Technol. **16** (4), 583 (1998).
4. H. Haga and S. Yamamoto, J. Lightwave Technol. **6** (6), 1024 (1988).
5. R. B. Charters, S. E. Staines, and R. P. Tatam, Opt. Lett. **19** (23), 2036 (1994).
6. K. Tiefenthaler and W. Kukosz, J. Opt. Soc. Am. B **6** (2), 209 (1989).
7. W. Lukosz, Sens. Actuators B **29**, 37 (1995).
8. I. U. Primak and A. B. Sotskiĭ, Dokl. Akad. Nauk Belarusi **42** (2), 69 (1998).
9. L. D. Hutcheson, *Integrated Optical Circuits and Components* (Marcel Dekker, New York, 1987).
10. A. B. Sotskiĭ, I. U. Primak, and L. I. Sotskaya, Zh. Prikl. Spektrosk. **67** (3), 390 (2000).
11. S. J. Hosain, J. P. Meunier, E. Bourillot, *et al.*, Fiber Integr. Opt. **14** (1), 89 (1995).
12. V. I. Borisov and A. I. Voitenkov, Zh. Tekh. Fiz. **51** (8), 1668 (1981) [Sov. Phys. Tech. Phys. **26**, 958 (1981)].
13. A. B. Sotskiĭ, L. I. Sotskaya, and Yu. D. Stolyarov, Izv. Vyssh. Uchebn. Zaved., Radiofiz. **30**, 1470 (1987).
14. M. N. Weiss and R. Srivastava, Appl. Opt. **34** (3), 455 (1995).

Translated by P. Pozdeev

Technical Physics Letters, Vol. 28, No. 12, 2002, pp. 1043–1045. Translated from Pis'ma v Zhurnal Tekhnicheskoĭ Fiziki, Vol. 28, No. 24, 2002, pp. 48–52.
Original Russian Text Copyright © 2002 by Korepanov, Lisitsyn, Oleshko, Tsypilev.

Pulsed Cathodoluminescence of Heavy Metal Azides

V. I. Korepanov, V. M. Lisitsyn,
V. I. Oleshko, and V. P. Tsypilev

Tomsk Polytechnical University, Tomsk, Russia
e-mail: korepan@iit.b10.tpu.edu.ru

Received May 14, 2002; in final form, July 15, 2002

Abstract—The first results of an investigation into the spectral and kinetic characteristics of a pulsed cathodoluminescence from polycrystalline heavy metal azides at an excitation level below the explosion initiation threshold are presented. It is established that the emission from AgN_3, PbN_6, and TlN_3 at 300 K measured in the interval of quantum energies from 1.5 to 3.5 eV represents weakly structured broad bands limited by the fundamental absorption edge of each material, with a characteristic decay time of $\tau < 20$ ns. At 30 K, TlN_3 exhibits luminescence in the interval from 1.5 to 2.5 eV with a maximum at 1.85 eV decaying on a microsecond time scale. The temperature dependence of the spectral and kinetic parameters of emission was studied. *© 2002 MAIK “Nauka/Interperiodica”.*

Heavy metal azides (HMAs) represent explosive initiators and serve as model objects for investigating the mechanisms of the explosion decomposition of such substances. With respect to the electron structure, HMAs belong to semiconductors with a bandgap width of about 3.5 eV and, hence, admit the excitation of visible luminescence. To date, considerable experimental material has been gained on the so-called explosion emission from HMAs. The explosion emission takes place at a level of electron or laser excitation above the explosion initiation (detonation) threshold and is detected with a certain delay relative to the excitation pulse [1, 2]. Information available on the stationary photo- and thermostimulated luminescence of HMAs excited below the detonation threshold is rather restricted [3, 4].

Evidently, development of the models of initiation of the explosion decomposition process requires elucidating the primary processes occurring in HMAs under electron or laser excitation conditions. A valuable source of data about these processes is offered by the luminescence excited by nanosecond electron pulses with an energy per pulse below the explosion initiation threshold. Despite the obvious need for these data, no such investigations have been reported to the best of our knowledge.

In this context, the aim of our experiments was to detect and study the pulsed cathodoluminescence from heavy metal azides excited by a high-current electron beam with an energy density below the explosion initiation threshold. The objects for investigation were powdered azides of silver (AgN_3), lead (PbN_6), and thallium (TlN_3). The compounds were synthesized by method of double stream crystallization [5]. The samples were prepared by pressing powders into disks at a pressure of 10^6 Pa with a diameter of 5 mm and a thickness of 200–300 μm.

The spectra were excited by a pulsed high-current electron accelerator operating at an average electron energy of 300 keV, a pulse duration of ~20 ns, and an energy density per pulse of 0.01–0.03 J/cm^2. The luminescence was analyzed using an MDR-23 monochromator and detected by a FEU-118 photoelectron multiplier connected to a C8-14 storage oscillograph. The time resolution of the setup was ~10 ns, and the spectral resolution was ~0.02 and ~0.01 eV in the shortwave and longwave range, respectively. The emission spectra were normalized taking into account the spectral sensitivity of the optical channel of the spectrometer. The pulsed spectrometer is described in more detail elsewhere [6]. The samples were mounted in a crystal holder of a vacuum cryostat with a residual gas pressure of about 10^{-3} Pa.

Figure 1 shows typical room-temperature cathodoluminescence spectra of AgN_3, PbN_6, and TlN_3 measured at a maximum of the emission pulse. In the spectral range studied, the pulsed emission from all the studied azides represents wide weakly structured bands limited by a fundamental absorption edge on the shortwave side (see the data for HMAs in [7]). It was established that the luminescence decay time for all samples in the temperature range from 30 to 300 K does not exceed the excitation pulse duration (≤20 ns). According to the preliminary estimates, the energy yield of luminescence from all HMAs is relatively low. Under otherwise equal excitation conditions, a maxi-

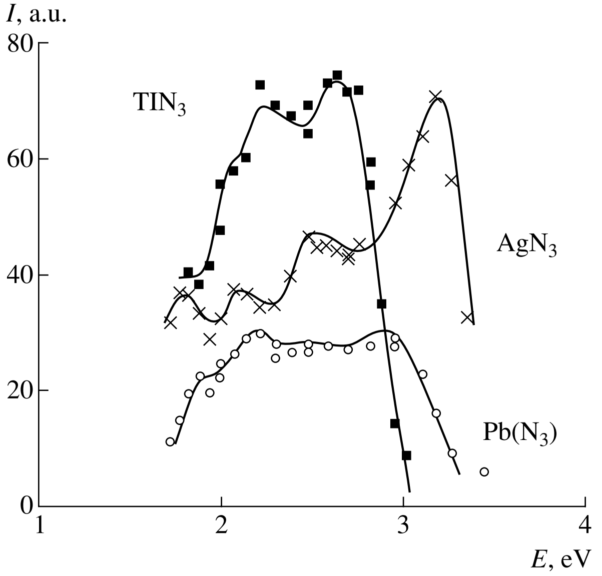

Fig. 1. Typical pulsed cathodoluminescence spectra of heavy metal azides measured at 300 K.

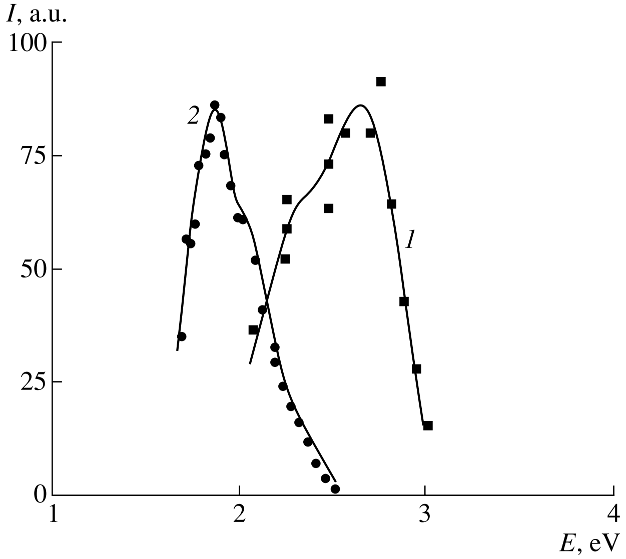

Fig. 2. The spectra of pulsed cathodoluminescence of TlN$_3$ measured at 30 K, showing the components decaying on the (*1*) nanosecond and (*2*) microsecond scale.

mum emission intensity was observed for thallium azide.

The samples of thallium azide measured at temperatures below 60 K exhibited an additional slowly decaying emission in the form of two overlapping bands with a common maximum at $E = 1.85$ eV (Fig. 2, curve *2*), the amplitude of which (but not the integral energy emitted) was about ten times lower as compared to that of the fast pulsed cathodoluminescence response. The emission decay kinetics at the maximum of this band measured at 30 K could be described by a sum of two exponents with characteristic decay times of $\tau_1 = 5$ μs and $\tau_2 = 50$ μs. The shape of the band measured at 30 K does not change with time in the course of the emission intensity decay. As can be seen from a comparison of the spectra of TlN$_3$ depicted in Figs. 1 and 2, the shape of the fast cathodoluminescence component depends on the excited sample temperature. While the intensity of this component (peaking at 2.7 eV) remains virtually unchanged over the broad temperature range (30–300 K) studied, the intensity of emission in the interval from 1.5 to 2.5 eV is significantly depressed when the temperature decreases from 60 to 30 K. For the same change in the temperature, the intensity of the slow emission component (peaking at 1.85 eV) in the spectrum of TlN$_3$ increases by a factor of about ten.

Thus, the samples of HMAs studied exhibit the cathodoluminescence properties typical of solids with sufficiently large bandgaps. For electron beam excitation at energies below the detonation threshold, these compounds behave much like the representatives of semiconducting and insulating materials, in which irradiation leads to the effective production of electron–hole pairs, followed by their partial radiative recombination. Many of these materials also exhibit a wideband fast pulsed cathodoluminescence with a relatively low energy yield [8]. This emission is usually attributed to interband transitions. The spectrum is limited only by the fundamental absorption edge of a crystal, the emission characteristics are independent of the sample temperature, and the luminescence decay time is on the order of several picoseconds.

Since the spectrum of the fast emission component observed for a pulsed electron beam excitation of TlN$_3$ clearly depends on the temperature (Figs. 1, 2), it would be expedient to interpret this emission as a luminescence of some other kind. In this case, the excitation can lead to the creation of short-lived radiolysis products, followed by recombination of the geminate electron–hole pairs in the course of recharge of the radiation-induced radicals of both intrinsic and impurity (or near-impurity) types. A high initial defect density in HMAs makes the formation of a large number of various electron excitations possible, which accounts for the wideband emission. Indirect evidence is provided by the results of the investigation of photoconductivity in AgN$_3$ performed in [3], the spectral dependence of which shows a clear correlation with the luminescence spectrum observed in our experiments. However, elucidation of the nature of both fast and slow (low-temperature) luminescence components requires additional investigation.

Acknowledgments. This study was supported by the “Scientific-Innovative Cooperation” program.

REFERENCES

1. B. P. Aduev, É. D. Aluker, and A. G. Krechetov, Pis'ma Zh. Tekh. Fiz. **22** (6), 24 (1996) [Tech. Phys. Lett. **22**, 236 (1996)].
2. B. P. Aduev, É. D. Aluker, Yu. A. Zakharov, *et al.*, Pis'ma Zh. Éksp. Teor. Fiz. **66** (2), 101 (1997) [JETP Lett. **66**, 111 (1997)].
3. G. M. Diamant and S. V. Kolbasov, Zh. Fiz. Khim. **65** (6), 1475 (1991).
4. Yu. A. Zakharov, S. I. Rukoleev, and V. S. Loskutrov, Khim. Vys. Énerg. **13** (1), 61 (1979).
5. S. I. Kurakin, G. M. Diamant, and V. M. Pugachev, Izv. Akad. Nauk SSSR, Neorg. Mater. **26** (11), 2301 (1990).
6. V. I. Korepanov, V. M. Lisitsyn, V. V. Strezh, *et al.*, Fiz. Tverd. Tela (Leningrad) **27** (10), 3052 (1985) [Sov. Phys. Solid State **27**, 1832 (1985)].
7. F. P. Bowden and A. D. Yoffe, *Fast Reactions in Solids* (Academic, New York, 1958; Inostrannaya Literatura, Moscow, 1962).
8. F. A. Savikhin and V. P. Vasil'chenko, Fiz. Tverd. Tela (St. Petersburg) **39** (4), 613 (1997) [Phys. Solid State **39**, 535 (1997)].

Translated by P. Pozdeev

Technical Physics Letters, Vol. 28, No. 12, 2002, pp. 1046–1048. Translated from Pis'ma v Zhurnal Tekhnicheskoĭ Fiziki, Vol. 28, No. 24, 2002, pp. 53–57.
Original Russian Text Copyright © 2002 by O. Pozdnyakov, Redkov, A. Pozdnyakov.

Thermal Stability of the Films of Polystyrene Chemically Bound to Fullerene C_{60}: Effect of Film Thickness in the Submicron Range

O. F. Pozdnyakov, B. P. Redkov, and A. O. Pozdnyakov
Ioffe Physicotechnical Institute, Russian Academy of Sciences, St. Petersburg, 194021 Russia
e-mail: ao.pozd@pop.ioffe.rssi.ru

Received July 5, 2002

Abstract—The thermal stability of polymer films with thicknesses in the submicron range was studied for a composition of polystyrene (PS) chemically bound (grafted) to fullerene C_{60}. It is shown that the thermal stability of PS–fullerene (PSF) films depends on their thickness δ. For $\delta > 10$ nm, there appears an additional low-temperature thermal degradation stage, in which the rate of polymer decomposition increases proportionally to the film thickness. The energy parameters of both stages in the thermal degradation kinetics are determined. A decrease in the thermal stability of PSF films is explained by the chemical activity of radicals formed in the initial stage of thermal decomposition of the PSF macromolecules. It is concluded that this effect is indicative of an excessive film thickness and can serve as a probe for the critical film thickness and its inhomogeneity in a submicron range. *© 2002 MAIK “Nauka/Interperiodica”.*

Films with dimensions on a nanometer scale attract special attention and are widely employed in modern and advanced technologies. Quasi-two-dimensional polymer films possess special properties not inherent in bulk polymers [1, 2]. This study continues our investigations into the effect of fullerene C_{60} on the thermal stability of polymer–fullerene compositions.

Previously [3–5], we demonstrated that the thermal stability of a polystyrene grafted onto fullerene (PSF) significantly decreases as compared to that of pure polystyrene (PS), which is manifested by the thermal degradation temperature in the former case being ~100 K lower than that in the latter case. However, the rates of the low-temperature degradation of PSF (the process responsible for a decreased thermal stability of the polymer) reported by various researchers exhibit a considerable scatter [4, 5]. At the same time, analysis of the available data indicates that there is ongoing extensive investigation into the polymer–fullerene systems [6, 7], including PSF [6].

Our subsequent investigations of the properties of ultrathin films of various polymer–fullerene compositions showed, first for an amylacrylate–amylmethacrylate copolymer [8] and now for PSF, that a factor determining variations in the thermal stability of nanodimensional (10–1000 nm) polymer films is the material thickness. It was suggested [8] that the effect of the film thickness is related to the chemical activity of radicals formed in the initial stage of thermal degradation of the polymer. The results of investigations of the PSF films have allowed us, on the one hand, to understand the reasons for the aforementioned discrepancies [4, 5] and, on the other hand, to find certain common features in the thermal stability of fullerene-containing polymer films in the range of submicron thicknesses.

This study was performed with the same PSF composition as that used previously [3–5], the structure of which comprises six arms of low-molecular-weight PS macromolecules chemically grafted onto C_{60} ($(\mathrm{PS})_6$–C_{60}) [5]. Thin PSF films of a required thickness were prepared using a dilute solution of this composition in toluene. A certain amount of this solution was applied to an oxidized tantalum substrate provided with a heater and a thermocouple. The substrate with the applied sample was placed into the vacuum chamber of a mass spectrometer (of the MX-1320 type) and heated at a rate of 3 K/s. The average thickness δ of a dry film was calculated using the known values of the volume, area, and concentration of a solution applied to a substrate.

The thermal degradation kinetics in PSF films was studied by measuring the temperature dependence of the intensity of selected peaks (104 D, styrene monomer; 720 D, fullerene) in the mass spectra of samples. The peak height in the mass spectrum is proportional to the rate of production of styrene monomers (dN_{St}/dt) and fullerene molecules (dN_{C60}/dt).

Figure 1 (curves *a*–*c*) shows the temperature dependence of dN_{St}/dt for PSF films of various thicknesses ($\delta = 2.3, 23, 46$ nm). As can be seen, the rate of material degradation in the low-temperature stage increases in proportion to the film thickness. Indeed, only a weak “shoulder” is observed on the low- temperature branch of the main degradation profile (Fig. 1, curve *a*), with a peak at $T^{\max} = 410 \pm 5$°C, for the film with $\delta = 2.3$ nm. In the curves for $\delta = 23$ and 46 nm, the shoulder evolves into an intense, well-resolved kinetic peak at $T_1^{\max} = 325 \pm 5$°C, which can even exceed the main peak height (Fig. 1, curve *c*). The activation energy of the PSF degradation process, as determined from the temperature dependence of dN_{St}/dt in the initial stage (below 300°C) amounts to 123 kJ/mol.

Figure 1 (curve *d*) also shows the temperature variation of dN_{C60}/dt for the 46-nm-thick PSF film. As can be seen, C_{60} is liberated from the film predominantly in the initial stage of thermal degradation ($T_{C_{60}}^{\max} \cong 350$°C). The activation energy of this process (120 kJ/mol) is close to that determined for styrene monomers.

Figure 2 presents the dN_{St}/dt profile for a two-layer PSF–PS system. This film, representing a model object, was prepared by depositing first a 2.3-nm-thick PSF film and then (after drying the film) a layer of pure PS with the same molecular weight ($M_n \sim 1400$) and a thickness of 23 nm. As is known [1, 3], pure PS in both thin and thick films with thicknesses up to 100 nm exhibits a single-mode character of thermal degradation with $T^{\max} \geq 420$°C. However, measurements of the two-layer film revealed a clear intense low-temperature process with the same $T^{\max} \sim 325$°C as above. We believe that this result is direct evidence of the leading role of the chemically active products of decomposition of PSF molecules formed in the initial degradation stage. Although the nature of the observed radicals has still not been established, we may suggest that these products represent free radical species of the C_{60}• or C_{60}–*R*• type, since other types of free radicals are usually present among the degradation products of normal PS.

Other interesting results to be noted are (i) the almost equal and (ii) low activation energies determined for both styrene and fullerene (123 and 120 kJ/mol) in comparison to the activation energy of degradation of the bulk PS (230 kJ/mol) [3]. Attributing the decrease in the activation energy (by ≅110 kJ/mol) to the energy of initiation E_i of the bond breakage event (without a change in the activation energy of the other elementary degradation stages—kinetic chain transfer and termination), we can estimate (by analogy with [9]) the E_i value for the primary broken bonds in PSF. This yields 130 kJ/mol against $E_i \sim 300$ kJ/mol for C–C bonds in the PS backbone.

Thus, a change in the thermal stability of the nanodimensional fullerene-containing polymer films studied is related to a weak chemical binding of PS to C_{60}. The formation of free radical species upon decomposition of $(PS)_{60}$–C_{60} macromolecules in the low-temperature region and their retention in thick films can activate the degradation of PS molecules in the course of the intermolecular kinetic chain transfer reaction. For very thin (in the limiting case, monomacromolecular) films, the active radicals leave the film without entering into intermolecular contacts and, hence, without causing any decrease in the thermal stability.

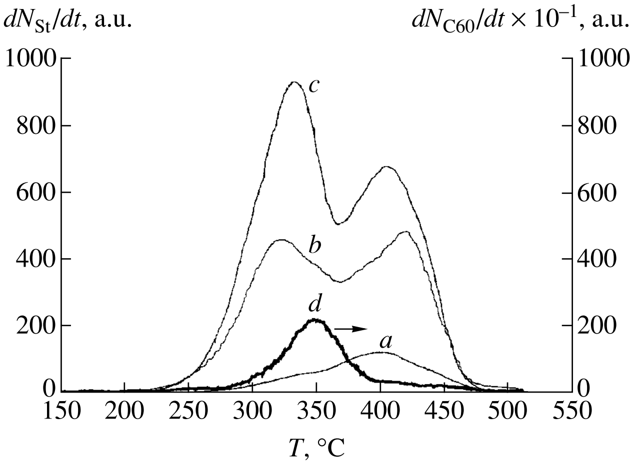

Fig. 1. Plots of the rate of (*a*–*c*) styrene formation (dN_{St}/dt) and (*d*) fullerene evolution (dN_{C60}/dt) during thermal degradation of a PSF film with a thickness of (*a*) 2.3, (*b*) 23, and (*c*, *d*) 46 nm.

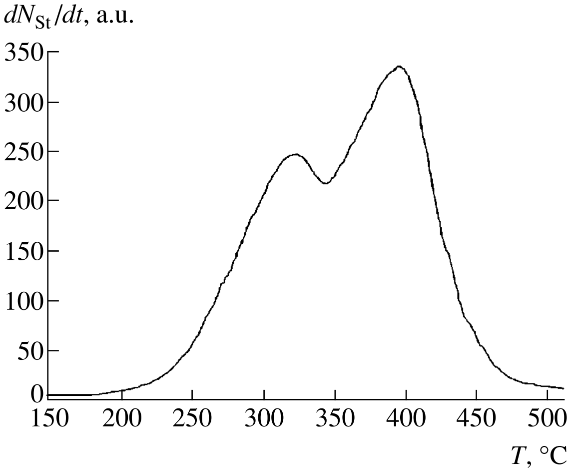

Fig. 2. Temperature variation of the rate of styrene formation during heating of a two-layer PSF–PS film. See the text for explanations.

Proportionality of the layer thickness to the rate of the low-temperature thermal degradation allows this process to be used as a probe for the critical film thickness in other analogous polymer–fullerene compositions. This probe can be used to characterize the degree of inhomogeneity of the film thickness in the submicron range.

Acknowledgments. This study was supported by the “Low-Dimensional Quantum Structures” program of the Presidium of the Russian Academy of Sciences.

REFERENCES

1. I. C. McNeil and M. A. J. Mohammed, Eur. Polym. J. **8**, 975 (1972).
2. O. F. Pozdnyakov, V. R. Regel’, B. P. Redkov, *et al.*, Vysokomol. Soedin., Ser. A **20** (11), 2494 (1978).
3. B. M. Ginzburg, A. O. Pozdnyakov, V. N. Zgonnik, *et al.*, Pis’ma Zh. Tekh. Fiz. **22** (4), 73 (1996) [Tech. Phys. Lett. **22**, 166 (1996)].
4. A. O. Pozdnyakov, O. F. Pozdnyakov, B. P. Redkov, *et al.*, Pis’ma Zh. Tekh. Fiz. **22** (18), 57 (1996) [Tech. Phys. Lett. **22**, 759 (1996)].
5. E. Yu. Melenevskaya, L. V. Vinogradova, L. S. Litvinova, *et al.*, Vysokomol. Soedin., Ser. A **40** (2), 247 (1998).
6. C. Mathis, S. Nunige, F. Audouin, and R. Nuffer, Synth. Met. **121**, 1153 (2001).
7. N. V. Kamanina, Synth. Met. **127**, 121 (2002).
8. O. F. Pozdnyakov, B. P. Redkov, G. K. Lebedeva, *et al.*, Pis’ma Zh. Tekh. Fiz. **28** (5), 38 (2002) [Tech. Phys. Lett. **28**, 188 (2002)].
9. H. H. G. Jellinek and M. D. Luh, Makromol. Chem. **115** (2719), 89 (1968).

Translated by P. Pozdeev

Technical Physics Letters, Vol. 28, No. 12, 2002, pp. 1049–1051. Translated from Pis'ma v Zhurnal Tekhnicheskoĭ Fiziki, Vol. 28, No. 24, 2002, pp. 58–62.
Original Russian Text Copyright © 2002 by Samokhvalov, Davydov.

Determination of the Parameters of Phosphor Activators in Thin-Film Electroluminescent Capacitor Structures

M. K. Samokhvalov and R. R. Davydov
Ul'yanovsk State Technical University, Ul'yanovsk, Russia
e-mail: sam@ulstu.ru

Received July 8, 2002

Abstract—A method for determining the concentration and electron-impact excitation cross section of activated emission centers in the phosphor layer of a thin-film electroluminescent capacitor structure, based on measurements of the brightness as a function of the applied alternating voltage amplitude and frequency, is analyzed. The error of determination of the parameters of electroluminescence excited by alternating-sign ramp voltage is evaluated. The parameters of electroluminescent structures based on the ZnS:Mn, $ZnS:TbF_3$, and $ZnS:SmF_3$ films are presented. © *2002 MAIK "Nauka/Interperiodica".*

Both basic investigations of the electroluminescence in thin-film structures and the production of electroluminescent (EL) display elements and devices requires the development of methods for monitoring the parameters of emission-active layers in EL thin film structures. The principal functional characteristics of such light-emitting devices pumped with an alternating voltage are given by the dependences of brightness on the applied voltage amplitude and frequency.

Based on the model of tunneling electron emission from traps at the phosphor–dielectric interface and direct impact excitation of the activated emission centers in a phosphor layer [1], we have obtained the following expression for the brightness B of a thin-film EL structure as a function of the applied voltage amplitude V_A and frequency f [2]:

$$B = \left[\frac{W}{B_0} + \frac{\pi}{\eta_0 k f (V - V_{th})}\right]^{-1}. \qquad (1)$$

Here, B_0 and η_0 are the maximum brightness and light efficiency; $k = 4CC_D C_L^{-1} V_{th}$; C, C_D, and C_L are the capacitances of the whole EL structure and the dielectric and phosphor layers, respectively; V_{th} is the threshold voltage of the EL capacitor structure; and W is a coefficient describing the features of electroluminescence excitation in a given structure. According to this relationship, by plotting the experimental data in the $1/B$ versus $1/f$ or $1/(V - V_{th})$ coordinates, we can determine the maximum brightness B_0 and the maximum light efficiency η_0. These effective characteristics are determined by the properties of the materials employed and the design features, while being independent of the excitation conditions [3].

In contrast, the quantity W is determined by the features of electroluminescence excitation, namely, by the interaction of accelerated electrons with excited emission centers [2]:

$$W = \frac{1}{BQ_T}\int_0^T j(t)B(t)dt,$$

where $j(t)$ is the current through the phosphor and Q_T is the charge carried by this current over the period T of voltage variation. The value of W, determined by numerical methods for sufficiently high frequencies, is $W \approx 1$ [2–4].

In order to estimate the accuracy of the approximation employed, which characterizes a methodological uncertainty in the electrical measurements involved, we analytically calculated the coefficient W for electroluminescence excited by an symmetric alternating-sign ramp signal. In this case, the quasistationary self-screening in the phosphor upon emission excitation is characterized by a constant current determined by the ramp slope: $j_D = C_D dV/dt$ [4]. Taking into account the Talbot law, we obtain

$$W = \frac{T}{2\Delta t_B}\left(\frac{B_C \Delta t_C}{B_B \Delta t_B} + 1\right)^{-1},$$

where B_B and B_C are the average values of brightness for the time periods corresponding to emission buildup (Δt_B) and decay (Δt_C), respectively. However, experimental determination of these parameters is extremely difficult. Taking into account linear variation of the applied voltage with time and assuming that there are a

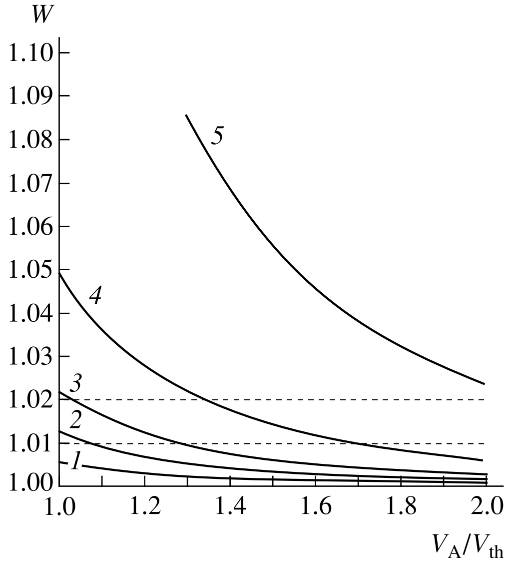

Fig. 1. Plots of the parameter W versus the V_A/V_{th} ratio calculated for ZnS:Mn phosphor operating at various ramp frequencies f = 1.5 (*1*), 1 (*2*), 0.75 (*3*), 0.5 (*4*), and 0.25 kHz (*5*).

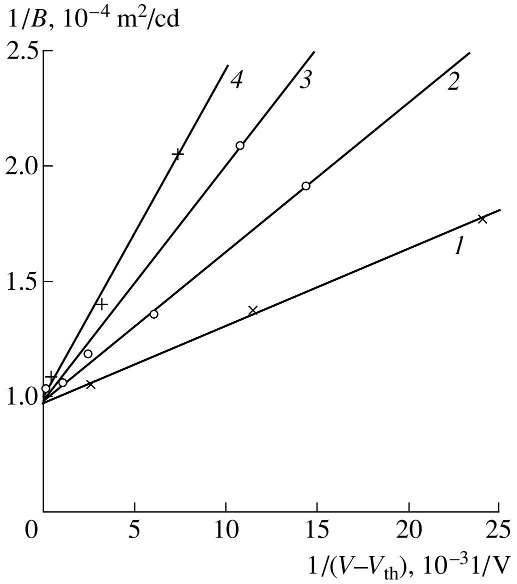

Fig. 2. Plots of the inverse brightness $1/B$ versus inverse voltage amplitude $1/(V–V_{th})$ for various excitation voltage frequencies f = 1.5 (*1*), 1 (*2*), 0.75 (*3*), and 0.5 kHz (*4*).

linear buildup and exponential decay of the brightness, the above expression can be transformed to

$$W = \left[1 + \frac{V_{th}}{V}\left(4f\tau\frac{V}{V_{th}}\tanh\left(\frac{1}{4f\tau}\frac{V_{th}}{V}\right) - 1\right)\right]^{-1},$$

where τ is the time constant of relaxation of the activated emission centers.

Figure 1 plots W versus the relative amplitude of ramp voltage of various frequencies for EL layers of zinc sulfide doped with manganese (τ = 1.3 ms [5]). As can be seen, the coefficient W decreases with increasing frequency. For $f \geq 1.2$ kHz, the methodological uncertainty does not exceed 1% for any voltage amplitude. For the EL layers of ZnS:TbF$_3$ (τ = 0.64 ms) and ZnS:SmF$_3$ (τ = 0.27 ms) [5], the corresponding minimum frequencies are 2 and 5 kHZ, respectively. Additional methodological uncertainties can be related to leaks in the dielectric (in the case of EL excited in strong electric fields) and to variations in the active current level (in the case of EL excited slightly above the threshold).

We have experimentally studied the properties of thin-film EL capacitors using multilayer metal–dielectric–phosphor–dielectric–transparent electrode systems prepared by vacuum deposition on glass substrates. For the phosphor layer, we used films of zinc sulfide doped with manganese (0.5 at.%), terbium fluoride (5 at.%), or samarium fluoride (3 at.%) with a thickness of 1.0–1.5 μm. The dielectric layers were obtained by depositing solid solutions of zirconium and yttrium oxides with a thickness of 0.2–0.3 μm [5]. The sample structures were characterized by measuring their voltage–brightness characteristics and the frequency dependences of integral brightness for EL structures excited by a symmetric alternating-sign ramp signal.

Figure 2 shows typical experimental plots of the brightness versus excitation voltage amplitude plotted for various frequencies in the $1/B$ versus $1/(V - V_{th})$ coordinates. As seen from these data, the experimental plots are well approximated by straight lines intersecting at the same point on the ordinate axis. Using these plots, it is possible to determine the B_0 and η_0 values. The uncertainty was determined by the error in the

Parameters of thin-film EL structures based on doped zinc sulfides

Phosphor	Maximum brightness B_0, cd/m^2	Maximum light efficiency η_0, lm/W	Concentration of emission centers N, cm^{-3}	Excitation cross section σ, cm^2
ZnS:Mn	10246	7.6	3.3×10^{18}	1.4×10^{-16}
ZnS:TbF$_3$	6718	1.4	5.6×10^{17}	1.0×10^{-16}
ZnS:SmF$_3$	825	0.3	3.6×10^{15}	5.4×10^{-16}

brightness measurements: for a semiconductor photometer of the FPCh type employed, this error reached up to 10%.

Using the maximum brightness and light efficiency values determined in this way, we calculated the values of concentration N and the electron-impact excitation cross section σ of the activated emission centers in the EL films studied [3]. The results of experimental investigation of the thin-film EL structures are listed in the table. Our results agree with the values reported by other researchers [1] and with the experimental data determined for analogous structures studied using different methods [5].

These experimental data can be used for the investigation of electroluminescence in thin films and for monitoring the parameters of phosphors and thin-film EL display devices.

Acknowledgments. This study was performed within the framework of the Federal Target Program "Integration" (project no. B-0107).

REFERENCES

1. A. N. Georgobiani and P. A. Pipinis, *Tunneling Phenomena in Luminescence of Semiconductors* (Mir, Moscow, 1994).
2. M. K. Samokhvalov, Zh. Tekh. Fiz. **66** (10), 139 (1996) [Tech. Phys. **41**, 1045 (1996)].
3. M. K. Samokhvalov, R. R. Davydov, and É. I. Khadiullin, Pis'ma Zh. Tekh. Fiz. **27** (8), 74 (2001) [Tech. Phys. Lett. **27**, 341 (2001)].
4. M. K. Samokhvalov, Pis'ma Zh. Tekh. Fiz. **20** (6), 67 (1994) [Tech. Phys. Lett. **20**, 246 (1994)].
5. I. Yu. Brigadnov and M. K. Samokhvalov, Izv. Vyssh. Uchebn. Zaved., Mater. Élektron. Tekh., No. 3, 64 (1998).

Translated by P. Pozdeev

Technical Physics Letters, Vol. 28, No. 12, 2002, pp. 1052–1053. Translated from Pis'ma v Zhurnal Tekhnicheskoĭ Fiziki, Vol. 28, No. 24, 2002, pp. 63–66.
Original Russian Text Copyright © 2002 by Morozov, Semashko.

On the Mass Separation of Quasineutral Beams

A. I. Morozov and N. N. Semashko

Nuclear Fusion Institute, Kurchatov Institute of Atomic Energy, State Scientific Center of the Russian Federation, Moscow, Russia

Received July 11, 2002

Abstract—A refined scheme of operation of a system capable of separating a quasineutral mixed ion flux into components with equal masses of particles is proposed. *© 2002 MAIK “Nauka/Interperiodica”.*

Introduction. Modern plasma technologies require the development of methods for the creation of electric fields of various configurations and orientations in a plasma. One direction in this research is related to the wake field acceleration process (involving small times and giant field strengths); the other direction is plasma optics dealing with stationary electric fields of relatively small strengths (~100–1000 V/cm). The problem considered below pertains to a plasma-optical system (POS).

The principles of POS operation were formulated by Morozov in [1] and then developed both theoretically and experimentally [2, 3]. This research led to the creation of plasma-optical lenses, recuperators, and plasma accelerators, including plasma thrusters for space vehicles [4].

The main advantage of plasma-optical systems is their ability to control high-current quasineutral beams with the aid of both magnetic and electric fields. In order to provide for this possibility, it is necessary that the electric and magnetic fields in the system be everywhere mutually orthogonal (for $T_e \longrightarrow 0$); that is [1, 3],

$$\Phi = \Phi(\gamma), \tag{1}$$

where γ is the magnetic field line index. Condition (1) is usually inconsistent with the Laplace equation ($\Delta\Phi = 0$) for fields in vacuum. However, there are cases in which $\Phi(x)$ satisfies both condition (1) and the Laplace equation ($\Delta\Phi = 0$). Such systems, called transitive, can be strictly realized when the magnetic field lines are straight (in axisymmetric systems, these lines have to be oriented in radial directions). Systems with planar fields can also be transitive.

Mass-separating POS. Of special interest among POSs are the mass separating systems in which a quasineutral mixed ion flux is separated into components with equal masses of particles (provided that all ions are singly charged). A detailed scheme of such a device, referred to below as a plasma-optical mass separator (POMS), was originally given in [2]. This POMS exhibits three important features (see figure).

(i) The system is axisymmetric: the fields (**E** and **H**) form a poloidal configuration, electrons drift by closed azimuthal trajectories, and the ion source is ring-shaped.

(ii) An azimutator—which is a device with a sufficiently strong radial magnetic field—is placed at the entrance to the focusing space region. As a result, the velocity of a particle changes from $\mathbf{v}_0 = (v_{or}, 0, v_{oz})$ in front of this device (where $v_{or} \ll v_{oz} \approx v_0$) to $\mathbf{v}_1 = (v_{or}, v_\theta, v_z)$ where $v_\theta^2 + v_z^2 = v_0^2$. Owing to the law of conservation of momentum $rv_\theta = -\frac{e}{c}\frac{\psi}{M}$,

$$\psi = \delta(rA_z). \tag{2}$$

The azimuthal velocity component acquired by a particle past the azimutator depends (for $v_{\theta 0} \approx 0$) only on the mass of the particle.

(iii) Passing the azimutator, the particles enter the focusing space confined between the two coaxial cylinders to which different potentials are applied. The resulting electric field, while not influencing the motion of particles along the Z axis, affects the v_z and v_θ components and is capable of focusing particles in the (r, θ) plane (over the azimuthal interval of $\delta\theta = \pi/\sqrt{2}$, as in the Hughes–Rozhanski energy analyzer). Obviously, focusing will also take place in the (r, z) coordinates.

In order to create an electric field in the focusing space in the presence of a quasineutral particle beam, it is necessary to generate a homogeneous longitudinal magnetic field that will provide for the validity of condition (1), that is, to magnetize electrons. For this purpose, it is sufficient to generate a field with a strength on the order of several dozens of oersteds, which will virtually not influence the ion flux dynamics. The ring focus will be situated at a distance

$$L = \frac{\pi}{\sqrt{2}}\frac{v_{1z}}{v_{1\theta}}$$

from the azimutator.

A schematic diagram of the axisymmetric mass separator.

POMS operation refined. Denoting by R_0 the azimutator slit radius, we can calculate the electric field at this radius such that a certain "central" mass M_0 will obey the equilibrium condition

$$\frac{M_0 v_{\theta 0}^2}{R_0} = eE_0.$$

Being displaced in azimuth by $\pi/\sqrt{2}$, the particles possessing a "central" mass will exhibit focusing at the same $r = R_0$. However, the particles with $M > M_0$ and $M < M_0$ will be focused at $r < R_0$ and $r > R_0$, respectively. For the masses close to M_0, the focus shift is

$$\delta r = R_0 \frac{(-\delta M)}{M_0}, \quad M = M_0 + \delta M.$$

Calculations show that a POMS with properly selected parameters can provide for a panoramic mass separation in the range from $M \sim 50$ to 200 amu in the same setup. It should be noted that the requirements to the ion beam at the source output are rather easy to meet.

Estimates. Experiments performed with plasma accelerators of the plasma thruster type showed that the ion bean density at the output can be up to ≤ 1 A/cm^2 for $M \sim 100$ amu and a particle energy of within ~100–1000 eV. For $R \sim 1$ m and a beam width of ~1 cm, the total ion current is ~700 A. With these beam parameters, the total mass ($M \sim 100$ amu) processed by one POMS per year will be about 10–15 ton (provided that the working process is not be adversely influenced by instabilities).

Acknowledgments. The authors are grateful to their colleagues A.P. Shubin[†], V.V. Savel'ev, and V. K. Naumov for participating in this study. Special thanks to V.P. Smirnov for his interest in the problems studied.

REFERENCES

1. A. I. Morozov, Dokl. Akad. Nauk SSSR **163** (6), 1363 (1965) [Sov. Phys. Dokl. **10**, 775 (1966)].
2. A. I. Morozov and S. V. Lebedev, *Reviews of Plasma Physics*, Ed. by M. A. Leontovich (Atomizdat, Moscow, 1974; Consultants Bureau, New York, 1980), Vol. 8.
3. A. I. Morozov, in *Encyclopedia of Low-Temperature Plasma*, Ed. by V. E. Fortov (Nauka, Moscow, 2000), Vol. III, p. 435.
4. A. I. Morozov, in *Encyclopedia of Low-Temperature Plasma*, Ed. by V. E. Fortov (Nauka, Moscow, 2000), Vol. III, p. 443.

Translated by P. Pozdeev

[†] Deceased.

Technical Physics Letters, Vol. 28, No. 12, 2002, pp. 1054–1057. Translated from Pis'ma v Zhurnal Tekhnicheskoĭ Fiziki, Vol. 28, No. 24, 2002, pp. 67–74.
Original Russian Text Copyright © 2002 by Serov, Bel'skaya, Margolin, Potsar.

Effect of Fractal-Matrix Resonators on the Properties of Thin Copper Films

I. N. Serov[a],*, G. N. Bel'skaya[b], V. I. Margolin[b],, and N. A. Potsar[b]**
[a] *AIRES Research Center, Foundation for Development of Novel Medical Technologies, St. Petersburg, Russia*
** e-mail: foundation@aires.spb.ru*
[b] *St. Petersburg State Electrotechnical University, St. Petersburg, 197376 Russia*
*** e-mail: vlad@margolin.etu.spb.ru*

Received July 22, 2002

Abstract—The effect of fractal-matrix resonators of AIRES type, situated outside the discharge zone, on the properties of thin (submicron) copper films obtained using magnetron ion sputtering is studied. Using the proposed technique, it is possible to obtain copper films of submicron thickness with local regions representing self-organized fractal structures. © *2002 MAIK "Nauka/Interperiodica".*

Development of submicron and nanodimensional technology provides for a permanent decrease in the dimensions of the elements of electronic devices and related structural elements. The ideal, which already seems possible, is the direct atomic assembly of devices on a substrate by means of a tunneling-probe transfer of separate atoms or atomic clusters. However, practical use of the atomic assembly techniques, such as tunneling-probe transfer, requires prolonged (on the order of 10^2 h) continuous deposition of about 100 atoms per second from a point of the tunneling probe device in order to provide for a compact coverage of an area on the order of 1 μm^2. Therefore, it seems more realistic to employ "collective" methods capable of processing the whole substrate (or a considerable part of it).

Of considerable interest in this respect is the obtaining of thin films possessing an ordered structure arising primarily as a result of initiation of self-organization processes in the course of layer growth. Using such ordered structures, it will be possible to obtain elements of microelectronic devices possessing ultrasmall dimensions without recourse to the methods of atomic assembly. There are known methods for obtaining bulk self-organized structures under the action of external factors. According to these methods, it is necessary to provide for a certain intensity of external action to ensure a transition of the system into a special nonlinear region called the state far from equilibrium [1]. In this state, local changes spread over the whole system, thus initiating the development of long-range correlations. As a result, the system response to external action becomes collective and also spreads over the entire volume [2].

The aforementioned external action can take the form of a hard energetic factor, such as ion or laser beams used for the modification of metal surfaces and the creation of spatially-organized structures [2]. Alternatively, the structuring agent can be represented by microwave [3] or X-ray [4] radiation. The question as to how a processed system accumulates the required energy and passes to a coherent behavior requires special investigations and can be considered within the framework of the BIP theory [5].

With a view to provide for the obtainment of self-organized thin-film structures, we studied the magnetron ion deposition of thin (submicron) copper films onto silicon substrates with the aid of fractal-matrix resonators of the AIRES type. These devices are based on a specially synthesized line hologram, with a line thickness presently on the order of 1.0 μm [6].

The method of magnetron ion sputtering in the standard regime provides for the obtainment of thin films that virtually completely cover a substrate and reproduce its shape [7]. The experiments were performed on a magnetron sputtering setup based on a commercial vacuum stage of the VUP-4 type as modified at the Department of Electronic and Vacuum Technology of the St. Petersburg State Electrotechnical University. A special magnetron sputtering device with a cathode diameter of 40 mm was mounted on the vacuum chamber lid. A power source provided a voltage of up to 1 kV and a discharge current of up to 2.5 A. The distance from the cathode to the substrate was 80 mm. It was also possible to apply a constant potential to the substrate holder ranging from 0 to ±300 V. The magnetron device was based on a barium magnet and allowed easy replacement of the cathode.

The films were deposited onto substrates representing ⟨100⟩ oriented single crystal silicon wafers of 76 KDB-7.5 grade. The cathodes were made of electrolytic copper. The samples of thin-film structures were studied with a MII-4 optical interferometer and an SM-

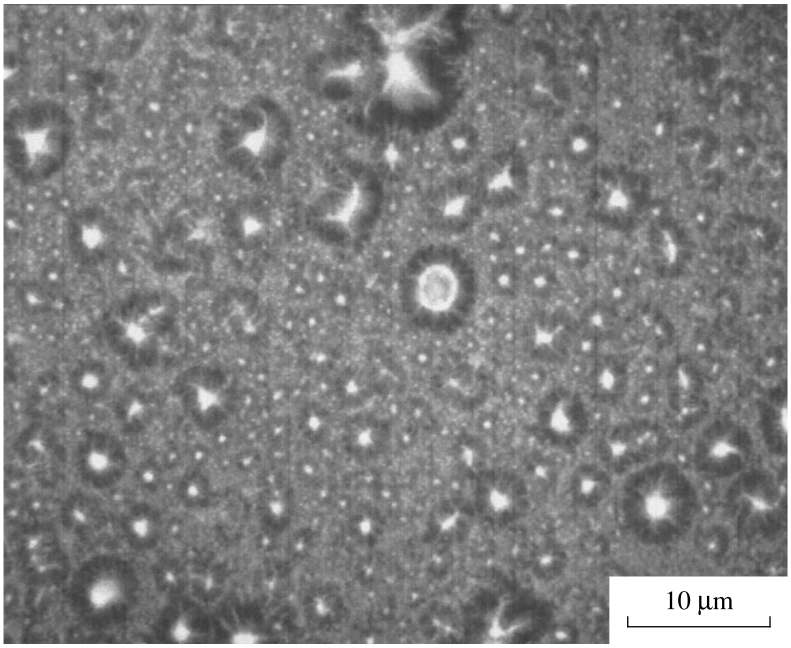

Fig. 1. A microphotograph of the fractal structures formed in the peripheral region of a substrate.

LUX HL optical microscope. The images were recorded with a digital camera of VNC-702 type. The copper film thicknesses ranged from 0.4 to 0.9 μm.

The experimental procedure was as follows. In the beginning of each experimental cycle, a copper film was deposited onto control substrates in the absence of AIRES resonators. The resulting films virtually repeat the substrate structure and exhibit no elements of ordering and self-organization. Then, the films were deposited onto silicon substrates in the presence of AIRES resonators arranged inside the vacuum chamber in a certain manner. The experiments were performed either with or without direct contact between substrates and resonators. In the case of such contact, a resonator or a system of resonators was mounted on the substrate outside the region of discharge operation. In the absence of contact, the resonators were arranged according to a certain scheme outside the discharge region at a certain distance from the substrates.

The results of the experiments are as follows. Microscopic examination showed that the copper films deposited in the presence of AIRES resonators exhibit certain but quite variable structures possessing a fractal character. The phase composition of the deposit was monitored using X-ray diffraction. Figure 1 shows a microphotograph demonstrating the formation of sufficiently ordered structures of a circular or spherical shape. On passage from the periphery to the center of the plate, the size of the ring-shaped elements exhibits a tendency to increase. The elements exhibit a certain distribution of dimensions from small to large. At the center of the plate, there are large ring-shaped elements with a height roughly estimated as reaching up to several microns.

It should be noted that the elements formed in this central region possess a much more complicated morphology (Fig. 2) as compared to that of the element situated at the periphery. The inner space of the large elements found in the central region contains nuclei arranged in a regular manner. Found outside the large ring-shaped elements are analogous elements of smaller size, both separate and forming complicated interpenetrating structures. On the whole, the pattern reveals a complicated fractal structure possessing, according to our analysis, several levels of self-organization and self-similarity. On the passage from the periphery to the center of the substrate (according to the experimental conditions, this corresponds to increasing action of the resonators on the film growth process), the structures acquire an increasing degree of self-organization: each cluster is characterized by several fractal levels.

As the time of deposition (and, hence, the copper film thickness) increases, even the peripheral region exhibits a fractal pattern of large and small ring-shaped elements. The large rings are surrounded by smaller ones, which, in turn, form a kind of circular structure and so on.

The passage from the periphery to the center of a thicker deposit reveals a certain hierarchy of fractal levels related to a large film thickness. All elements exhibit, besides the above described planar geometry, a certain dome-shaped structure. Some elements appear in the form of truncated trigonal, tetragonal, and hexagonal quasipyramids (Fig. 3) surrounded by analogous

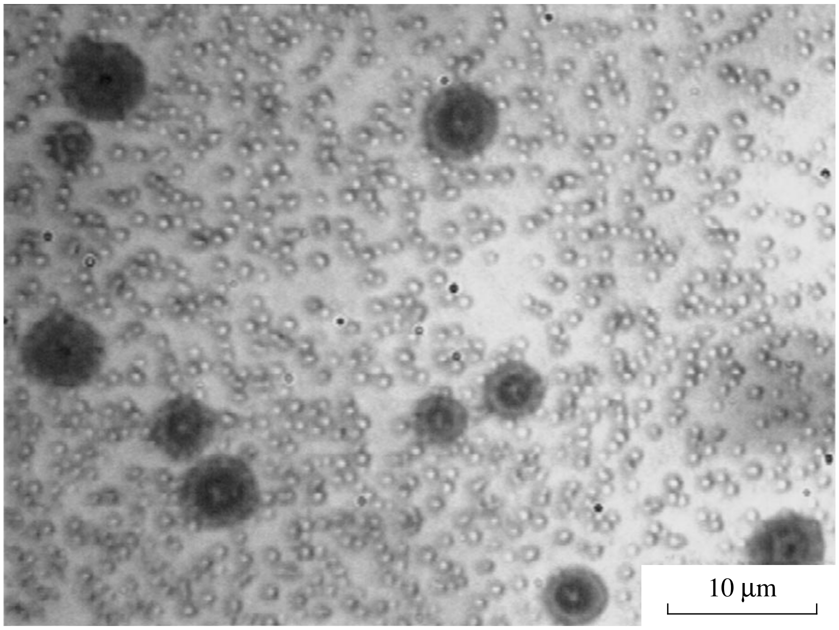

Fig. 2. A microphotograph of the fractal structures formed in the central region of a substrate.

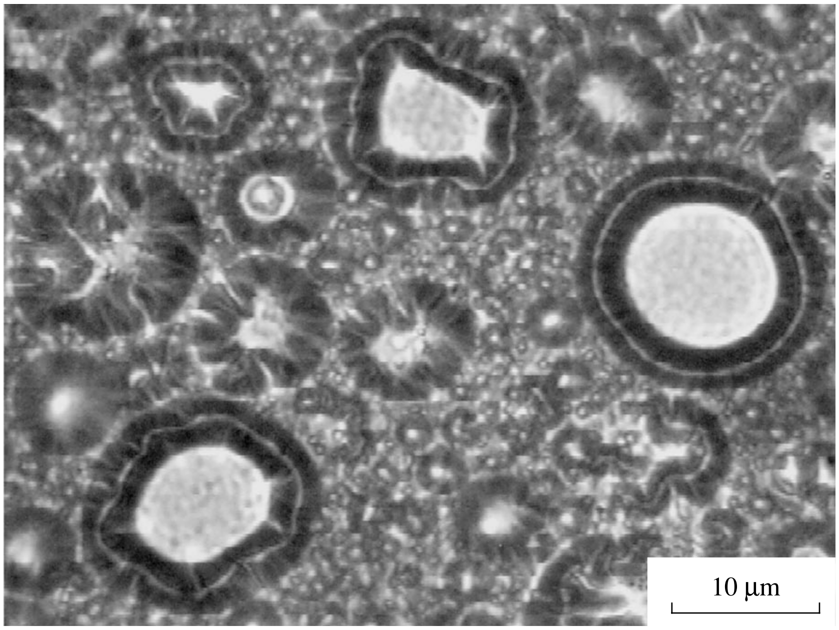

Fig. 3. A microphotograph of the fractal structures formed in the region of maximum resonator action.

smaller elements. Some of these quasipyramids possess a central depression resembling a crater. Some elements appear in the form of dome-shaped helical formations with a fractal structure.

The character of the film structure can be generally described as follows. The peripheral regions, showing evidence of an edge effect, contain coarse ring-shaped fractal formations with evidence of the “cloning” process inside each element. All these coarse formations possess a pronounced vertical component and appear as dome-shaped formations, some of which contain internal craters. The density of the elements significantly increases in the central regions of the substrates. This is accompanied by an increase in the maximum size of ring-shaped and dome-shaped elements with an internal hierarchy of levels. Thus, the films represent fractal objects with a complicated hierarchy of structural levels.

It was established that when the passage from one sample to another proceeds under identical conditions of deposition and process parameters, the film structure exhibits evolution toward a more pronounced fractal pattern and increasing size of elements. This fact indicates that the film is a certain kind of replica of resonator structure (by analogy with the films deposited onto structural elements). This leads to the shape memory effect, as confirmed by the results of experiments using highly fractal copper films as quasi-resonators. In the subsequent experiments, it will be possible to select a configuration, structure, and arrangement of resonators so as to provide for a controlled growth of self-organized ordered structures on a submicron film. This approach corresponds to the aforementioned principles of "collective" methods and can be used to obtain submicron electronic devices.

Acknowledgments. The authors are grateful to Prof. O.V. Frank-Kamenetskaya and to T.N. Kamenskaya, the head of the X-ray Laboratory, for the X-ray diffraction characterization of the copper films and fruitful discussions of the results.

REFERENCES

1. G. Nicolis and I. Prigogine, *Self-Organization in Non-Equilibrium Systems* (Wiley, New York, 1977; Mir, Moscow, 1979).
2. V. S. Khmelevskaya, Soros. Obraz. Zh. **6** (6), 85 (2000).
3. S. S. Berdonosov, Soros. Obraz. Zh. **7** (1), 32 (2001).
4. V. N. Peregudov, É. M. Pashaev, and S. N. Yakunin, in *Proceedings of All-Russia Scientific and Technical Conference "Micro- and Nanoelectronics," 2001*, Vol. 2, p. 33.
5. I. N. Serov, *General Course of BIP* (Aktsident, St. Petersburg, 2002).
6. A. V. Alekseĭtsev, G. N. Bel'skaya, B. É. Bonshtedt, *et al.*, in *Proceedings of XIX Russian Conference on Electron Microscopy, Chernogolovka, 2002*, p. 26.
7. I. Brodie and J. J. Muray, *The Physics of Microfabrication* (Plenum, New York, 1982; Mir, Moscow, 1985).

Translated by P. Pozdeev

Technical Physics Letters, Vol. 28, No. 12, 2002, pp. 1058–1059. Translated from Pis'ma v Zhurnal Tekhnicheskoĭ Fiziki, Vol. 28, No. 24, 2002, pp. 75–79.
Original Russian Text Copyright © 2002 by Buchin, Denisenko, Rudakov.

Forming Through Channels in Silicon Substrates

É. Yu. Buchin, Yu. I. Denisenko, and V. I. Rudakov
Institute of Microelectronics and Informatics, Russian Academy of Sciences, Yaroslavl, Russia
e-mail: imi.buchin@rambler.ru

Received July 19, 2002

Abstract—A new method of silicon processing, based on the selective electrochemical etching of p^+-type regions formed in an n-type matrix by thermal migration of aluminum, is proposed. A special advantage offered by this technique is the possibility of obtaining through channels with a cross section of arbitrary shape and a characteristic transverse size ranging from 20 to 200 μm. © *2002 MAIK "Nauka/Interperiodica".*

The possessing unique electronic properties and high mechanical characteristics, single crystal silicon finds increasing application in various micromechanical devices. Designing such devices frequently entails the forming of holes in silicon wafers. This task can be solved using a number of methods, including laser drilling, etching in a high-density plasma, alkaline anisotropic etching of (110)-oriented silicon crystals, and anodic etching in hydrofluoric acid based acid electrolytes. The advantages and drawbacks of these techniques are well known.

Below, we propose a new method of silicon processing based on liquid-phase etching of the p^+-type regions formed in an n-type silicon matrix by thermal migration of an aluminum zone.

The process of thermal migration or zone melting under temperature gradient conditions, which is used in the first stage of the proposed procedure for the through local doping of silicon, possesses a large technological potential [1]. Figure 1a schematically illustrates this process by showing the migration of a liquid zone representing an eutectic Al–Si melt in an n-type silicon substrate. The liquid zone migrates, whereby silicon is dissolved on the hot side, transferred by diffusion through the melt, and allowed to crystallize on the cold side of the migrating zone. The concentration of aluminum in the recrystallized layer is determined by the limiting solubility of the metal in silicon ($\sim 2 \times 10^{19}$ cm^{-3} at 1100–1200°C). The liquid zone travels in the direction of the temperature gradient and emerges at the opposite surface of the substrate. The thermal migration velocity is higher by 3–5 orders of magnitude as compared to the velocity of atomic transport in the course of traditional diffusion in solids. As a result, an extended p^+-type region is formed in the n-type silicon matrix along the liquid zone trajectory. The shape of the cross section (circle, square, triangle) of this region is determined by the shape of a deposited aluminum spot, while the depth of penetration is determined by the time of processing at a given temperature gradient ∇T and by a particular substrate material.

The second stage of the process under consideration consists in selective removal of the p^+-type region, with the formation of through channels with a desired shape of the transverse cross section. This can be effected by chemical or electrochemical liquid-phase etching of the

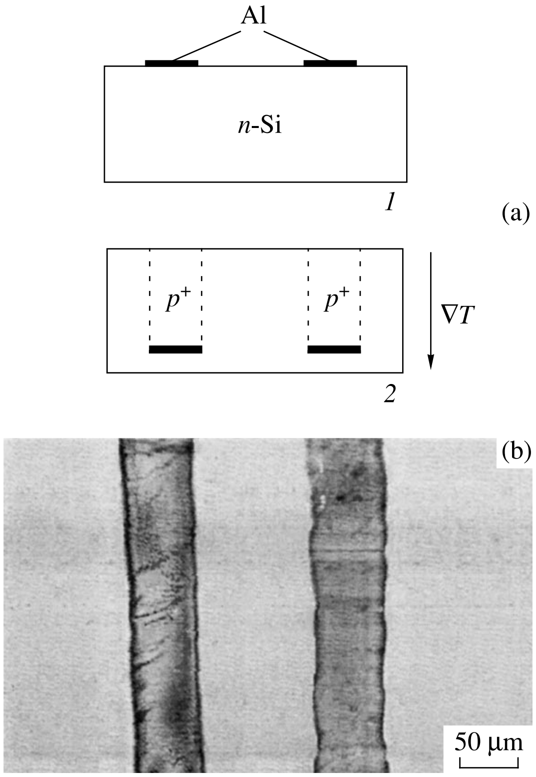

Fig. 1. Thermal migration of a liquid aluminum eutectic zone from the (*1*) cooled to (*2*) IR-heated side of an n-type silicon plate: (a) schematic diagram of the initial and final stages of the process; (b) microphotograph showing the through doped p^+-type channels in the transverse cleavage of a silicon plate upon the thermal migration of aluminum and additional chemical decoration of the p–n junction.

1063-7850/02/2812-1058$22.00 © 2002 MAIK "Nauka/Interperiodica"

modified silicon regions. For a selective removal of the p^+-type region from an n-type silicon matrix by chemical etching, it is recommended to use highly dilute solutions of the HNO_3–HF–H_2O or HNO_3–HF–CH_3COOH systems [2]. However, this process is characterized by a relatively low etching rate (several tenths of a micron per minute). For an electrochemical process (silicon anodizing in HF-based electrolytes), this rate can be about ten times higher. As is known, a necessary condition for silicon dissolution in this process is the presence of a certain density of holes on the semiconductor surface in contact with the electrolyte. In silicon of the p type, holes are the majority carriers, whereas their density in the n-type material is small. By choosing the etching process conditions so as to suppress the mechanisms of additional charge carrier production (photogeneration, avalanche multiplication at high applied voltages, etc.), it is possible to ensure selective etching of only the p^+-type regions in the substrate material. However, the process of silicon anodizing conducted at low applied voltages and current densities favors pore formation. The resulting porous region has to be subsequently removed, for example, by dissolving this material in a strongly diluted alkaline solution [3].

Our experiments were performed with (100)-oriented silicon wafers of KEF-4.5 grade with a diameter of 100 mm and a thickness of 460 μm. The thermal migration process was effected in a thermal gradient setup employing IR heating [4]. The initial wafer with electron-beam deposited, 3-μm-thick 60 × 40 μm rectangular aluminum spots was heated from rear side up to a temperature of 1100°C. The temperature of the front side, on which the melted zone entered the substrate, was 8–10°C lower due to conduction heat exchange with the water-cooled copper holder. The thermal migration time was about 25 min, the process termination being detected with the aid of a pyrometer. Then, the substrate was cooled, extracted from the working chamber, and cut into 40 × 40 mm plates. Figure 1b shows a microphotograph of a through doped channel observed in the transverse cleavage of a silicon plate upon the thermal migration of aluminum and additional chemical decoration of the p–n junction.

We performed selective anodic etching of the samples in a vertical Teflon electrochemical cell with a platinum counterelectrode. The electrolyte represented a mixture of hydrofluoric acid with isopropyl alcohol (1 : 1, v/v). The etching process was conducted in the dark in a galvanostatic regime, with a local current density in the p-type region of 60 mA/cm^2 at a voltage of 5–7 V. The etching rate reached 5 μm/min. For the obtaining of through channels, the etching process was terminated at a distance of 10–15 μm from the rear side of the sample plate. Then, the sample was rinsed in distilled water, dried in an air flow, and ground so as to remove a 20-μm-thick layer from the rear side. A porous silicon layer was removed from the channels by etching with a 1% potassium hydroxide solution. Figure 2 shows the image of a plate with through holes of a nearly rectangular shape. If necessary, the inner channel walls can be rendered more smooth by additional chemical polishing.

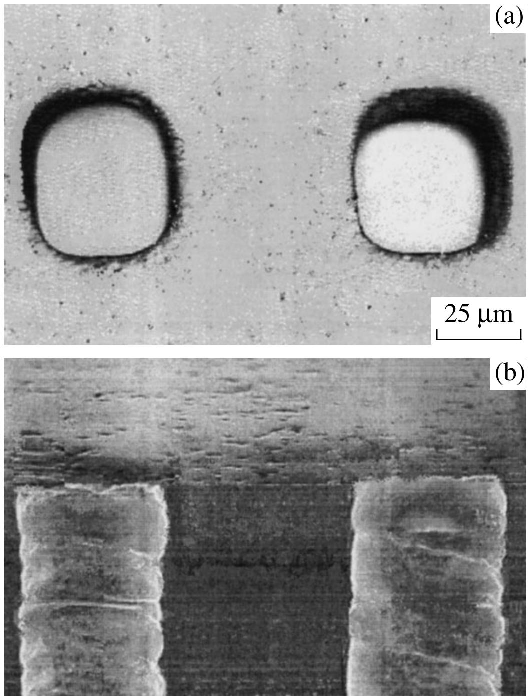

Fig. 2. Through channels in a silicon plate: (a) microphotograph; (b) electron-microscopic image of the transverse cleavage.

The proposed method is cheaper as compared to the plasmachemical etching techniques and more universal than all other methods of through channel formation mentioned above. However, this technique also has certain limitations related to the process of thermal migration. First, the shape of the final channel cross section is somewhat more rounded than that of the initial aluminum spot. Second, the size of the channel cross section is restricted to a range of 20–200 μm. Thermal migration of the liquid zone of a smaller size is accompanied by instability of the trajectory (which results in random deviations of the doped channel), while the melting zone of a greater size can split into smaller fragments.

REFERENCES

1. V. I. Rudakov and L. A. Koledov, in *Foreign Electron Engineering: Scientific and Technical Collection* (TsNII “Élektronika”, Moscow, 1993), pp. 27–60.
2. B. Schwartz and H. Robbins, J. Electrochem. Soc. **123** (12), 1903 (1976).
3. X. G. Zhang, S. D. Collins, and R. L. Smith, J. Electrochem. Soc. **136** (5), 1561 (1989).
4. B. V. Mochalov and V. I. Rudakov, Prib. Tekh. Éksp., No. 2, 155 (1996).

Translated by P. Pozdeev

Technical Physics Letters, Vol. 28, No. 12, 2002, pp. 1060–1064. Translated from Pis'ma v Zhurnal Tekhnicheskoĭ Fiziki, Vol. 28, No. 24, 2002, pp. 80–88.
Original Russian Text Copyright © 2002 by Okulov.

Instability of an Equilibrium Circular Configuration of Helical Vortices

V. L. Okulov
Institute of Thermal Physics, Siberian Division, Russian Academy of Sciences, Novosibirsk, Russia
e-mail: okulov@itp.nsc.ru

Received July 8, 2002

Abstract—The problem of stability of an equilibrium circular configuration of N helical vortices is analytically studied for the first time. A solution is obtained that provides for an effective analysis of the cases of stable vortex systems (pair, triplet, etc.) observed in practice. The algebraic representation for the angular rotation velocity of a system of N helical vortices, obtained as an additional intermediate result, is simpler as compared to the other known asymptotic expressions and allows calculations to be performed with high precision over the entire range of helix pitch variation. © *2002 MAIK “Nauka/Interperiodica”.*

Stable pairs of helical vortices have been repeatedly observed in various vortex flows, for example, in tornado eyes, in wake streams behind propellers, upon vorticity breakdown above delta-shaped wings and in tubes, in technological vortex chambers of various configurations, in turbulent flows featuring pairs of coherent vortex structures, and in other systems. A triplet of helical vortices is much less frequently observed in real flows, and a configuration of four vortices is an even less stable object. In the course of the preliminary experiments with a rectangular vortex chamber described in [1], quadruple vortex structures were observed only for a very short period of time and rapidly decayed.

The problem of the stability of an equilibrium circular configuration comprising N vortex structures has been theoretically studied only for a polygonal system of N point vortices or straight vortex filaments (the limiting case of a helical vortex with infinite pitch). According to the results of investigations performed by Kelvin, Thomson, and Havelock [2], such a system can loss stability only when the number of point vortices is $N \geq 7$. This result, obtained in the simplest particular case, is obviously at variance with the aforementioned observations.

In this context, the study aimed, for the first time, at finding analytically the conditions of stability for an equilibrium configuration comprising N identical thin helical vortices with intensity Γ, pitch h (below, the pitch is expressed as $l = h/2\pi$), and axes determined by the screw lines $X_n = (a\cos(\theta + n\delta), a\sin(\theta + n\delta), a\tau(\theta + n\delta))$ lying on a cylinder of radius a (coaxial with the z axis) with an equal shift $\delta = 2\pi/N$ by the angle θ and with a common dimensionless step $\tau = l/a$. The vortex cores are assumed to possess a relative radius $\varepsilon \ll 1$ (with respect to the cylinder radius a). The unperturbed vortex system rotates about and uniformly moves along the cylinder axis.

In order to study instabilities in the above system, it is necessary to develop a simple and exact procedure for calculating the velocity field induced by helical vortex filaments. However, in this case (unlike that of straight filaments with a simple polelike solution), the Biot–Savart law cannot be integrated in an analytical form. Because of the presence of a singularity in the core, it is also difficult to use this law for direct numerical calculation of the velocity field. Known asymptotic solutions (see, e.g., [3]) cannot provide a sufficient accuracy in determining the velocity necessary to solve the problem of stability in the entire range of helical vortex pitch variation.

A different form of solution for a helical vortex filament in infinite space (see Eqs. (8), (9), (12), and (13) in [4]) and in a tube (see Eqs. (19) and (24) in [5]) has been written in terms of a Kapteyn series of the type

$$H_M^{I,J} = \sum_{n=1}^{\infty} m^M I_m^{\langle I\rangle}(mx) K_m^{\langle J\rangle}(my) e^{im\chi}, \qquad (1)$$

where x and y are the radial distances divided by the step l $(x \leq y)$ and $\chi = \theta - z/l$; $I_m^{(0)}(mx)$, $K_m^{(0)}(my)$ are the modified Bessel functions and $I_m^{(1)}(mx)$, $K_m^{(1)}(my)$ are the corresponding derivatives. The series (1) converges slowly, especially at the singular point $(x \longrightarrow y)$. In order to bypass this difficulty (for $x \longrightarrow y$; $M = 1$; $I, J = 0, 1$ or $1, 0$), Boersma and Wood [6] separated singularities with respect to the spatial variables from (1) and described the main twist effect (vortex pitch) using an integral residue W (see Eq. (4.1) in [6]). However, the residue W (as well as the Biot–Savart law) cannot be expressed in the form of finite integrals. Eventually, the rotation velocity of a configuration comprising one, two, three, or four helical vortices was numerically calculated [6, 7] up to the seventh decimal digit using 20 values of the step, the asymptotic expressions [3, 8] for the cases of small and large steps were refined, and the results were generalized to the case of N vortices.

According to an alternative method [5], the velocity and current function are determined upon directly separating from (1) the singularities written in distorted spatial variables explicitly taking into account the vortex twist. In contrast to the above approach, this method allows problems involving various numbers of helical vortices in the space to be solved and the flow characteristics to be calculated at any point with the required precision.

For studying the stability of an equilibrium circular configuration of N helical vortices, we will generalize the latter method for all types ($I, J = 0$ or 1) of series (1) appearing in the definitions of current function ($M = 0$), velocity field ($M = 1$), and its spatial derivatives ($M = 2$). To this end, let us formally replace the cylindrical functions in series (1) by their uniform high-order expansions (see Eqs. (9.7.7–10) in [9]). Upon convolution of the resulting series, the principal part $S_M^{I,J}$ of series (1) acquires the following form:

$$S_M^{I,J} = \lambda^{I,J}\left[a_M^{\langle 0\rangle}\frac{e^{\xi+i\chi}}{(e^{\xi}-e^{i\chi})^2} + a_M^{\langle 1\rangle}\frac{e^{i\chi}}{e^{\xi}-e^{i\chi}} + a_M^{\langle 2\rangle}\ln(1-e^{-\xi+i\chi}) + a_M^{\langle 3\rangle}\mathrm{Li}_2(e^{-\xi+i\chi}) + a_M^{\langle 4\rangle}\mathrm{Li}_3(e^{-\xi+i\chi})\right];$$

$$e^{\xi} = \frac{x}{y}\frac{e^{\sqrt{1+x^2}}(1+\sqrt{1+y^2})}{e^{\sqrt{1+y^2}}(1+\sqrt{1+x^2})};$$

$$\lambda^{(I,J)} = \frac{1}{2}\frac{(1+x)^{\frac{1}{2}-I}(1+y)^{\frac{1}{2}-J}}{x^{-I}(-y)^{-J}};$$

$$a_M^{\langle 0\dots 4\rangle} = \begin{bmatrix} 0 & 0 & 1 & \alpha^{(I,J)} & \beta^{(I,J)} \\ 0 & 1 & \alpha^{(I,J)} & \beta^{(I,J)} & \gamma^{(I,J)} \\ 1 & \alpha^{(I,J)} & \beta^{(I,J)} & \gamma^{(I,J)} & \delta^{(I,J)} \end{bmatrix},$$

where $\alpha^{(i,j)}$, $\beta^{(i,j)}$, $\gamma^{(i,j)}$, and $\delta^{(i,j)}$ are the polynomials of power 1 to 4 in functions u_n and v_n (see Eqs. (9.3.9–10) and (9.3.13–14) in [9]), which result from the multiplication of uniform expansions and depend on l. Thus, the singularities and their coefficients contain explicit information about the vortex twist. Note that the difference between $S_M^{I,J}$ and $H_M^{I,J}$ is very small (less than one per cent). Therefore, the problem under consideration is more effectively solved by representing series (1) through $S_M^{I,J}$ than by using the aforementioned asymptotic expressions, the best of which fail to work in an important interval of variation of the dimensionless helix pitch, $\tau = 0.8$–2 [6, 7].

In order to illustrate this statement, we will use the $S_M^{I,J}$ representation and determine the velocity of motion of the helical vortex system under consideration. This velocity consists of the self-induced velocity of a fixed vortex and the velocity induced by other vortices. The first component can be determined by using a representation through series (1) (see Section 4.1.1 in [3]), while the second component will be obtained as a sum of solutions from [4] expressed through series (1), shifted from a selected vortex with respect to the angular coordinate by $n\delta$ ($n = 1, \dots, N-1$). Replacing series (1) in the resulting expression by their principal parts $S_M^{I,J}$ and accomplishing time-consuming calculations involving the summation of singularities and polylogarithms uniformly arranged over the circle, we obtain the following formula for the angular velocity of a system of N helical vortices:

$$\frac{4\pi a^2}{\Gamma}\Omega = N - \frac{\tau}{\sqrt{1+\tau^2}} - \frac{\tau}{(\sqrt{1+\tau^2})^3}\left[\ln\left(\frac{\tau}{N(\sqrt{1+\tau^2})^3}\right)+1\right]$$
$$-\frac{\tau^3}{(\sqrt{1+\tau^2})^9}\left[\left(\tau^4-3\tau^2+\frac{3}{8}\right)\frac{\zeta(3)}{N^2}-\tau^4-3\tau^2-3-\frac{1}{\tau^2}\right] \quad (2)$$
$$-\frac{\tau}{(\sqrt{1+\tau^2})^3}\left[\ln\left(\frac{1+\tau^2}{\varepsilon}\right)+\frac{1}{4}\right],$$

where $\zeta(\cdot)$ is the Riemann zeta function. The angular velocities Ω' calculated using formula (2) without the last term and the values of Ω'_{WB} calculated using the W integral tabulated in [7] are presented for comparison in the table. It should be noted that the maximum difference does not exceed 0.2% in the entire range of the dimensionless step τ and that formula (2) is in fact simpler than the asymptotic expressions derived in [7].

The velocity of translational motion of the vortex system along the z axis can be determined from the relation $w_z + rw_\theta/l = \Gamma/2\pi l$ between the tangential and axial components of the velocity induced by helical vortices in infinite space [1, 5]. According to this, the circular configuration of helical vortices in the equilibrium state moves along the axis at a velocity of $U = (\Gamma/2\pi a - a\Omega)/\tau$ and rotates with an angular velocity of Ω as given be formula (2). In the limiting case of $\tau \longrightarrow \infty$, the system of straight vortices simply rotates with the velocity $\Omega = \Gamma(N-1)/4\pi a^2$ coinciding with the rotation velocity of a system of point vortices [2].

A comparison of the angular rotation velocities of a system of vortices calculated according to [7] and using formula (2)

τ	$N = 2$		$N = 3$		$N = 4$	
	$2\pi a^2\Omega'_{WB}/\Gamma$	$2\pi a^2\Omega'/\Gamma$	$2\pi a^2\Omega'_{WB}/\Gamma$	$2\pi a^2\Omega'/\Gamma$	$2\pi a^2\Omega'_{WB}/\Gamma$	$2\pi a^2\Omega'/\Gamma$
0.01	1.02149	1.02149	1.52352	1.52352	2.02495	2.02495
0.05	1.06700	1.06699	1.57710	1.57710	2.08427	2.08426
0.1	1.09850	1.09850	1.61850	1.61850	2.13268	2.13268
0.2	1.12433	1.12433	1.66271	1.66271	2.18988	2.18988
0.3	1.12316	1.12311	1.67674	1.67673	2.21472	2.21471
0.4	1.10818	1.10798	1.67271	1.67267	2.21866	2.21864
0.5	1.08673	1.08641	1.65782	1.65774	2.20881	2.20879
0.6	1.06258	1.06241	1.63656	1.63650	2.19003	2.19001
0.7	1.03742	1.03773	1.61164	1.61168	2.16561	2.16562
0.8	1.01199	1.01292	1.58472	1.58491	2.13780	2.13786
0.9	0.98668	0.98816	1.55686	1.55719	2.10818	2.10829
1	0.96178	0.96357	1.52883	1.52925	2.07786	2.07801
2	0.76622	0.76495	1.30363	1.30331	1.82988	1.82977
3	0.66451	0.66328	1.18667	1.18639	1.70148	1.70139
4	0.61110	0.61059	1.12549	1.12540	1.63476	1.63474
5	0.58025	0.58015	1.09026	1.09026	1.59655	1.59655
6	0.56088	0.56097	1.06822	1.06826	1.57274	1.57275
7	0.54791	0.54809	1.05351	1.05356	1.55690	1.55692
8	0.53878	0.53899	1.04319	1.04324	1.54582	1.54584
9	0.53210	0.53231	1.03566	1.03571	1.53777	1.53778
10	0.52706	0.52726	1.02999	1.03003	1.53171	1.53172

Upon going to the screw variables (r, χ) and the corresponding velocity projections (w_r, $w_\chi = w_\theta - w_z/\tau$) [1, 5], the problem of the stability of the vortex configuration studied reduces to a two-dimensional case. Let the kth vortex shift from the equilibrium position to a point ($a + r_k$, $2\pi n/N + (\Omega - U/l)t + \chi_k$). Then, in the linear approximation, the perturbed equations of motion of the kth vortex are as follows:

$$\frac{dr_k}{dt} = \frac{\Gamma}{\pi\alpha}\frac{1}{\tau^2}\mathrm{Re}\left\{\chi_k \sum_{n(n\neq k)} S_2^{1,1}\left(a, a, \frac{2\pi(n-k)}{N}\right) - \sum_{n(n\neq k)} \chi_n S_2^{1,1}\left(a, a, \frac{2\pi(n-k)}{N}\right)\right\},$$

$$a\frac{d\chi_k}{dt} = \frac{\Gamma}{\pi a^2}\frac{1}{\tau^2}\mathrm{Re}\left\{r_k \sum_{n(n\neq k)}\left[\frac{\tau^2+1}{\tau^2}S_2^{1,1}\left(a, a, \frac{2\pi(n-k)}{N}\right) + \frac{1-\tau^2}{\tau}S_1^{0,1}\left(a, a, \frac{2\pi(n-k)}{N}\right)\right] + \frac{(\tau^2+1)^2}{\tau^2}\sum_{n(n\neq k)} r_n S_2^{1,1}\left(a, a, \frac{2\pi(n-k)}{N}\right)\right\} - \frac{\tau^2+1}{\tau^2}\Omega r_k. \quad (3)$$

In system (3), the Kapteyn series (1) in expressions for the field derivatives were replaced by their principal parts $S_M^{I,J}$. Following [2], we can seek solutions to the system in the form of $r_k = \alpha(t)e^{2\pi km/N}$ and $\chi_k = \beta(t)e^{2\pi km/N}$, where m is the subharmonic wavenumber running through integer values in the interval $[0, N-1]$. For $m = 0$, all vortices behave in the same manner and the resulting system of equations is $\alpha'(t) = A(m)\beta(t)$ and $\beta'(t) = B(m)\alpha(t)$, from which it follows that α and β are proportional to $\exp(t\sqrt{AB})$. Therefore, the system is unstable for any such m for which $AB \geq 0$. Similarly to the case with Eq. (2), upon accomplishing the time-

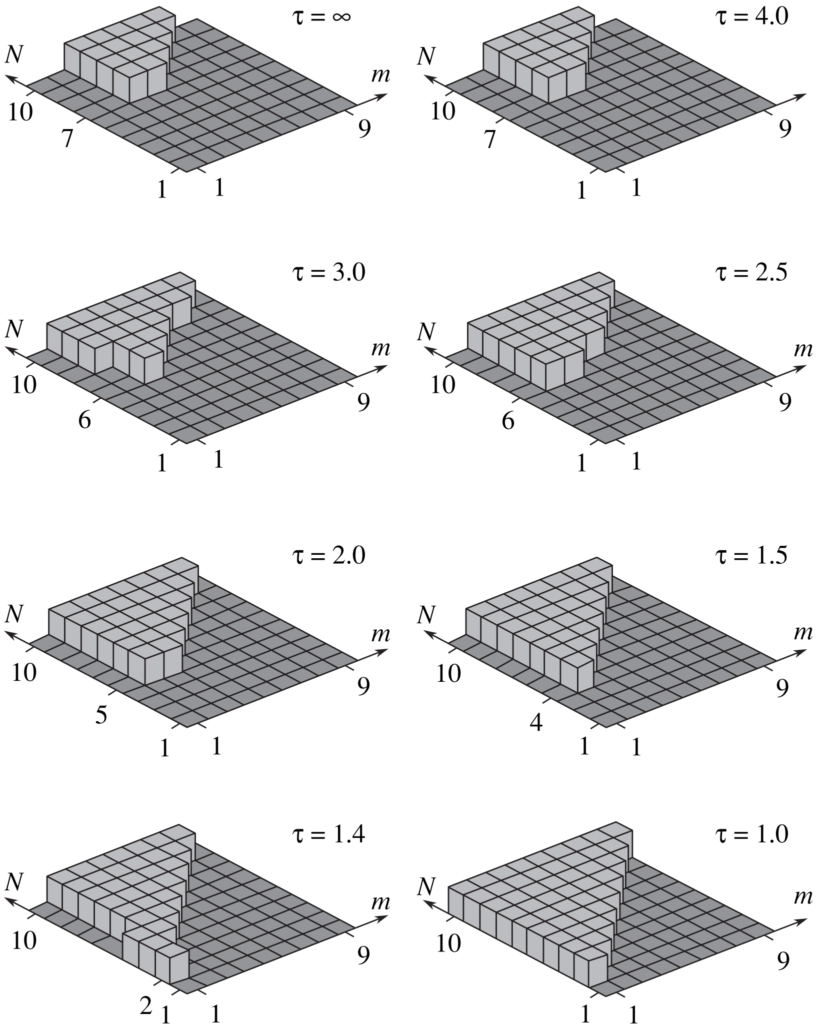

Schematic diagrams of subharmonic wavenumbers m for the unstable modes of a circular equilibrium configuration of N helical vortices calculated in the case of a constant total area of the vortex core cross sections $\varepsilon_N = 0.15\sqrt{N}$.

consuming algebraic transformations, we arrive at a relatively simple expression for the AB product:

$$\begin{aligned}
\frac{16\pi^2 a^3}{\Gamma^2}AB = \Bigg[& m(N-m)\frac{\sqrt{1+\tau^2}}{\tau} - \frac{\tau}{4}\frac{4\tau^2-3}{(\sqrt{1+\tau^2})^5} \\
& \times\left(\frac{N}{m} - C - \psi\left(-\frac{m}{N}\right)\right)\Bigg]\Bigg[m(N-m)\frac{\sqrt{1+\tau^2}}{\tau} \\
& -2(N-1)\frac{\tau^2}{1+\tau^2} + \frac{\tau}{\sqrt{1+\tau^2}} - 1 \\
& + \frac{\tau}{(\sqrt{1+\tau^2})^3}\left(\ln\left(\frac{\tau}{\varepsilon N(1+\tau^2)}\right) + \frac{5}{4}\right) \qquad (4) \\
& + \frac{\tau^3}{(\sqrt{1+\tau^2})^5}\left(\ln(N) - \left(1 - \frac{1}{4\tau^2}\right)\left(\frac{N}{m} - C - \psi\left(-\frac{m}{N}\right)\right)\right) \\
& + \frac{\tau^3}{(\sqrt{1+\tau^2})^9}\left[\left(\tau^4 - 3\tau^2 + \frac{3}{8}\right)\frac{\zeta(3)}{N^2} - \tau^4 - 3\tau^2 - 3 - \frac{1}{\tau^2}\right] \\
& + \frac{\tau^3(1+\tau^2)}{(\sqrt{1+\tau^2})^{11}}\left(t^4 - 3\tau^2 + \frac{3}{8}\right)\frac{N^2-1}{N^2}\zeta(3)\Bigg],
\end{aligned}$$

where $C = 0.577215\ldots$ is the Euler constant and $\psi(\cdot)$ is the psi function. Note that expression (4) for $\tau \longrightarrow \infty$ coincides with the product $m(N-m)[m(N-m)-2(N-1)]$ for the point vortices [2]. By analyzing expression (4) for various values of the step τ, we determined the unstable modes (see figure), which show a more realistic pattern than does the solution in [2].

Thus, we have for the first time analytically studied the problem of the stability of a circular equilibrium configuration of helical vortices.

Acknowledgments. This study was supported by the Russian Foundation for Basic Research (project no. 01-01-00899) and by the INTAS Foundation (project no. 00-00232).

REFERENCES

1. S. V. Alekseenko *et al.*, J. Fluid Mech. **382**, 195 (1999).
2. P. G. Saffman, *Vortex Dynamics* (Cambridge Univ. Press, Cambridge, 1992).
3. R. L. Ricca, J. Fluid Mech. **273**, 241 (1994).
4. J. C. Hardin, Phys. Fluids **25**, 1949 (1982).
5. V. L. Okulov, Russ. J. Eng. Thermophys. **5**, 63 (1995).
6. J. Boersma and D. H. Wood, J. Fluid Mech. **384**, 263 (1999).
7. D. H. Wood and J. Boersma, J. Fluid Mech. **447**, 149 (2001).
8. P. A. Kuibin and V. L. Okulov, Phys. Fluids **10**, 607 (1998).
9. *Handbook of Mathematical Functions*, Ed. by M. Abramowitz and I. A. Stegun (Dover, New York, 1964; Nauka, Moscow, 1979).

Translated by P. Pozdeev

Technical Physics Letters, Vol. 28, No. 12, 2002, pp. 1065–1067. Translated from Pis'ma v Zhurnal Tekhnicheskoĭ Fiziki, Vol. 28, No. 24, 2002, pp. 89–94.
Original Russian Text Copyright © 2002 by Dubinov, Tren'kin.

Electric Field Potential Distribution in a Periodic Sequence of Charged Planes in a Plasma

A. E. Dubinov and A. A. Tren'kin
Institute of Experimental Physics, Russian Federal Nuclear Center, Sarov, Russia

Received July 11, 2002

Abstract—A solution to the one-dimensional problem of the electric field potential distribution between charged planes periodically arranged in a plasma is obtained, which can serve as a model for the description of ordered structures in a dust plasma. © *2002 MAIK "Nauka/Interperiodica".*

Determining the electric field distribution in a dust plasma under conditions in which the charged particles form a periodic structure is of considerable interest. At first glance, this task can be simply solved, since the field distribution around each point charge in a plasma is known [1–3]. However, such a plasma is a system possessing an important specific feature: the dust particles can acquire a negative electric charge, which results in depletion of the electron density in the plasma. The possibility of existence of a dust plasma with reduced electron density was demonstrated by Tsytovich [4]. It should be noted that, on the scale of distances exceeding the spacing of dust particles, the condition of quasineutrality of the plasma is fulfilled since the sum of the negative charges of electrons and dust particles equals the total positive charge of ions.

The above problem is extremely difficult to solve in both two- and three-dimensional cases. A solution has been obtained using numerical methods only for a system of two dust particles [5]. However, a solution can be analytically found in a one-dimensional case wherein the particles are replaced by charged planes. A model of charged planes in a plasma was recently employed by Yakovlenko [6] to determine the field distribution. However, the system studied in [6] comprised planes positively charged due to the Richardson effect and gas ionized by emitted electrons, which resulted in an excess electron density. A system of positively charged planes was also considered in [7].

In a recent experiment [8], we experimentally measured the force of attraction between two planes occurring in a glow discharge plasma. It was found that the planes in the plasma were negatively charged. This result indicates that the problem is not only of basic interest but also of practical value.

Consider a periodic sequence of charged planes in a thermodynamically equilibrium plasma with a given temperature T. Denoting the system period by L and the electron and ion densities by n_e and n_i, respectively, we can write the condition of quasineutrality as

$$\int\limits_{mL-\frac{L}{2}}^{mL+\frac{L}{2}} e(n_\mathrm{e}-n_\mathrm{i})dz+\sigma = 0, \tag{1}$$

where σ is the surface charge density in the plane, $e = -|e|$ is the electron charge, and $m = 0, \pm1, \pm2, \ldots$ are integers. This equation is conveniently rewritten in terms of the electron and ion densities averaged over the system period:

$$e\langle n_\mathrm{e}\rangle L - e\langle n_\mathrm{i}\rangle L+\sigma = 0. \tag{2}$$

The electric field potential distribution in this system can be determined from the one-dimensional Poisson equation

$$\frac{d^2\varphi}{dz^2} = -4\pi e[n_\mathrm{e}-n_\mathrm{i}-L(\langle n_\mathrm{e}\rangle-\langle n_\mathrm{i}\rangle)\delta(z-mL)] \tag{3}$$

with the boundary conditions

$$E = -\frac{d\varphi}{dz}\bigg|_{z=mL} = 2\pi\sigma = -2\pi eL(\langle n_\mathrm{e}\rangle-\langle n_\mathrm{i}\rangle); \tag{4}$$

$$E = -\frac{d\varphi}{dz}\bigg|_{z=mL+\frac{L}{2}} = 0, \tag{5}$$

where $\delta(\ldots)$ is the Dirac delta function. The second boundary condition reflects the symmetry of the system studied.

Assuming that the electron and ion densities obey the Boltzmann distribution, we obtain the approximate relations

$$n_\mathrm{i,\,e} = n^0_\mathrm{i,\,e}\exp\left(\pm\frac{e\varphi}{kT}\right)\approx n^0_\mathrm{i,\,e}\left(1\pm\frac{e\varphi}{kT}\right), \tag{6}$$

where k is the Boltzmann constant. With allowance

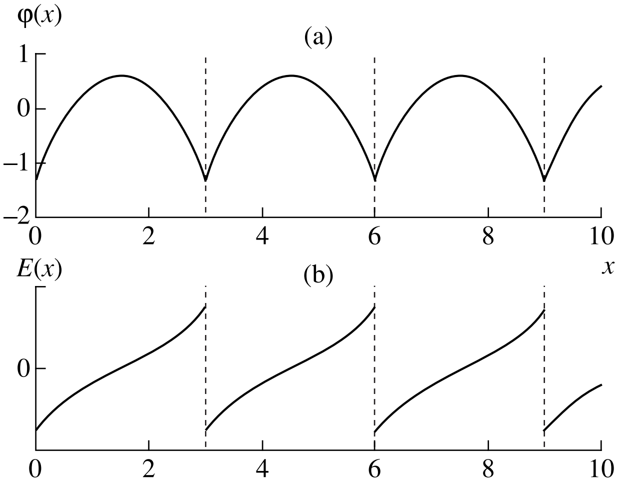

Figure.

made for this, Eq. (3) can be written as

$$\frac{d^2\varphi}{dz^2} = \frac{\varphi}{\lambda_\mathrm{D}^2} + f(z), \tag{7}$$

where

$$\lambda_\mathrm{D} = \sqrt{\frac{kT}{4\pi e^2(n_\mathrm{e}^0 + n_\mathrm{i}^0)}}$$

is the Debye screening radius and

$$f(z) = 4\pi e(n_\mathrm{i}^0 - n_\mathrm{e}^0) + 4\pi eL(\langle n_\mathrm{e}\rangle - \langle n_\mathrm{i}\rangle)\delta(z - mL).$$

A solution to this boundary-value problem including an inhomogeneous differential equation can be represented as a sum of the general solution of the corresponding homogeneous equation (φ_hom) and a partial solution of the inhomogeneous equation (φ_inhom):

$$\varphi = \varphi_\mathrm{hom} + \varphi_\mathrm{inhom}. \tag{8}$$

The well-known general solution represents a sum of two exponents,

$$\varphi_\mathrm{hom} = c_1\exp\left(\frac{z}{\lambda_\mathrm{D}}\right) + c_2\exp\left(-\frac{z}{\lambda_\mathrm{D}}\right), \tag{9}$$

where c_1 and c_2 are the integration constants. A partial solution can be represented as the integral

$$\varphi_\mathrm{inhom} = \int_{mL}^{z} G(z, z')f(z')dz', \tag{10}$$

with the Green function

$$G(z, z') = \frac{\lambda D}{2}\left[\exp\left(\frac{z - z'}{\lambda_\mathrm{D}}\right) - \exp\left(-\frac{z - z'}{\lambda_\mathrm{D}}\right)\right]. \tag{11}$$

In accomplishing the integration in Eq. (10), we obtain

$$\varphi_\mathrm{inhom} = 4\pi e\lambda_\mathrm{D}\left\{\lambda_\mathrm{D}(n_\mathrm{i}^0 - n_\mathrm{e}^0)\left[\cosh\left(\frac{z - mL}{\lambda_\mathrm{D}}\right) - 1\right]\right. \tag{12}$$
$$\left. - L(\langle n_\mathrm{i}\rangle - \langle n_\mathrm{e}\rangle)\sinh\left(\frac{z - mL}{\lambda_\mathrm{D}}\right)\right\}.$$

Now, we have to determine the integration constants c_1 and c_2 such that solution (8) will satisfy boundary conditions (4) and (5). This task reduces to solving two algebraic equations for c_1 and c_2, which eventually yields

$$c_{1,2} = \pi e\lambda_\mathrm{D}^2\frac{\exp\left(\mp\frac{mL}{\lambda_\mathrm{D}}\right)}{\sinh\left(\frac{L}{2\lambda_\mathrm{D}}\right)}\left\{2\left[\frac{L}{\lambda_\mathrm{D}}(\langle n_\mathrm{i}\rangle - \langle n_\mathrm{e}\rangle)\cosh\left(\frac{L}{2\lambda_\mathrm{D}}\right)\right.\right. \tag{13}$$
$$\left.\left. - (n_\mathrm{i}^0 - n_\mathrm{e}^0)\sinh\left(\frac{L}{2\lambda_\mathrm{D}}\right)\right] - \frac{L}{\lambda_\mathrm{D}}(\langle n_\mathrm{i}\rangle - \langle n_\mathrm{e}\rangle)\exp\left(\mp\frac{L}{2\lambda_\mathrm{D}}\right)\right\}.$$

Thus, expressions (9), (12), and (13) present a solution to the problem under consideration. The shape of the solution can be illustrated numerically. Let us introduce the dimensionless quantities

$$\eta = \frac{n_\mathrm{i}^0 - n_\mathrm{e}^0}{n_\mathrm{e}}, \quad x = \frac{z}{\lambda_\mathrm{D}}, \quad \delta = \frac{L}{\lambda_\mathrm{D}}$$

and assume that the electron and ion densities do not significantly deviate from their average values over the period $n_{\mathrm{e,\,i}}^0 \approx \langle n_{\mathrm{e,\,i}}\rangle$. Then, the above solution acquires the following form, which can be conveniently plotted:

$$\varphi(x) = 2\pi e\lambda_\mathrm{D}^2 n_\mathrm{e}\eta\left[2\delta\cosh(x - m\delta)\coth(\delta/2)\right.$$
$$\left. - \delta\frac{\cosh(x - \delta(m + 1/2))}{\sinh(\delta/2)} - 2(1 + \delta\sinh(x - m\delta))\right].$$

Typical plots showing the spatial variation of the potential and strength of the electric field in the periodic structure studied are presented in the figure.

In concluding, it should be noted that, although we have considered the simplest case of thermodynamic equilibrium, the solution can be readily generalized to the case of $T_\mathrm{e} \neq T_\mathrm{i}$, which is more typical of experimental conditions. This is achieved through using the following expression for the Debye screening radius:

$$\lambda_\mathrm{D} = \sqrt{\frac{kT_\mathrm{e}T_\mathrm{i}}{4\pi e^2(n_\mathrm{e}^0 T_\mathrm{i} + n_\mathrm{i}^0 T_\mathrm{e})}}. \tag{14}$$

Acknowledgments. One of the authors (A.E.D.) gratefully acknowledges the support of the NWO (grant no. 0.47-008-013).

REFERENCES

1. C. Lin and X.-L. Zhang, J. Phys. Soc. Jpn. **64** (10), 3767 (1995).
2. B. K. Shivamoggi, J. Math. Phys. **37** (1), 254 (1996).
3. S. K. Das, M. S. Janaki, and B. Dasgupta, J. Math. Phys. **38** (11), 5707 (1997).
4. V. N. Tsytovich, Usp. Fiz. Nauk **167** (1), 57 (1997) [Phys. Usp. **40**, 53 (1997)].
5. S. J. Choi and M. J. Kushner, J. Appl. Phys. **75** (1), 3351 (1994).
6. S. I. Yakovlenko, Pis'ma Zh. Tekh. Fiz. **27** (9), 83 (2001) [Tech. Phys. Lett. **27**, 389 (2001)].
7. K. V. Chukbar, Fiz. Plazmy **26** (5), 455 (2000) [Plasma Phys. Rep. **26**, 424 (2000)].
8. A. E. Dubinov, V. S. Zhdanov, A. M. Ignatov, *et al.*, Pis'ma Zh. Tekh. Fiz. **25** (13), 73 (1999) [Tech. Phys. Lett. **25**, 538 (1999)].

Translated by P. Pozdeev

Technical Physics Letters, Vol. 28, No. 12, 2002, pp. 971–974. Translated from Pis'ma v Zhurnal Tekhnicheskoĭ Fiziki, Vol. 28, No. 23, 2002, pp. 1–8.

A Laser Operating on the Interband Transitions in Quantum Wells with Coherent Electron Transport

É. A. Gel'vich, E. I. Golant, and A. B. Pashkovskiĭ

"ISTOK" State Unitary Enterprise, Fryazino, Moscow oblast, Russia

Received March 12, 2002

Abstract—A new approach to the creation of a quantum cascade laser is suggested, which employs interband transitions in quantum wells with a coherent electron transport. The coherent electron transport is studied based on the simplest two-band Kane model, in which the interaction between states of the conduction and valence bands is described taking into account only states in the light hole subband of the valence band. © *2002 MAIK "Nauka/Interperiodica"*.

In recent years, considerable attention has been paid to the study of semiconductor heterostructures featuring coherent (collisionless) electron transport. In these structures, the average time required for electrons to leave the active region, typically comprising one or several quantum wells, is significantly smaller than the characteristic times of all processes violating the electron wave function. The study of intersubband electron transitions in such structures has allowed some new physical effects to be predicted and ways to implement these phenomena for the effective generation of electromagnetic oscillations in the terahertz range to be outlined [1–3].

First, calculations showed that structures with coherent electron transport can possess a high negative active conductivity proportional to the fourth power of the potential barrier height [1]. The high conductivity provides the conditions for lasing with a low starting current.

Second, it was established that, under the stationary coherent electron transport conditions, application of an ac electric field of even a small (compared to the quantum energy) amplitude may lead to a significant energy redistribution between the quantum confinement levels of a two-barrier structure [2]. In particular, for a structure pumped with a current of monoenergetic electrons, it was predicted that, under certain conditions, each incident electron transfers (or acquires) a field energy quantum, so that the quantum efficiency reaches 100%. Although, for a more realistic energy distribution of the pumping electrons, the maximum quantum efficiency decreases to 66% [3], this level is still unprecedentedly high.

However, the aforementioned results refer only to the electron transitions inside the conduction band of materials obeying the quadratic dispersion law. At the same time, recent progress made in molecular beam epitaxy (MBE) technology has allowed semiconductor heterostructures to be obtained in which oscillations in the IR range are generated through interband electron transitions in the quantum wells formed due to the band discontinuity at the heterojunctions between relatively narrow-bandgap InAs and GaInSb layers [4, 5].

The establishment of the conditions conductive to coherent electron transport in such structures is of interest, both from the standpoint of basic knowledge about the features of the corresponding energy band structure and from the standpoint of practical applications. It is probable that such conditions are more readily ensured for the interband transitions than for the intraband ones, because of a less intense phonon scattering and the Auger recombination suppression in the former case [4, 5].

We have studied coherent electron transport within the framework of the simplest two-band Kane model, in which the interaction between states of the conduction and valence bands is described taking into account only states in the light hole subband of the valence band. The interaction with the other (distant) subband is approximately taken into account by using a free fitting parameter to additionally provide for the possibility of matching the effective masses of electrons and holes to the experimental data.

The Bloch electron function envelope in this model is described by the Schrödinger equations for a two-component wave function [6, 7]:

$$i\hbar\frac{\partial}{\partial t}\begin{pmatrix}\psi_e\\ \psi_l\end{pmatrix} = \hat{H}_{0R}\begin{pmatrix}\psi_e\\ \psi_l\end{pmatrix} + \hat{H}(t)\begin{pmatrix}\psi_e\\ \psi_l\end{pmatrix}, \qquad (1)$$

where ψ_e and ψ_l are the corresponding wave function envelopes of the states in the conduction band and the

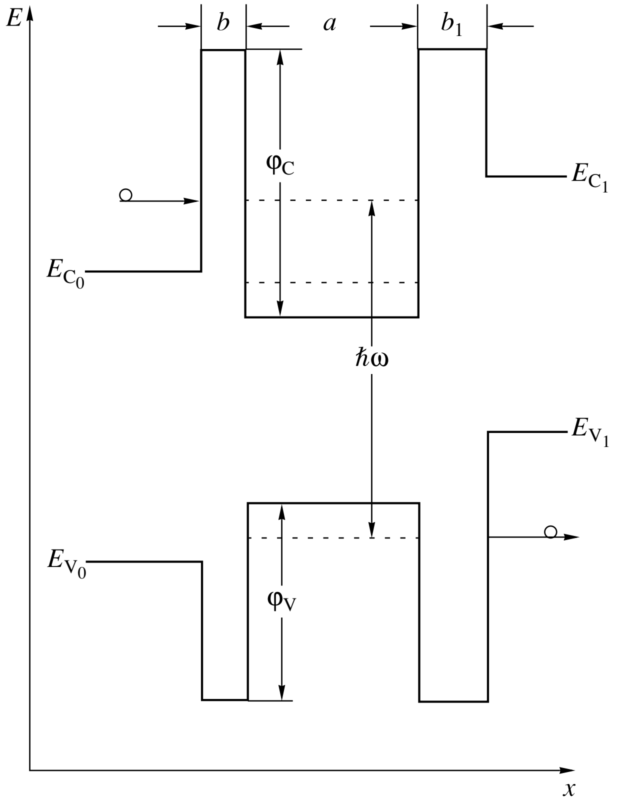

Fig. 1. Schematic diagram of the semiconductor structure studied.

light hole subband. The Hamiltonian in Eq. (1) has the following form:

$$\hat{H}_{0R} = \begin{pmatrix} E_C + \hat{k}_-\tilde{\zeta}\hat{k}_+ & kP \\ P\hat{k}_+ & E_V \end{pmatrix},$$
$$\hat{H}(t) = \begin{pmatrix} 2U(x)\cos\omega t & 0 \\ 0 & 2U(x)\cos\omega t \end{pmatrix}, \tag{2}$$

where $\hat{k}_+ = \hat{k}_x + i\hat{k}_y$, $\hat{k}_- = \hat{k}_x - i\hat{k}_y$, $\hat{k}_{x,y} = -i\nabla_{x,y}$, P is the matrix element of the momentum operator for the conduction band and the light hole subband, $2U(x)$ is the amplitude of the variable potential, $\tilde{\zeta} = \hbar^2\zeta/2m_0$, and ζ is a parameter describing the contribution of distant bands. We will consider only solutions of the above equations representing plane waves in the direction of the y axis. In this case, the operators can be represented as $\hat{k}_- = \hat{k}_x - ik_y$, $\hat{k}_+ = \hat{k}_x + ik_y$, and $\hat{k}_x = -i\nabla_x$ and the dispersion law in the absence of perturbations has the following form:

$$k^2 = k_x^2 + k_y^2 = \frac{2m_0}{\hbar}\frac{(E-E_V)(E-E_C)}{E_p+\zeta(E-E_V)} = \frac{2m}{\hbar^2}(E-E_C),$$
$$E_P = \frac{2m_0P^2}{\hbar^2}, \quad m = m_0\frac{(E-E_V)}{E_P+\zeta(E-E_V)}, \tag{3}$$

where E is the electron energy.

In the first order of perturbation theory, the wave function can be written as [1]

$$\psi = \psi_0(x)e^{-i\omega_0 t} + \psi_+(x)e^{-i(\omega_0+\omega)t} + \psi_-(x)e^{-i(\omega_0-\omega)t}, \tag{4}$$

where the first-order corrections $\psi_e^{\pm}$ are obtained from Eqs. (1) and (2) with allowance for the linear relations between $\psi_l^{\pm}$ and $\psi_e^{\pm}$ [8]:

$$\hat{k}_-\frac{\hbar^2}{2m_0}\left(\zeta + \frac{2m_0P^2}{\hbar^2(E-E_V\pm\hbar\omega)}\right)\hat{k}_+\psi_e^{\pm} - (E-E_C\pm\hbar\omega)\psi_e^{\pm}$$
$$+\frac{\hat{k}P}{E-E_V\pm\hbar\omega}\left\{\frac{U(x)P}{E-E_V}\hat{k}_+\psi_e\right\} + U(x)\psi_e = 0, \tag{5}$$

with different signs corresponding to the upward (+) and downward (–) transitions on the energy scale. Below, we will consider only the electron component of the wave function and omit the corresponding index.

Let us consider the flux of electrons with energy $\varepsilon = E - E_{C0}$ incident on an asymmetric two-barrier structure with a quantum well width a (Fig.1) to which a homogeneous high-frequency electric field $U(x) = -qFx$ is applied. Here, F is the electric field strength varying in time according to the law $2F\cos\omega t = F(e^{i\omega t} + e^{-i\omega t})$. Consider the first barrier of the heterostructure depicted in Fig. 1, φ_C being the barrier height in the conduction band and φ_V, that in the valence band. As can be shown for thin barriers ($kb \ll 1$),

$$\psi'(+0) - \frac{m(+0)}{m(-0)}\psi'(-0) \approx \left[\frac{2m(+0)}{\hbar^2}\varphi_C b\right]\psi(0) = g_C\psi(0),$$
$$E > E_C,$$
$$\psi(+0) - \psi(-0) \approx \frac{\varphi_V b}{E-E_{V0}}\psi'(-0) = g_V\psi'(-0) \tag{6}$$
$$= \frac{m(-0)}{m(+0)}g_V\psi'(+0), \quad E < E_V,$$

where the expression in square brackets (denoted by g_C) is analogous to the product of the barrier power and the effective electron mass $\frac{2m^*\alpha}{\hbar^2}$ [1].

In the resonance two-level approximation, the electron wave function for the levels with numbers N and L in the high-frequency electric field can be written as

$$\psi \approx \psi_N(x)e^{-i\omega_0 t} + \psi_L(x)e^{-i(\omega_0 - \omega)t}. \tag{7}$$

The wave function coefficients ψ_N and ψ_L inside the structure can be represented (as in the single-band model [2, 3]) in the form of a product of a constant factor and an alternating series (geometric progression),

$$1 - z + z^2 - z^3 + \ldots + (-1)^n z^n, \tag{8}$$

the sum of which in the domain of convergence ($|z| < 1$) is $1/(1 + z)$. Here,

$$z = \left(\frac{qF}{\hbar}\frac{\pi g_V g_C NR}{k}\right)^2\left(\frac{\hbar\omega}{E - E_V} - 1\right)\frac{m_- k_{1-}}{m_{1-}k_0}. \tag{9}$$

The calculation yields

$$\psi_N(x) = \begin{cases} \exp(ik_0 x) + D\exp(-ik_0 x), & x < 0, \\ A\sin(kx) + B\cos(kx), & 0 < x < a, \\ C\exp(-\kappa_1(x - a)), & x > a, \end{cases}$$

$$D = \frac{1 - z}{1 + z}, \quad A = \frac{1}{1 + z}\frac{2g_C}{k}, \quad B = \frac{2}{1 + z},$$

$$C = \frac{2}{R}\frac{(-1)^{N+1}}{1 + z},$$

$$\psi_L(x) = \frac{1}{1 + z}\begin{cases} D_-\exp(\kappa_{0-}x), & x < 0, \\ A_-\sin(k_- x) + B_-\cos(k_- x), & 0 < x < a, \\ C_-\exp(-ik_{1-}(x - a)), & x > a, \end{cases} \tag{10}$$

$$C_- \approx \frac{2qFaRg_V g_C(-1)^{N+1}}{\hbar\omega}\left(\frac{\hbar\omega}{E - E_V} - 1\right),$$

$$A_- \approx -\frac{B_-}{g_V k_-},$$

$$B_- \approx \frac{2iqFaR^2 g_V^2 g_C k_{1-}(-1)^N}{\hbar\omega}\left(\frac{\hbar\omega}{E - E_V} - 1\right),$$

$$D_- \approx \frac{A_- k_- m_{0-}}{\kappa_{0-}m_-},$$

where k is the wavevector of electrons inside the quantum well; k_0 and k_1 are the wavevectors of electrons on the left and right sides of the structure, and k_{1-}, of the electrons having passed left to right with emission of the energy quantum $\hbar\omega$; and R is the ratio of the second to first barrier thicknesses. Using expressions (10), we can determine the high-frequency conductivity of the structure studied:

$$\sigma = \frac{4\pi Lq^2R^2g_V^2g_C^2(E - \hbar\omega - E_{C1})}{\hbar\omega k_- k_{1-}(1 + z)} \times\left(1 + \frac{E - E_{C0}}{E - E_{V0}}\frac{E_{p0}}{E_{p0} + \zeta(E - E_{V0})}\right)^{-1}\left(\frac{\hbar\omega}{E - E_V} - 1\right)^2. \tag{11}$$

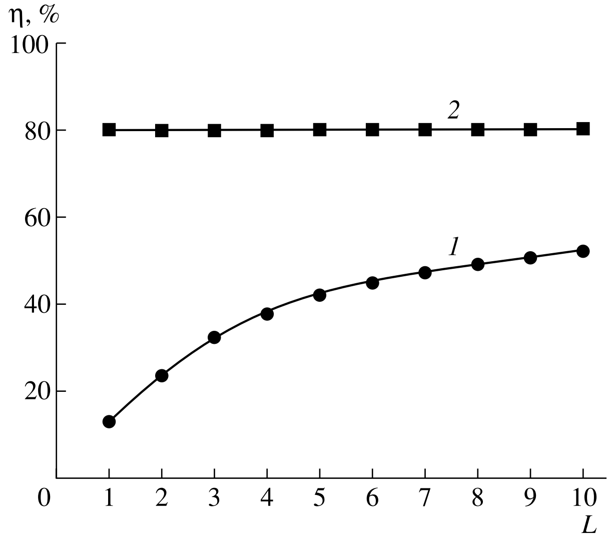

Fig. 2. Plots of the quantum efficiency versus the number of the lower resonance level to which the transition takes place in the systems with (*1*) intraband and (*2*) interband transitions.

As can be seen for $z = 1$, in this system (as well as in the case of intraband transitions [2]), electrons are no longer reflected from the two-barrier structure (D in formulas (10) becomes zero) and pass freely from the conduction band to the valence band. The field amplitude corresponding to a zero reflection ($z = 1$) can be quite small [3]. At the same time, using the fact that the energy levels between which the transitions take place are situated in different energy bands of the semiconductor structure, one can relatively independently control the level widths by changing the barrier thicknesses. In this way, it is possible to significantly increase the integral quantum efficiency of transitions in systems pumped with a flux of electrons possessing a real energy distribution. Indeed, by controlling the second barrier thickness, the level width in the valence band can be made greater than that in the conduction band (Fig. 1). According to the previous estimates [3], the integral quantum efficiency (with allowance for the fact that not all electrons can strike the structure at the center of the level) can reach up to 80%.

For comparison, Fig. 2 gives the values of maximum quantum efficiency achievable in the systems with intraband and interband transitions as a function of the level number.

REFERENCES

1. A. B. Pashkovskiĭ, Zh. Éksp. Teor. Fiz. **109** (5), 1779 (1996) [JETP **82**, 959 (1996)].
2. E. I. Golant and A. B. Pashkovskiĭ, Pis’ma Zh. Éksp. Teor. Fiz. **63** (7), 559 (1996) [JETP Lett. **63**, 590 (1996)].
3. E. I. Golant and A. B. Pashkovskiĭ, Zh. Éksp. Teor. Fiz. **112** (7), 237 (1997) [JETP **85**, 130 (1997)].
4. Rui Q. Yang, B. H. Yang, D. Zhaang, *et al.*, Appl. Phys. Lett. **71** (17), 2409 (1997).
5. J. L. Brandshaw, Rui Q. Yang, J. D. Bruno, *et al.*, Appl. Phys. Lett. **75** (16), 2362 (1999).
6. E. O. Kane, in *Semiconductors and Semimetals*, Ed. by R. K. Willardson and A. C. Beer (Academic, New York, 1966), Vol. 1, Chap. 3.
7. C. Sirtory, F. Capasso, and J. Faist, Phys. Rev. B **50** (12), 8663 (1994).
8. E. I. Golant and A. B. Pashkovskiĭ, Pis’ma Zh. Éksp. Teor. Fiz. **75** (2), 88 (2002) [JETP Lett. **75**, 83 (2002)].

Translated by P. Pozdeev

Technical Physics Letters, Vol. 28, No. 12, 2002, pp. 975–977. Translated from Pis'ma v Zhurnal Tekhnicheskoĭ Fiziki, Vol. 28, No. 23, 2002, pp. 9–13.
Original Russian Text Copyright © 2002 by Karasev, Simonov, Suzdal'tsev, Yafarov.

The Effect of Microtopography and Deposition Regime on the Field Emission Properties of Graphitelike Carbon Films

S. A. Karasev, S. V. Simonov, S. Yu. Suzdal'tsev, and R. K. Yafarov

Saratov Branch, Institute of Radio Engineering and Electronics, Russian Academy of Sciences, Saratov, Russia
e-mail: pirpc@renet.ru

Received March 13, 2002

Abstract—Technological factors controlling the formation of the microtopography of the surface of graphitelike carbon films deposited from the plasma of a microwave gas discharge in ethanol vapor are established. Parameters of the deposition regime and the surface roughness influence the electric conductivity and the field emission properties of the films obtained by this method. Using graphitelike carbon films, an emission current density of up to 0.3 A/cm^2 was obtained at an electric field strength in the gap of about 7 V/μm. © *2002 MAIK "Nauka/Interperiodica".*

At present, an urgent technological task is to obtain nanocrystalline carbon films of various structures, which could be used as field-emission cathodes for flat displays and vacuum devices in microwave electronics [1]. The good prospects in using carbon based materials as cathodes are related to their stability with respect to bombardment by the ions of residual gases present in high-voltage devices operating under the conditions of technical vacuum. Another important factor is the possibility of decreasing the electron work function in the carbon films of certain structural modifications characteristic both of diamondlike films featuring hybridization of the bonds involving valence electrons of carbon atoms and of carbon nanotubes possessing a graphitelike structure [2, 3].

In this context, our study aimed at finding technological means of obtaining graphitelike nano- and microcrystalline film materials possessing a developed surface microtopography and ensuring the desired electron emission properties.

The carbon films were obtained by deposition from ethanol vapors onto glass substrates in an electron cyclotron resonance microwave gas discharge in a setup described elsewhere [4]. The deposited film thickness was determined with the aid of a laser ellipsometer and an interference microscope. The microtopography of the sample film surface was studied with a scanning atomic force microscope (AFM). The film structure was determined using a DRON-3.0 X-ray diffractometer. The field emission current from a sample film surface was measured in a diode structure under high vacuum conditions (10^{-5} Pa) using a device in which the interelectrode distance could be controlled to within 1 μm. The anode was made of a carbon-containing composite material (MPG-6) and had a working-area diameter of 3 mm.

The sample films were deposited at an ethanol vapor pressure of 0.05 Pa and various accelerating potentials applied to the substrate holder. The substrate holder temperature was maintained at 350°C. The microwave power pumped to the plasma source was 250 W. The sample film thicknesses were 0.25–0.3 μm. The X-ray diffraction data showed that the films consisted predominantly of a fine crystalline graphite phase with an interplanar spacing of $d = 3.36$ Å [5].

Figure 1 shows typical experimental curves of the field emission current density (j) versus electric field strength (E) measured using the diode structures with graphitelike films deposited at various accelerating potentials. The anode–cathode (sample) gap width was 120 μm. As can be seen, a minimum emission threshold was reached with the films synthesized at an accelerating potential of +300 V applied to the substrate holder.

The above j–E curves were used to determine the field enhancement coefficient n of the microdiode. This coefficient was calculated as the ratio $n = E_1/E_2$ of the electric field strength E_1 at a separate (averaged) microprotrusion in the gap of the microdiode structure to the average electric field strength E_2 determined by the applied potential difference and the anode–cathode spacing neglecting the surface roughness [6].

Figure 2 shows the plots of the field enhancement coefficient n, the surface resistance R_s, and the average microprotrusion (roughness) height h versus the accelerating potential used in the carbon film synthe-

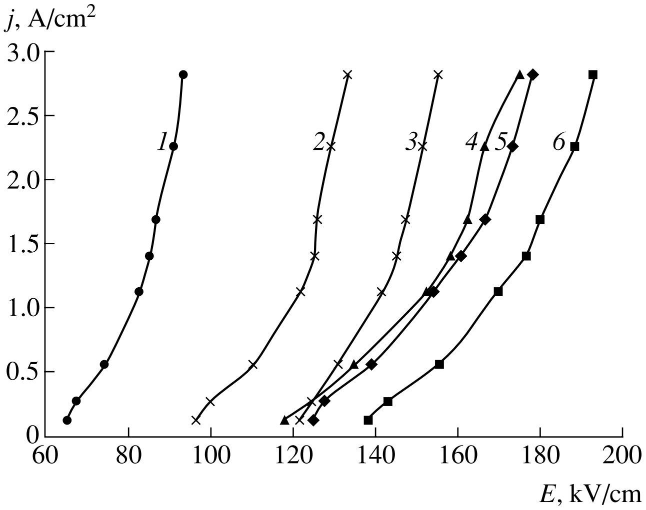

Fig. 1. Plots of the field electron emission current density versus electric field strength measured in a microdiode structure with an interelectrode gap width of 120 μm and graphitelike carbon film cathodes synthesized at various acceleration potentials (V): (*1*) +300; (*2*) +200; (*3*) +100; (*4*) –100; (*5*) –300; (*6*) –200.

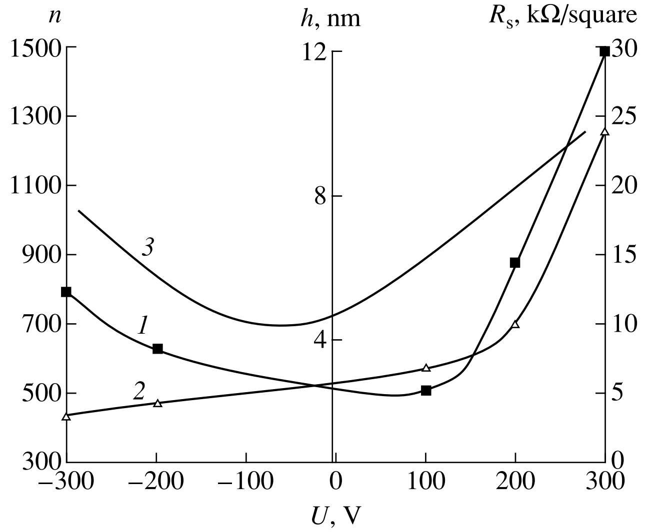

Fig. 2. Plots of (*1*) the electric field enhancement coefficient *n* microdiode structure with an interelectrode gap width of 120 μm, (*2*) surface resistance R_s, and (*3*) average microprotrusion (roughness) height *h* versus acceleration potential applied to the substrate holder during synthesis of the film.

sis. The average roughness height was determined from the AFM data (processed by a special software) for three regions of a sample film surface. As can be seen from the data in Figs. 1 and 2, the threshold electric field strength decreases and the coefficient of field enhancement at the emitter tips increases for the samples possessing more developed microtopography and a higher surface resistance. The fact that an increase in the emissivity of graphitelike carbon films can be accompanied by a decrease in their conductivity is explained as follows.

Previously [7], we demonstrated that the rate of deposition and the development of roughness of carbon films synthesized under the conditions of microwave plasma discharge in high vacuum are determined to a considerable extent by the energy and type of ions bombarding the substrate in the course of the film growth. At a small negative potential (from 0 to –200 V, Fig. 2) applied to the substrate holder, the conditions are close to those favoring the "layer growth" mechanism. These conditions are characterized by the absence of supersaturation of atomic carbon in the gas phase and by a high surface mobility of carbon atoms related to a change in the energy relief of the surface bombarded with low-energy ions of the plasma. This is indirectly confirmed by the fact that the graphitelike carbon films (possessing a higher conductivity and a lower emissivity) obtained at a negative potential on the substrate holder exhibited a "metallic luster," which is typical of single crystal graphite surface.

When the substrate holder potential is above +100 V, the substrate surface is bombarded with electrons and negative ions, including carbon ions. Owing to the more intense supply of carbon atoms and ions and the higher sticking coefficient of the latter species as compared to that of neutral atoms, the growth of the graphitelike carbon film proceeds in a more chaotic regime, as manifested by an increase in the dimensions of separate microcrystals disoriented relative to the direction of layer growth. This, together with the anisotropy of the electric conductivity of graphite, leads to an increase in the surface resistance of the carbon films.

At a sufficiently large negative accelerating potential (below –200 V), an increase in the surface roughness of the graphitelike carbon film is caused by the surface etching with ionized and atomic hydrogen supplied from the ethanol vapor plasma and by the hydrogen penetration into subsurface layers of the growing film. The etching (erosion) processes begin to develop at the sites of the initial defects on the growth surface [8], for example, at the atomic vacancies and steps. At the sites where one or several carbon bonds are broken, hydrogen more readily enters into chemical reaction to form a volatile hydrocarbon compound. As a result, carbon atoms are lost from the uppermost layer and leave roughnesses, with the edge carbon atoms becoming potential centers for field electron emission. Note that this mechanism of the formation of surface roughness in the growing carbon film does not violate the anisotropy of the electric conductivity of graphite. For this reason, the increase in emissivity of the graphitelike carbon films synthesized at high negative potentials on the substrate holder correlates only with the surface roughness height, irrespective of whether the value of the surface resistance remains constant or decreases (Fig. 2).

REFERENCES

1. A. F. Bobkov, E. V. Davydov, S. V. Zaĭtsev, *et al.*, Zh. Tekh. Fiz. **71** (6), 95 (2001) [Tech. Phys. **46**, 736 (2001)].
2. A. N. Obraztsov, Yu. I. Pavlovskiĭ, and A. P. Volkov, Zh. Tekh. Fiz. **71** (11), 89 (2001) [Tech. Phys. **46**, 1437 (2001)].
3. Y. Saito, K. Hamaguchi, K. Nata, *et al.*, Nature **389**, 555 (1997).
4. N. N. Bylinkina, S. P. Mushtakova, V. A. Oleĭnik, *et al.*, Pis'ma Zh. Tekh. Fiz. **22** (6), 43 (1996) [Tech. Phys. Lett. **22**, 245 (1996)].
5. A. Ubbelohde and F. Lewis, *Graphite and Its Crystal Compounds* (Clarendon, Oxford, 1960; Mir, Moscow, 1965).
6. M. I. Elinson and G. F. Vasil'ev, *Nonincandesced Cathodes* (Nauka, Moscow, 1974), p. 278.
7. S. Yu. Suzdal'tsev and R. K. Yafarov, Pis'ma Zh. Tekh. Fiz. **27** (15), 77 (2001) [Tech. Phys. Lett. **27**, 656 (2001)].
8. Z. Wagar, E. A. Denisov, T. N. Kompaniets, *et al.*, Zh. Tekh. Fiz. **71** (6), 133 (2001) [Tech. Phys. **46**, 773 (2001)].

Translated by P. Pozdeev

Technical Physics Letters, Vol. 28, No. 12, 2002, pp. 978–980. Translated from Pis'ma v Zhurnal Tekhnicheskoĭ Fiziki, Vol. 28, No. 23, 2002, pp. 14–18.
Original Russian Text Copyright © 2002 by Baraban, Egorov, Askinazi, Miloglyadova.

Electroluminescence of $Si–SiO_2–Si_3N_4$ Structures

A. P. Baraban, D. V. Egorov, A. Yu. Askinazi, and L. V. Miloglyadova

Institute of Physics, St. Petersburg State University,
St. Petersburg, Russia

Received March 21, 2002

Abstract—$Si–SiO_2–Si_3N_4$ heterostructures obtained by depositing silicon nitride onto a silicon substrate oxidized in dry oxygen were studied by measuring electroluminescence (EL) in the electrolyte–insulator–semiconductor system. The EL spectra display the emission bands typical of a silicon oxide layer and an intense band at 2.7 eV characteristic of the radiative relaxation of excited silylene centers. Since these centers are typical of silicon oxynitride layers, it is concluded that such a layer is formed at the boundary. © *2002 MAIK “Nauka/Interperiodica”.*

In modern microelectronic and optoelectronic technologies, multilayer dielectric films are frequently deposited onto the surface of semiconductors to form either passive of active elements of device structures. In connection with this, of considerable importance are the physicochemical processes taking place at interphase boundaries between dielectric layers both during the synthesis of an insulator–semiconductor structure and in the course of its subsequent operation. Studying these processes is also of interest from the standpoint of gaining basic knowledge on the properties of interphase boundaries, especially of those formed in disordered systems.

The aim of our experiments was to study the formation and properties of interphase boundaries formed in the course of deposition of a silicon nitride layer onto the oxide film of a $Si–SiO_2$ structure. The resulting system was studied by measuring electroluminescence in the electrolyte–insulator–semiconductor system [1].

The experiments were performed with $Si–SiO_2–Si_3N_4$ heterostructures obtained by depositing a silicon nitride layer (80- or 100-nm-thick) onto a (100)-oriented single crystal silicon substrate (KDB-10 grade wafers) oxidized in dry oxygen at 1100°C (with an oxide thickness of 40, 77, or 100 nm). The silicon nitride layers were obtained by chemical vapor deposition from a silane–ammonia mixture. The thicknesses of the dielectric layers were determined using ellipsometry.

The EL spectra were measured in the wavelength range from 250 to 800 nm using a high-transmission MDR-2 monochromator. The measurements were performed at a positive bias voltage applied to the silicon substrate, under conditions excluding the process of impact ionization in the bulk of the oxide layer. The electrolyte was a 1 N aqueous solution of Na_2SO_2. All measurements were performed at $T = 293$ K.

Figure 1 presents typical EL spectra of the $Si–SiO_2–Si_3N_4$ heterostructures. In the general case, the EL spectra of such structures represent superpositions of the spectra of SiO_2 and Si_3N_4 layers of the corresponding thicknesses measured under identical conditions (current density and electric field strength in the dielectric layers). For the luminescence excitation conditions used in this study, the EL spectrum of the SiO_2 layer of an $Si–SiO_2$ structure consists of two characteristic bands with a quantum energy of ~1.9 an 2.3 eV and a less intense emission in the UV range ($h\nu > 3$ eV) (Fig. 2) [1]. The EL spectrum from the Si_3N_4 layer of an $Si–Si_3N_4$ structure is about ten times smaller in intensity than that from an analogous silicon oxide layer and exhibits no clearly distinguished spectral features (Fig. 2). The EL spectrum of our $Si–SiO_2–Si_3N_4$ heterostructures exhibits all emission bands characteristic of the SiO_2 layer and a clearly pronounced emission band with a peak at ~2.7 eV. The intensity of the latter band increases with the thickness of both the SiO_2 and Si_3N_4 layers and exhibits a superlinear dependence on the density of current passing through the structure. The latter circumstance suggests that there is a relation between the mechanism of excitation of this band and the process of electron heating in the oxide layer. It is also necessary to note that the intensity of the EL band at 1.9 eV decreases when the intensity of emission at 2.7 eV grows.

As the silicon nitride layer of an $Si–SiO_2–Si_3N_4$ heterostructure is etched off, the band at 2.7 eV completely

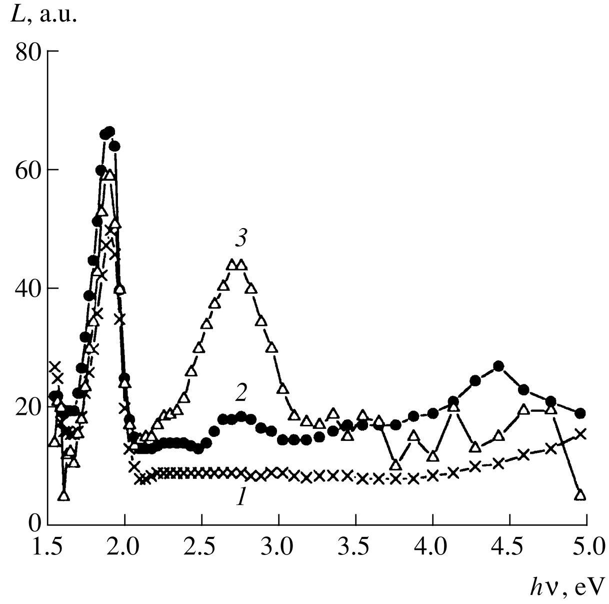

Fig. 1. The EL spectra of Si–SiO$_2$–Si$_3$N$_4$ structures with various thicknesses of the oxide and nitride layers: (*1*) SiO$_2$ (400 Å) + Si$_3$N$_4$ (800 Å); (*2*) SiO$_2$ (770 Å) + Si$_3$N$_4$ (800 Å); (*3*) SiO$_2$ (1000 Å) + Si$_3$N$_4$ (1000 Å).

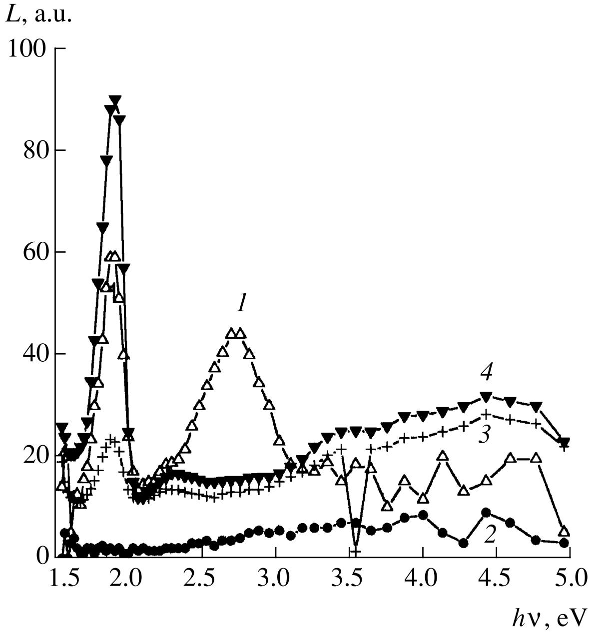

Fig. 2. A comparison of the EL spectra of various structures: (*1*) Si–SiO$_2$–Si$_3$N$_4$; (*2*) Si–Si$_3$N$_4$; (*3*) Si–SiO$_2$–Si$_3$N$_4$ after etching off the nitride layer in hydrofluoric acid; (*4*) Si–SiO$_2$.

vanishes and the resulting EL spectrum (Fig. 2, curve *3*) becomes close to the spectrum characteristic of an SiO$_2$ layer. Indeed, a comparison of the EL spectrum measured after etching to that of the Si–SiO$_2$ structure (Fig. 2, curve *4*) prepared under the same conditions as those used for the synthesis of a two-layer dielectric film shows a general similarity between the two spectra and reveals a significant decrease in intensity of the emission band at 1.9 eV in spectrum *3*.

Previously [1], we established that the EL at 1.9 eV is related to the presence of silanol groups in an SiO$_2$ layer. The concentration of these groups increases with the thickness of the SiO$_2$ layer (and, hence, with the degree of disorder in this oxide [1]). In our case, this is manifested by the intensity of the EL band at 1.9 eV in spectrum *2* being greater than that in spectrum *1* (Fig. 1).

The luminescence at 2.7 eV is characteristic of the radiative relaxation of excited (excitation energy, ~5 eV) silylene (O$_2$=Si:) centers [2] whose presence is typical of silicon oxynitride (SiN$_x$O$_y$) layers [4]. This suggests that deposition of a silicon nitride layer onto a silicon oxide surface leads to the formation of an intermediate silicon oxynitride layer at the SiO$_2$–Si$_3$N$_4$ interface. The thickness of the intermediate oxynitride layer (and, hence, the concentration of silylene centers in this layer) increases with the thicknesses of both the silicon oxide and nitride layers. In the EL excitation regime studied, the electric field strength in the silicon nitride layer reaches 6–9 MV/cm. This leads to the electron heating [3] up to energies exceeding 5 eV, which are sufficient for the excitation of silylene centers in the region of the SiO$_2$–Si$_3$N$_4$ interface.

A decrease in the intensity of the EL band at 1.9 eV (on passing from spectrum *2* to spectrum *3* in Fig. 1) indicates that the formation of silicon oxynitride is accompanied by a transformation of the uppermost SiO$_2$ layer, primarily through the formation of silanol groups. As noted above, an increase in the silicon oxide layer thickness is accompanied by a growth in the concentration of Si–OH groups in the uppermost layer of this oxide. This leads to an increase in the thickness of the silicon oxynitride layer and/or in the concentration of the silylene centers at the SiO$_2$–Si$_3$N$_4$ interface during the subsequent deposition of silicon nitride, as manifested by an increase in intensity of the EL band at 2.7 eV (Fig. 1). The same result is observed upon increasing the thickness of a silicon nitride layer (i.e., the time of silicon oxide exposure to an active medium), which increases the probability of formation of silylene centers and the intensity of the EL band at 2.7 eV. The above results indicate that the intermediate silicon oxynitride layer appears immediately during the synthesis of silicon nitride, rather than results from the current passage in the course of the EL measurements. The latter conclusion is also confirmed by the fact that the intensity of the EL band at

2.7 eV is independent of the charge passed through the structure.

Thus, an analysis of the EL spectra showed that the synthesis of a Si–SiO_2–Si_3O_4 structure is accompanied by the formation of silicon oxynitride at the boundary between the two dielectrics, which takes place predominantly through the transformation of silanol groups present in the uppermost SiO_2 layer.

Acknowledgments. This study was supported by the Russian Foundation for Basic Research, project no. 01-03-32771.

REFERENCES

1. A. P. Baraban, V. V. Bulavinov, and P. P. Konorov, *Electronics of SiO_2 Layers on Silicon* (Leningr. Gos. Univ., Leningrad, 1988).
2. L. N. Skuja, A. N. Strelttsky, and A. B. Pakovich, Solid State Commun. **50** (12), 1069 (1984).
3. D. Y. DiMaria and Y. R. Abernathey, J. Appl. Phys. **60** (5), 1727 (1986).
4. V. A. Gritsenko, *Structure and Electronic Properties of Amorphous Insulators in Silicon MIS Devices* (Nauka, Novosibirsk, 1993).

Translated by P. Pozdeev

Technical Physics Letters, Vol. 28, No. 12, 2002, pp. 981–982. Translated from Pis'ma v Zhurnal Tekhnicheskoĭ Fiziki, Vol. 28, No. 23, 2002, pp. 19–22.
Original Russian Text Copyright © 2002 by Baiburin, Volkov, Il'in, Semenov.

Tunneling Spectroscopy of Palladium–Barium Emitters

V. B. Baiburin, Yu. P. Volkov, E. M. Il'in, and S. V. Semenov
Saratov State Technical University, Saratov, Russia
e-mail: bai@sstu.saratov.su

Received June 26, 2002

Abstract—The surface of a palladium–barium cathode was studied using scanning probe microscopy techniques. Data from the tunneling spectroscopy showed the pattern of the electron work function distribution over a microscopic region on the emitter surface. This pattern is compared to the distribution of various phases in the palladium–barium alloy employed. © *2002 MAIK “Nauka/Interperiodica”.*

The reliability and working life of high-power microwave electronic tubes depend to a considerable extent on the physical properties of electron emitters (composition, structure, operating mechanism, etc.). An affective type of electron source for modern electronic devices of this type is represented by alloyed metal emitters [1]. Although such emitters have been employed for a long time, the mechanism of their operation—in particular, the formation of emission-active regions on the cathode surface—is still not completely clear. Being important from the standpoint of both basic knowledge and applications related to the further development of cathodes possessing advanced characteristics, successful research in this direction is determined by the possibility of measuring the physical parameters characterizing microscopic regions on the emitter surface at a high spatial resolution.

To our knowledge, almost no experimental data have been reported about the surface of alloyed emitters, in particular, of the palladium–barium system. The classical methods of surface analysis (such as optical metallography, chemical analysis, and X-ray diffraction), while being rather expensive, still do not allow surface relief and composition to be studied at a sufficiently high spatial resolution. We believe that an effective tool for solving this problem is offered by scanning tunneling microscopy (STM) [2], which provides for the possibility of studying the emitter surface topography and the electron work function distribution over the cathode at a high surface resolution.

Here, we report the results obtained in an investigation of the surface of palladium–barium alloy cathodes using STM. The sample surface was washed from contaminations with 96% ethyl alcohol and studied in air with a universal scanning probe microscopy setup [3] using a mechanically cut platinum–iridium alloy wire as a probing point.

Figure 1 presents a computer-processed STM image of the surface topography of a palladium–barium alloy emitter obtained for a microscopic area with dimensions 90 × 90 nm measured at a tunneling current of 1 nA. As can be seen from Fig. 1, the emitter surface has a well-developed relief and possesses a porous character, which is in agreement with the existing theoretical notions.

Figure 2 shows a typical distribution of the surface sites with various values of the electron work function over a microscopic (90 × 90 nm) area of a palladium–barium emitter surface. In this pattern, variations in the electron work function are manifested by the image color varying from white (minimum value, 2.3 eV) to

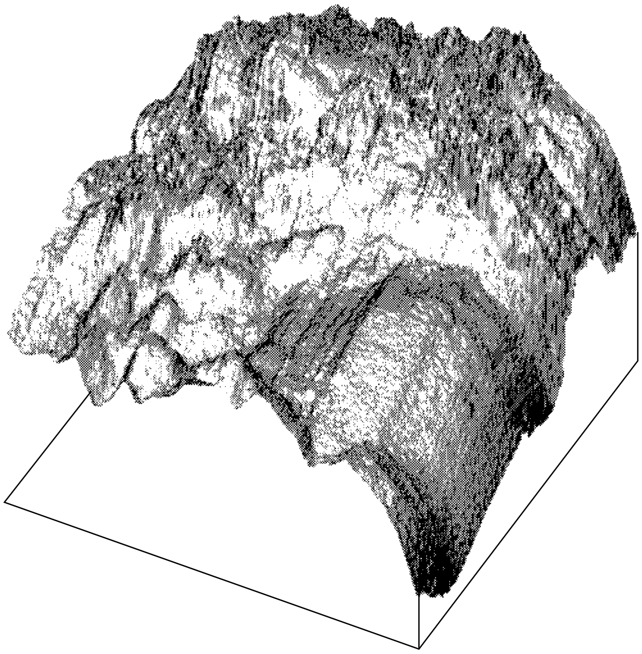

Fig. 1. An STM image of the surface topography of a 90 × 90 nm area on a palladium–barium electron emitter, showing surface roughnesses with a maximum height of 30.7 nm. The STM measurements were performed in air at a tunneling current of 1 nA and a bias voltage of 100 mV.

Fig. 2. A typical distribution of the surface sites with various values of the electron work function over a microscopic (90 × 90 nm) area of a palladium–barium emitter surface measured with tunneling spectroscopy using a tunneling gap modulation technique. White, grey, and black regions correspond to an electron work function of 2.3 eV (minimum), ~3.7 eV, and 5.2 eV (maximum), respectively.

black (maximum value, 5.2 eV). The image was obtained using tunneling spectroscopy in a tunneling gap modulation mode in the absence of a digital negative feedback (usually employed to maintain a constant tunneling current). The white regions probably correspond to barium–oxygen compounds (with an electron work function of 2.3 eV); grey regions, to an intermetallic compound (~3.7 eV); and black, to a palladium matrix with the maximum electron work function (5.2 eV). This result confirms theoretical notions regarding the island character of emissions from alloyed cathodes.

We believe that further investigations of the emitter surface topography, composition, and properties using STM could prove useful in studying the influence of various chemical and technological factors on the emissive properties of alloyed cathodes in the course of fabrication and service, with a view to obtaining devices possessing optimum characteristics.

REFERENCES

1. L. A. Ashkinazi, *Thermionic Secondary-Electron-Emission Cathodes for Electronic Vacuum and Gas-Discharge Devices*, in *Review on Electronics*, Series 1: *Microwave Engineering* (TsNII “Élektronika”, Moscow, 1992), Vol. 5.
2. G. Binnig, H. Rohrer, Ch. Gerber, *et al.*, Phys. Rev. Lett. **49** (1), 57 (1982).
3. V. B. Baiburin, Yu. P. Volkov, and N. P. Konnov, Instrum. Exp. Tech. **40** (5), 242 (1997).

Translated by P. Pozdeev

Technical Physics Letters, Vol. 28, No. 12, 2002, pp. 983–985. Translated from Pis'ma v Zhurnal Tekhnicheskoĭ Fiziki, Vol. 28, No. 23, 2002, pp. 23–29.
Original Russian Text Copyright © 2002 by Askinazi, Baraban, Dmitriev, Miloglyadova.

The Energy Position of Electrically Active Centers in the Oxide Layer of SIMOX Structures

A. Yu. Askinazi, A. P. Baraban, V. A. Dmitriev, and L. V. Miloglyadova
Institute of Physics, St. Petersburg State University, St. Petersburg, Russia

Received February 19, 2002

Abstract—Silicon-on-insulator (Si–SiO_2) structures fabricated using the SIMOX technology were studied by measuring high-frequency capacitance–voltage characteristics. Based on these data, the energy position of electrically active centers in the oxide layer of SIMOX structures is estimated. *© 2002 MAIK “Nauka/Interperiodica”.*

Heterostructures of the silicon-on-insulator (SOI) type offer a promising basis for the development of devices for use in modern microelectronics and solid-state electronics. Study of the properties of electrically active centers in these structures is of considerable interest for both basic science and applied research. An important method of obtaining SOI structures consists in the formation of buried oxide layers in the bulk of silicon by oxygen implantation, known as SIMOX technology. Despite the numerous investigations performed on these structures, there are still open questions concerning the energy position and the nature of the electrically active centers in SIMOX structures.

The purpose of this study was to determine the energy position of electrically active centers formed in the buried SiO_2 layer of SIMOX structures.

The experiments were performed with Si–SiO_2 structures prepared by implanting oxygen ions at an energy of 190 keV and a total dose of 1.8×10^{18} cm^{-2} into a silicon substrate heated to a temperature of 650°C. After ion implantation, the samples were thermally annealed for 6 h at $T = 1320$°C and then the external silicon layer was etched off to leave a silicon dioxide layer with a thickness of about 450 nm. During the electric measurements, the voltages applied to the samples (with + on Si) were sufficiently small to avoid degradation (breakdown) of the oxide film: the field strength in the oxide was E_{ox} = 1–5 MV/cm. The samples were irradiated in the near UV range ($h\nu < 6$ eV) by the light of a DRL-250 mercury lamp.

The charge state of the Si–SiO_2 structures was studied using methods based on measuring the high-frequency capacitance–voltage characteristics of the samples. The first method combines such measurements with the depth profiling technique [1] involving layer-by-layer oxide removal by etching. Based on these data, it is possible to construct a plot of the flat-bad potential V_{fb} versus the oxide layer thickness d_{ox} (Fig. 1). Another method is field cycling [1], which gives the plots of $-V_{fb}$ versus E_{ox} (Fig. 2). All these measurements were performed at a temperature of 293 K in an electrolyte–insulator–semiconductor system [1].

Previously [2], we established that the SIMOX structures studied are characterized by a positive charge density $Q^+ = (0.4 \pm 0.1) \times 10^{12}$ cm^{-2} in the oxide layer at the SiO_2–Si interface, with a centroid positioned at $X = 65 \pm 10$ nm (Fig. 1). Exposure to UV radiation in the absence of applied electric fields leads to a virtually complete neutralization of the charge (Fig. 1) [2]. The measurements performed with an electric field applied to a nonirradiated SIMOX structure (field cycling) showed evidence of stability of the charge state in the

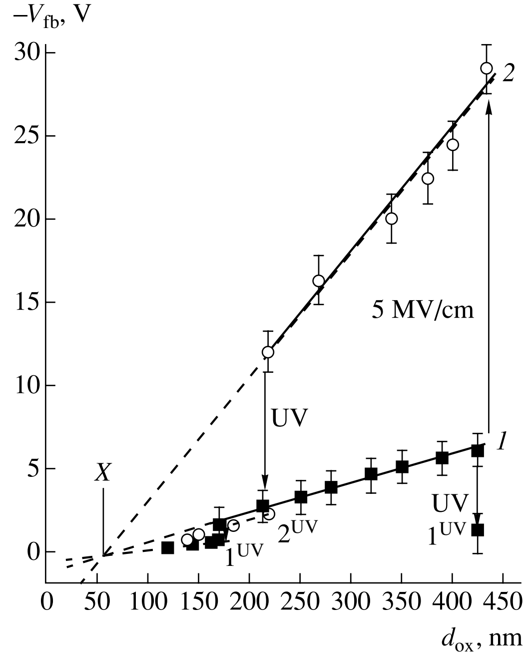

Fig. 1. Plots of the flat-band potential V_{fb} versus oxide layer thickness d_{ox} for SIMOX structures (*1*) in the initial state and (*2*) with an applied electric field.

1063-7850/02/2812-0983$22.00 © 2002 MAIK “Nauka/Interperiodica”

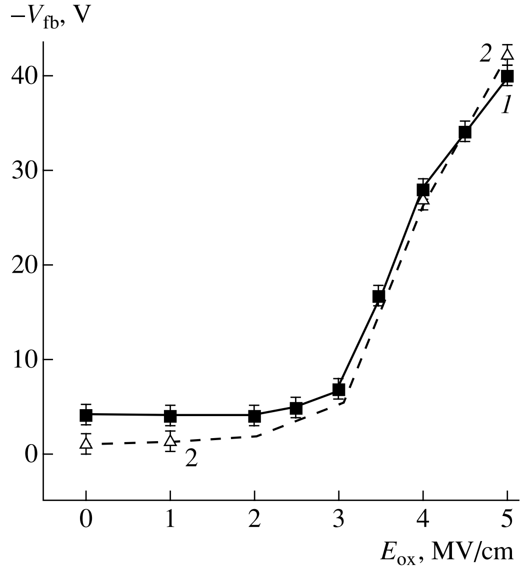

Fig. 2. Plots of the flat-band potential V_{fb} versus applied electric field strength for SIMOX structures (*1*) in the initial state and (*2*) irradiated in the near UV range.

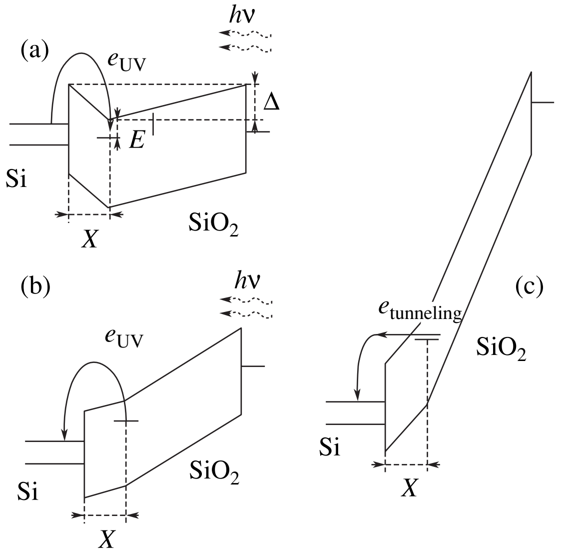

Fig. 3. Schematic diagrams illustrating the recharge of electrically active centers formed in the bulk of SiO_2 layer of SIMOX structures (see the text for explanations).

range of field strengths $E_{ox} \leq 2.5$ MV/cm (Fig. 2) [3]. As the applied electric field strength was increased further, the $-V_{fb}$ value exhibited a sharp growth starting from $E_{ox} = 3$ MV/cm (Fig. 2) [3]. This was indicative of the formation of a positive charge in the oxide layer, the centroid of this charge being also positioned at $X = 65 \pm 10$ nm (Fig. 1) [2, 3].

The UV irradiation of the SIMOX structures in the presence of an applied electric field leads to virtually complete neutralization of the positive charge generated in the oxide layer (Fig. 1) [2]. Preliminary irradiation of the samples did not significantly modify the shape of the $-V_{fb}(E_{ox})$ dependence (Fig. 2). Simultaneous exposure to UV radiation and application of a field with $E_{ox} \approx 0.2$ MV/cm did not change the charge state of the oxide. However, the same combined action of UV radiation and a field strength of $E_{ox} = 1$ MV/cm resulted in the appearance of a considerable positive charge with a centroid at $X = 65 \pm 10$ nm [2]. Subsequent exposure to UV radiation in the absence of applied electric fields leads again to a virtually complete neutralization of the charge.

Thus, irradiation in the near UV range and/or application of an electric field leads to a change in the charge state of the oxide layer of SIMOX structures. This is related to recharging of the electrically active centers (EACs), probably of a common nature, situated within the SiO_2 layer with a centroid positioned at 65 nm. Based on the experimental data obtained, we can formulate certain notions concerning the EAC recharge mechanism, the EAC energy position in the bandgap of SiO_2, and the nature of these centers.

In the course of synthesis of the Si–SiO_2 structures according to the SIMOX technology, EACs are formed in the bulk of the oxide layer at a distance of 65 nm from the Si–SiO_2 interface. In the initial state, part of these centers occurs in the neutral state (N^0), while the other centers are positively charged (N^+). The positive charge present in the bulk of the SiO_2 layer creates an electric field. This field produces spatial distortion of the energy bands of SiO_2, which is manifested by the appearance of a potential well for electrons in the conduction band. Assuming that all EACs are located in the same plane at a distance of $X = 65$ nm from the Si–SiO_2 interface, the depth Δ of the potential well in the absence of an external electric field can be estimated as

$$\Delta = \frac{\mathrm{N}^+ q^2 X}{\varepsilon_0 \varepsilon_{ox}}, \qquad (1)$$

where q is the elementary charge and $\varepsilon_0\varepsilon_{ox}$ is the permittivity of SiO_2. Substituting well-known values into this expression, we obtain $\Delta \cong 1.3$ eV.

The UV irradiation of SIMOX structures in the absence of an applied electric field leads to recharging of the EACs, whereby the positively charged centers are neutralized by the electrons photoinjected from silicon. The injected electrons drift in the electric field created by the initial positive charge until complete neutralization of the EACs takes place: $\mathrm{N}^+ + e \xrightarrow{h\nu} \mathrm{N}^0$ (Fig. 3a). The application of a relatively weak external electric field (with + on Si) prevented the drift of photoexcited electrons and resulted in the charge state remaining unchanged. The magnitude of this field can be estimated as

$$E_{ox}^{\otimes} = \frac{q\mathrm{N}^+}{\varepsilon_0 \varepsilon_{ox}}, \qquad (2)$$

which yields $E_{ox} = 0.2$ MV/cm, in agreement with the experimental results.

In the presence of an external electric field of a significantly higher strength (1 MV/cm), the UV irradiation of samples leads to devastation of the neutral EACs ($N^0 \xrightarrow{h\nu} N^+ + e$) as a result of the excitation of electrons from these centers to the conduction band of SiO_2 and their drift to the silicon substrate (Fig. 3b). This results in the formation of a considerable positive charge in the bulk of SiO_2. In this case, the energy of the neutral EACs does not exceed the UV quantum energy, which corresponds to 6 eV from the conduction band bottom of SiO_2. The fact that the positive charge in the oxide increases only in the presence of a sufficiently large applied electric field ($E_{ox} \geq 3$ MV/cm) is explained by the recharging of neutral EACs into positively charged centers ($N^0 \xrightarrow{\text{el. field}} N^+ + e$) as a result of the tunneling of electrons to the conduction band of SiO_2 and their drift to Si (Fig. 3c). It should be noted that the same electric field strength is required for the onset of tunneling injection of electrons from metal (Mg) contacts into SiO_2 in metal–insulator-semiconductor (MIS) structures [4]. These data suggest that the energy position of neutral EACs is close to the potential barrier height at the SiO_2–Mg interface ($E_t^0 \approx 2.4$ eV).

The common position of the centroids characterizing the spatial position of EACs recharged following significantly different mechanisms (optical recharge, tunneling) indicates that EACs formed in the Si–SiO_2 structures obtained using SIMOX technology are spatially localized within a sufficiently narrow region. EACs possessing the properties described above can represent unsaturated bonds of silicon atoms ($Si_3{\equiv}Si–$) at a boundary between SiO_2 and silicon clusters, the existence of which in SIMOX structures was suggested in [5]. Such an unsaturated bond represents an amphoteric center [6] possessing three metastable states differing in the number of trapped electrons, charge, and energy position. The most important subject for subsequent investigations is the reason for the appearance of a high concentration of silicon clusters at a distance of 65 nm from the SiO_2–Si interface.

REFERENCES

1. A. P. Baraban, V. V. Bulavinov, and P. P. Konorov, *Electronics of SiO_2 Layers on Silicon* (Leningr. Gos. Univ., Leningrad, 1988).
2. A. Yu. Askinazi, A. P. Baraban, V. A. Dmitriev, *et al.*, Pis'ma Zh. Tekh. Fiz. **27** (10), 57 (2001) [Tech. Phys. Lett. **27**, 422 (2001)].
3. A. Yu. Askinazi, A. P. Baraban, and L. V. Miloglyadova, Zh. Tekh. Fiz. **72** (5), 61 (2002) [Tech. Phys. **47**, 574 (2002)].
4. M. Lenzlinger and E. H. Snow, J. Appl. Phys. **40** (1), 278 (1969).
5. J. Stoemenos, A. Garcia, B. Aspar, and J. Margail, J. Electrochem. Soc. **142** (4), 1248 (1995).
6. C. T. White and K. L. Ngai, J. Vac. Sci. Technol. **16** (5), 1412 (1979).

Translated by P. Pozdeev

Technical Physics Letters, Vol. 28, No. 12, 2002, pp. 986–987. Translated from Pis'ma v Zhurnal Tekhnicheskoĭ Fiziki, Vol. 28, No. 23, 2002, pp. 30–33.
Original Russian Text Copyright © 2002 by Koshcheev.

Quasi-Stationary Distribution of Relativistic Particles in a Bent Crystal

V. P. Koshcheev
Surgut State University, Surgut, Russia
e-mail: koscheev@surgu.wsnet.ru

Received June 21, 2002

Abstract—It is shown that a quasi-stationary distribution of the transverse energies of relativistic particles (protons) moving in a bent crystal has a characteristic width of less than a few thousandths of an electron-volt. *© 2002 MAIK “Nauka/Interperiodica”.*

The rotation and cooling of beams of relativistic particles moving in bent crystals were predicted by Tsyganov [1]. According to the theory describing the bulk trapping of relativistic particles into the channeled mode [2], the discrete character of the atomic plane potential in a bent crystal explains the fact that the elastic energy losses for the transverse motion of channeled particles exceed the inelastic losses for the same motion by a factor of 10^7.

The motion of fast charged particles in bent planar channels of a crystal can be described using the Fokker–Planck equation [3]. As constructed using a stochastic equation of evolution of the transverse energy of particles constructed previously [4, 5], the Fokker–Planck equation can be represented as follows:

$$\frac{\partial f}{\partial t} = -\frac{\partial[A(\varepsilon)f]}{\partial\varepsilon} + \frac{1}{2}\frac{\partial^2[B(\varepsilon)f]}{\partial\varepsilon^2}, \qquad (1)$$

where $f = f(\varepsilon, t)$ is the density of the flux of channeled particles in the space of transverse energies.

The coefficients of the drift and diffusion of channeled particles in the transverse energy space are given by the formulas

$$A(\varepsilon) = -\frac{2pv}{RT(\varepsilon)}[x_2(\varepsilon) - x_1(\varepsilon)] + \frac{1}{4}\frac{\partial B(\varepsilon)}{\partial\varepsilon},$$

$$B(\varepsilon) \simeq \frac{4(x_2(\varepsilon) - x_1(\varepsilon))}{T^2(\varepsilon)}\int\limits_{x_1(\varepsilon)}^{x_2(\varepsilon)} D(x)dx,$$

where $T(\varepsilon)$ is the period of oscillations for a particle moving in the planar channel, $D(x)$ is the diffusion coefficient of the channeled particles, and $x_{1,2}$ are the reversal points of the classical trajectory of the channeled particle, which can be determined from the equation $U_{eff}(x_{1,2}) = \varepsilon$. Here, U_{eff} is the effective potential of a planar channel in the bent crystal and has the following form:

$$U_{eff}(x) = \bar{U}(x) - \frac{pvx}{R},$$

where $E = pv$ is the initial particle energy, R is the radius of crystal bending, $y = s\cos\phi$, $z = s\sin\phi$, ϕ is an angle in the *YOZ* plane (which is far from the principal crystallographic directions), $s \simeq vt$ is the depth of channeled particle penetration into the crystal, and $\bar{U}(x)$ is the continuous potential of the planar crystal channel averaged over thermal oscillations.

A solution to Eq. (1) will be found in the approximation adopting a harmonic potential of the planar channel, a constant crystal bending radius, and a constant atomic electron density. First, let us consider a purely dynamic problem in which the diffusion coefficient is zero. By direct substitution, it is easy to check that the function

$$\bar{f}(\varepsilon, t) = \left[\frac{1}{4(\varepsilon + \varepsilon_*)V_{\max}} \times \left(1 + \frac{\varepsilon_*}{\left(\sqrt{\varepsilon + \varepsilon_*} + (4t/T)\sqrt{\varepsilon_*}\right)^2 - \varepsilon_*}\right)\right]^{1/2} \qquad (2)$$

is a solution to Eq. (1) with $B(\varepsilon) = 0$ and the initial condition

$$\bar{f}(\varepsilon, t = 0) = [4\varepsilon V_{\max}]^{-1/2}, \qquad (3)$$

corresponding to a beam of particles incident onto the crystal surface with a zero disorientation angle. In expression (2), $\varepsilon_* = (R_c/R)^2 V_{\max}$, $V_{\max}$ is the maximum potential of a separate atomic plane and R_c is the critical crystal bending radius [1]. It can also be readily seen that, after several periods of oscillations in the planar

1063-7850/02/2812-0986$22.00 © 2002 MAIK “Nauka/Interperiodica”

channel (for $4t/T \gg 1$), the distribution function (2) ceases to depend on time:

$$\bar{f}(\varepsilon, t \gg T) = [4(\varepsilon + \varepsilon_*)V_{\max}]^{-1/2}. \qquad (4)$$

Thus, as a result of elastic losses of the transverse energy caused by a discrete atomic plane potential in the bent crystal, the transverse energy distribution profile shifts from $\varepsilon = 0$ in the unbent part of the crystal to $\varepsilon = -\varepsilon_*$ in the bent part. When the crystal is bent, the potential well bottom shifts away from the middle of the planar channel and decreases by $-\varepsilon_*$.

A stationary solution to Eq. (1), which is more correctly called quasi-stationary because the total energy of a channeled particle decreases due to the inelastic energy losses, has the following form:

$$f_s(\varepsilon) = [4(\varepsilon + \varepsilon_*)\varepsilon_{1/e}]^{-1/2}\exp\left(-\sqrt{(\varepsilon + \varepsilon_*)/\varepsilon_{1/e}}\right). \qquad (5)$$

The characteristic width of the distribution function (5) is

$$\varepsilon_{1/e} \simeq \frac{8[\mathrm{Re}^4 NZ_2 \ln(Ea/\hbar c)]^2}{(pv)^3}, \qquad (6)$$

where NZ_2 is the average density of atomic electrons, a is the screening radius, $\hbar$ is the Planck constant, and c is the speed of light in vacuum.

Formula (6) yields the following estimate for relativistic protons in a silicon crystal:

$$\varepsilon_{1/e} \simeq \frac{1}{pv}\left(\frac{R}{R_c}\right)^2 \times 10^{-6},$$

where the initial particle energy $[pv]$ = GeV and the distribution function width $[\varepsilon_{1/e}]$ = eV are expressed in units of the total energy (GeV) and the transverse energy (eV), respectively. As can be readily seen, relativistic protons with total energies in a broad range from 1 to 1000 GeV are localized in a narrow vicinity of the potential minimum of a bent planar channel in a silicon crystal: the characteristic distribution width exhibits a record value of below a few thousandths of an electronvolt.

A comparison of expressions (4) and (5) shows that an allowance for multiple scattering leads to a paradoxical result: the distribution of channeled particles with respect to the transverse energy narrows rather than broadens. As is known (see, e.g., [6]), an analogous situation takes place in storage rings; however, the mechanism of the transverse cooling of relativistic ions in that case is somewhat different. Direct verification of the theoretical predictions can be performed by treating the experimental data reported by Andreev *et al.* [7] using the method developed by Bak *et al.* [8].

In the latter experiment [8], a crystal was bent in a three-point loading mode and the depth of the particle penetration into the crystal varied in proportion to the bending radius [9]. No quasi-stationary state can be expected in this case, which is in agreement with the experimental results obtained (see [8, Fig. 17]). In the former experiment [7], a crystal was bent using a device ensuring a constant bending radius, which should lead, as demonstrated above, to a quasi-stationary distribution of particles with respect to transverse energy.

The proposed theory is indirectly confirmed by the results of experiments reported in [10], where no explanation was given to the absence of dechanneling in the part of the crystal (bent in a four-point loading mode) with a constant bending radius.

REFERENCES

1. E. N. Tsyganov, Preprint Fermilab, TM, 682 (Batavia, 1976).
2. V. P. Koshcheev, Pis'ma Zh. Tekh. Fiz. **28** (8), 24 (2002) [Tech. Phys. Lett. **28**, 318 (2002)].
3. V. P. Koshcheev, Izv. Vyssh. Uchebn. Zaved., Fiz., No. 1, 88 (2002).
4. V. P. Koshcheev, Pis'ma Zh. Tekh. Fiz. **27** (18), 61 (2001) [Tech. Phys. Lett. **27**, 784 (2001)].
5. V. P. Koshcheev, Pis'ma Zh. Tekh. Fiz. **28** (5), 1 (2002) [Tech. Phys. Lett. **28**, 171 (2002)].
6. H. Danared, A. Kallberg, K.-G. Rensfelt, and A. Simonson, Phys. Rev. Lett. **88** (17), 174801 (2002).
7. V. A. Andreev, V. V. Baublis, E. A. Damaskinskiĭ, *et al.*, Pis'ma Zh. Éksp. Teor. Fiz. **36** (9), 340 (1982) [JETP Lett. **36**, 415 (1982)].
8. J. F. Bak, P. R. Jensen, H. Matsboll, *et al.*, Nucl. Phys. B **242**, 1 (1984).
9. J. A. Ellison, S. I. Baker, R. A. Carrigan, Jr., *et al.*, Nucl. Instrum. Methods Phys. Res. B **230**, 9 (1984).
10. W. M. Gibson, L. I. Kim, M. Pisharody, *et al.*, Nucl. Instrum. Methods Phys. Res. B **230**, 54 (1984).

Translated by P. Pozdeev

Technical Physics Letters, Vol. 28, No. 12, 2002, pp. 988–990. Translated from Pis’ma v Zhurnal Tekhnicheskoĭ Fiziki, Vol. 28, No. 23, 2002, pp. 34–38.
Original Russian Text Copyright © 2002 by Ivlev, Gatskevich.

The Dynamics of Annealing of Ion-Amorphized Silicon by Nanosecond Pulses of Excimer Laser UV Radiation

G. D. Ivlev and E. I. Gatskevich

Institute of Electronics, National Academy of Sciences of Belarus, Minsk, Belarus
e-mail: ivlev@inel.bas-net.by

Received June 25, 2002

Abstract—Phase transitions in ion-amorphized silicon annealed by nanosecond UV radiation pulses of an ArF excimer laser were studied by time-resolved reflectivity measurements at $\lambda = 633$ nm. It was established that epitaxial crystallization of a melted layer of silicon takes place at a laser energy density of $W > 0.8$ J/cm^2. At 0.2 J/cm$^2 < W < 0.7$ J/cm^2, silicon exhibits amorphization in the course of solidification, the initial and final amorphous phases being different. This amorphization of solidifying silicon is accompanied by the nucleation of separate crystallization centers. The presence of such centers changes the kinetics of phase transformations in the course of repeated laser action, leading to the formation of a polycrystalline structure, and provides for the possibility of obtaining intermediate crystallization states of Si in a sequence of laser-induced phase transitions. © *2002 MAIK “Nauka/Interperiodica”.*

The modification and crystallization of amorphous silicon (a-Si) under the action of nanosecond UV radiation pulses of an excimer laser is an attractive method for use in the technology of thin-film solar cells and transistors in active liquid crystal display matrices [1, 2]. In this context, it is important to study the phase transitions taking place in a-Si under the action of such laser radiation.

Previously [3], we studied the dynamics of ArF excimer laser annealing of thin hydrogenated a-Si films prepared by silane decomposition in glow discharge plasma. It was established that crystallization of the ion-amorphized silicon requires at least two laser pulses with an energy density above the melting threshold W_{ma}. After a single laser pulse, solidification of a liquid phase (l-Si) leads to the formation of a new amorphous phase (a$_2$-Si), with the structure and electric properties being different from those of the initial (a$_1$-Si) amorphous phase. The purpose of this study was to elucidate the dynamics of laser-induced transformations taking place in ion-amorphized silicon layers under analogous experimental conditions.

The experiments were performed on (111)-oriented B-doped single crystal silicon wafers implanted with 75-keV P^+ ions to a total dose of 2×10^{15} cm^{-2}, which produces amorphization of the initial crystalline material (c-Si) to a depth of ~0.1 μm. The a-Si samples were annealed by exposure to pulsed radiation from an ArF excimer laser (FMG-100) with a pulse duration (full width at half maximum) of ~10 ns. The absorbed laser energy density W was controlled with the aid of a focusing lens moved along the laser beam axis. The irradiated spot size was determined by a diaphragm of 0.5 mm in diameter spaced from the sample by a distance exceeding the focal length. The sample was probed by a He–Ne laser beam ($\lambda = 633$ nm) focused into an ~0.05 mm spot at the center of the region irradiated by the excimer laser. The probing laser beam, incident at an angle of 30°, was polarized in the incidence plane. The reflected beam was detected by a silicon photodiode, the output signal of which was transmitted to a TS-8123 storage oscillograph connected with a personal computer. The characteristic transient time of the signal detection channel was about 4 ns.

Under the experimental conditions studied, the melting threshold energy density was $W_{ma} \sim 0.16$ J/cm^2, the epitaxial crystallization threshold of a melted silicon layer was $W_{ec} \sim 0.75$ J/cm^2, and the laser ablation threshold was 2.3–2.4 J/cm^2. Laser action at an energy density in the interval $W_{ma} < W < W_{ec}$ does not lead to crystallization of the amorphous silicon layer but induces the phase transitions a$_1$-Si $\longrightarrow$ l-Si $\longrightarrow$ a$_2$-Si taking place at a temperature (T_{ma}) which is about 200 K below the equilibrium melting point T_{mc} of crystalline silicon (c-Si), that is, under the conditions of significantly supercooled l-Si [4, 5]. The formation of l-Si is manifested by an increase in the coefficient of reflection (R) of the probing radiation (see figure), which is restored to the initial level (~33%) after solidification.

When the laser radiation energy density W is increased in the above interval, the time variation of the reflection coefficient, $R(t)$, qualitatively changes. For $W > 0.4$ J/cm^2, the final R level is attained in a nonmonotonic manner (see curves *4–6* in the figure). This behavior, which becomes more pronounced when W approaches the epitaxial threshold, is explained by the fact that the amorphous phase formation (l-Si $\longrightarrow$ a_2-Si) proceeds both from the substrate and from the surface of a melted layer, so that R drops below the initial level and exhibits a minimum. This behavior of the reflection coefficient agrees with the results of calculations and is due to interference of the probing radiation upon reflection from the a_2-Si/l-Si system with liquid–solid interfaces moving in opposite directions. After the action of a laser pulse with an energy of $W \geq 0.8$ J/cm^2, the melted layer exhibits epitaxial crystallization (see curves *7*, *8* in the figure) and the surface of the laser-irradiated zone is visually indistinguishable from that of a polished single crystal.

A difference between the a_1-Si and a_2-Si structures is confirmed by the following fact: repeated irradiation of the pre-exposed samples ($2W_{ma} < W < W_{ec}$) leads to significantly different kinetics of the phase transitions and, accordingly, to different dynamics of variation of the reflection coefficient R (see curves *10–15* in the figure). According to this, preliminary irradiation ($W = W_1 = 0.2$–0.3 J/cm^2) results in the appearance of separate crystalline nuclei (nanocrystals with probable dimensions below 5 nm) in the amorphous matrix formed due to the l-Si $\longrightarrow$ a_2-Si phase transition. Upon repeated melting of the amorphous silicon (i.e., of the a_2-Si phase) at $W = W_2$, these nanocrystals (occurring in a strongly supercooled liquid phase l_1-Si) grow to form a polycrystalline structure (pc_1-Si).

For $W \geq 2W_{ma}$, the laser action leads to melting of the pc_1-Si phase ($T_{ma} < T < T_{mc}$) followed by the formation of a secondary polycrystalline phase (l_2-Si $\longrightarrow$ pc_2-Si). As a result, the zone of laser action acquires a specific color and is characterized by lower reflectance (curves *10–15* in the figure). Additional phase transitions (l_1-Si $\longrightarrow$ pc_1-Si $\longrightarrow$ l_2-Si) lead to an intermediate decrease in intensity of the reflected probing beam (manifested by the drop in curves *10–15*), while relatively small W values lead to a slower decrease in R (manifested by the shoulder in curves *11* and *12*). As the W value increases, the minimum in R shifts toward the leading front of the pulsed response signal. For laser energies above W_{ec}, the phase transition l_1-Si $\longrightarrow$ pc_1-Si is probably suppressed as a result of the liquid-phase heating proceeding at a high rate and the decomposition of nanocrystals.

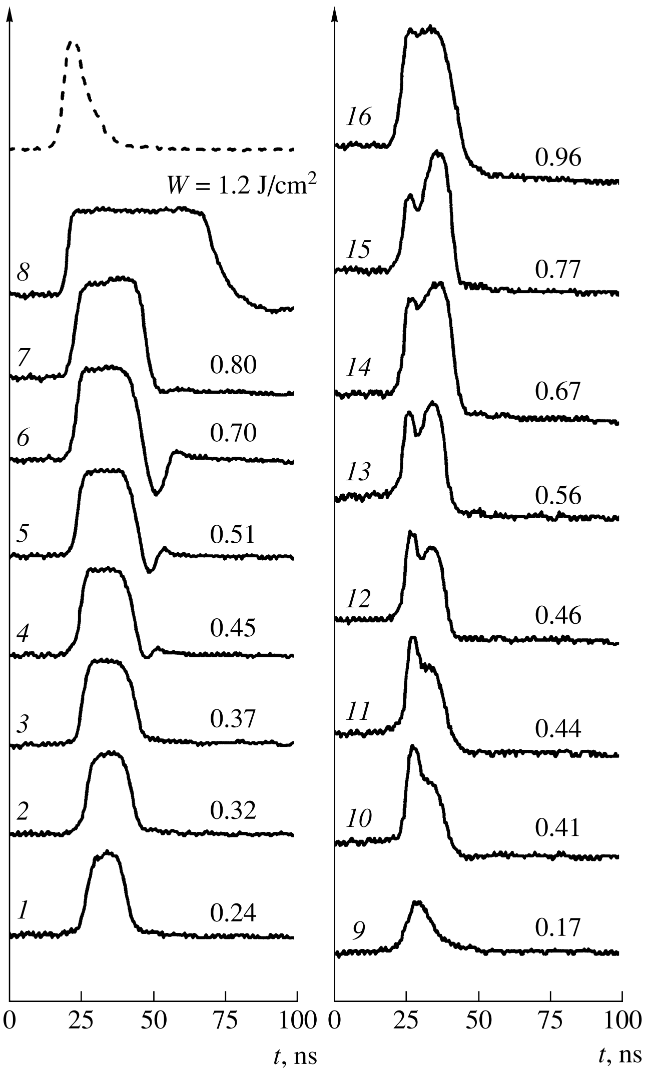

Oscillograms of the output signals of a photodetector sensing the probing radiation flux reflected from a silicon sample heated by nanosecond UV laser pulses (dashed profile) at various energy densities (see the text for explanations).

In concluding, it should be noted that the experiments performed with analogous ion-implanted silicon samples irradiated by single pulses of a ruby laser [5] also showed evidence of additional phase transitions of the l_1-Si $\longrightarrow$ pc-Si $\longrightarrow$ l_2-Si type. Here, in contrast to the situation described above, the effective nucleation of nanocrystals in the a-Si premelting stage is not suppressed due to a much lower rate of heating of the initial a-Si (pulse duration, 70–80 ns). As a result, the above phase transitions (i.e., the intermediate silicon crystallization stage with the formation of fine-crystalline pc-Si) and the subsequent melting take place not only for $W_{ma} < W < W_{ec}$ but also for laser radiation energies above the epitaxial growth threshold.

Acknowledgments. The authors are grateful to V. Cháb for kindly providing the opportunity to perform the experiments with an excimer laser.

This study was partly supported by the Belarussian Republican Foundation for Basic Research, project no. F99-184.

REFERENCES

1. C. D. Kim, R. Ishihara, and M. Matsumura, Jpn. J. Appl. Phys. **34**, 5971 (1995).
2. W. Staudt, S. Borneis, and K.-D. Pippert, Phys. Status Solidi A **166** (2), 743 (1998).
3. G. Ivlev, E. Gatskevich, V. Cháb, *et al.*, Appl. Phys. Lett. **75**, 498 (1999).
4. W. C. Sinke, A. Polman, and P. A. Stolk, in *EPM'89: Proceedings of the 3rd International Conference on Energy Pulse and Particle Beam Modification of Materials, Dresden, 1989*, Ed. by K. Hohmuth and E. Richter (Akademie-Verlag, Berlin, 1990), Vol. 13, pp. 94–99.
5. L. P. Avakyants, G. D. Ivlev, and E. D. Obraztsova, Fiz. Tverd. Tela (St. Petersburg) **34**, 3334 (1992) [Sov. Phys. Solid State **34**, 1784 (1992)].

Translated by P. Pozdeev

Technical Physics Letters, Vol. 28, No. 12, 2002, pp. 991–993. Translated from Pis'ma v Zhurnal Tekhnicheskoĭ Fiziki, Vol. 28, No. 23, 2002, pp. 39–43.
Original Russian Text Copyright © 2002 by Rodnyĭ, Mishin, Mikhrin, Potapov.

Temperature-Induced Variation of the Emission Band Intensities of an $SrAl_{12}O_{19}$:Pr Phosphor

P. A. Rodnyĭ, A. N. Mishin, S. B. Mikhrin, and A. S. Potapov
St. Petersburg State Technical University, St. Petersburg, 195251 Russia
e-mail: Rodnyi@toexph.stu.neva.ru

Received July 4, 2002

Abstract—The spectral characteristics of the X-ray-excited luminescence from an $SrAl_{12}O_{19}$:Pr phosphor featuring cascade photon emission were studied in a range of temperatures from 90 to 500 K. It is demonstrated that an important role in the energy transfer to the emission centers in $SrAl_{12}O_{19}$:Pr is played by competitive processes of the formation of V_k centers and the trapping of holes by Pr^{3+} ions. © *2002 MAIK “Nauka/Interperiodica”.*

At present, the task of improving the performance characteristics of plasma display panels is solved, in particular, through finding new effective phosphors. Good prospects in this respect are offered by compounds capable of emitting photons by the cascade mechanism [1–5]. A convenient matrix featuring cascade photon emission from Pr^{3+} ions is $SrAl_{12}O_{19}$ [1]. Praseodymium replacing strontium in the $SrAl_{12}O_{19}$ matrix weakly interacts with the nearest neighbor oxygen ions, thus ensuring high positions of the energy levels of a mixed $4f^15d$ electron configuration and providing for the possibility of radiative transitions from the $^1S_0$, $4f$ level [1, 2]. Previously, the properties of $SrAl_{12}O_{19}$:Pr phosphors were studied both experimentally [1–5] and theoretically [6]. These investigations provided detailed data on the spectra and luminescence decay times [1–4], the concentration dependence of the spectral characteristics [4, 5], the influence of nonradiative transitions on the emission properties of phosphors [1, 2], and the role of mixing of the $^1S_0$, $4f$ and $5d$ states of Pr^{3+} ions [6].

In this study, we paid special attention to the temperature-induced variations in the intensities of bands in the emission spectrum of an $SrAl_{12}O_{19}$:Pr phosphor. These temperature dependences provide new information about basic physical processes in the phosphor. These data are also of considerable practical significance because a phosphor used in a gas-discharge device can operate at temperatures above room temperature. The measurements were mostly conducted in the experimental setup described previously in [7]. The experiments were performed with polycrystalline samples of $SrAl_{12}O_{19}$:Pr, the characteristics of which were recently presented in [5].

Figure 1 shows a typical temperature variation in the intensities of the two most effective bands in the X-ray-excited luminescence spectrum of an $SrAl_{12}O_{19}$:Pr phosphor. The short-wavelength emission band with a maximum at 403 nm is assigned to the first step of the cascade photon emission ($^1S_0 \longrightarrow {}^1I_6$ transitions), and the long-wavelength band with a peak at 488 nm corresponds to the second step of this cascade process ($^3P \longrightarrow {}^3H_4$ transitions). A maximum intensity of the emission due to transitions from the $^1S_0$ level is observed at ~350 K. The entire X-ray-excited luminescence spectrum measured at this temperature is presented in Fig. 2. The inset to Fig. 2 shows the luminescence excitation spectrum of the room-temperature emission at 403 nm. Besides the aforementioned bands, the X-ray-excited luminescence spectrum displays other emission bands corresponding to transitions from the upper excited $^1S_0$ level of the Pr^{3+} ion to lower levels, including $^3F_4$ (257 nm), $^1G_4$ (276 nm), and $^1D_2$ (341 nm).

A decrease in the intensity of emission at 403 and 488 nm observed for $T > 350$ K (Fig. 1) is naturally attributed to the process of temperature quenching. An unusual feature is a sharp drop in the intensity of emission at 403 nm at temperatures below 140 K, where the decrease in the intensity of emission at 488 nm is not as pronounced. It is important to note that this significant drop in intensity of the short-wavelength band is characteristic of X-ray-excited luminescence and not observed upon direct excitation of the Pr^{3+} centers at 6 eV. The X-ray excitation produces a certain amount of electrons at the conduction band bottom and holes at the valence band top. These electrons subsequently relax to the closest $4f^15d$ states of Pr^{3+}, while the holes

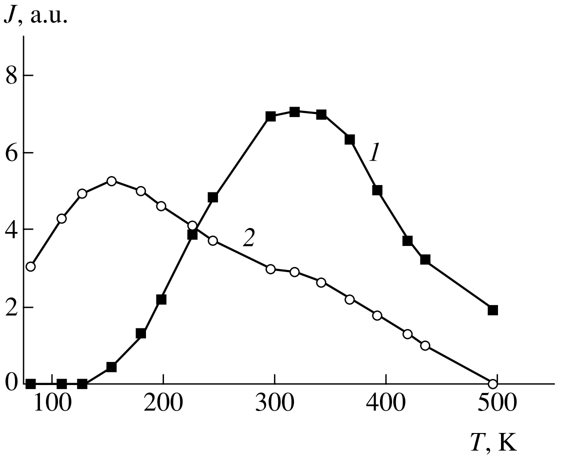

Fig. 1. Temperature dependence of the intensity of the emission bands at (*1*) 403 and (*2*) 488 nm in the X-ray-excited luminescence spectrum of an $SrAl_{12}O_{19}$:Pr phosphor (0.5% Pr).

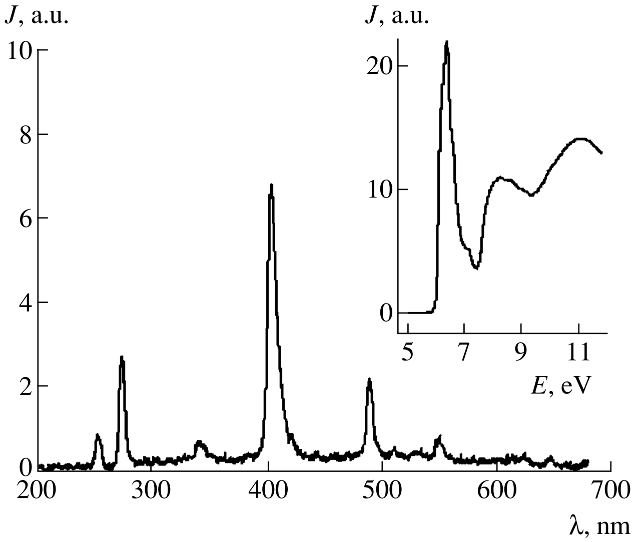

Fig. 2. The X-ray-excited luminescence spectrum of an $SrAl_{12}O_{19}$:Pr phosphor (0.5% Pr) measured at 350 K. The inset shows the room-temperature spectrum of excitation for the luminescence band at 403 nm.

are either trapped by Pr^{3+} ions or involved in the axial relaxation process [2].

The most acceptable mechanism explaining the low-temperature drop in intensity of the first step of the cascade photon emission is that involving competitive processes of the trapping of holes from the valence band by the V_k centers and Pr^{3+} ions. Having reached the valence band bottom, holes in the ionic compound participate in the axial relaxation. As a result of this process, autolocalized holes or V_k centers are formed within a time period of ~10^{-12} s. On the other hand, the recombination luminescence mechanism in activated crystals consists in the trapping of holes from the valence band by Pr^{3+} ions according to the reaction $Pr^{3+} + h \longrightarrow Pr^{4+}$, followed by the trapping of electrons from the conduction band to the excited level. At temperatures above that of delocalization of the V_k centers ($T_d \approx$ 129–140 K), holes in the relaxed states (i.e., V_k centers) migrate over the crystal and can be trapped by Pr^{3+} ions. At $T < T_d$, the V_k centers are immobile and the conversion reaction $Pr^{3+} \longrightarrow Pr^{4+}$ is low-probable, which leads to a decrease in intensity of the first step of the cascade photon emission.

Transitions from the $^3P_0$ level provide for a high radiation yield even at low temperatures due to the energy transfer from autolocalized excitons to Pr^{3+} ions. An autolocalized exciton is formed when a V_k center traps an electron from the conduction band, after which the exciton $\longrightarrow Pr^{3+}$ energy transfer takes place. The energy of the autolocalized exciton is sufficient to excite a $^3P_0$ level but not to provide for the system transition to a $^1S_0$ level. For this reason, the low-temperature spectra show predominantly $^3P_0$ luminescence or the second step of the cascade proton emission from Pr^{3+} ions. Previously, luminescence due to autolocalized excitons was observed in $SrAl_{12}O_{19}$:Pr containing less than 0.5% Pr^{3+} ions [5].

The position of a low-energy edge (at 5.92 eV or 210 nm) of the luminescence excitation spectrum corresponds to the onset of $4f \longrightarrow 5d$ transitions (see the inset to Fig. 2). The $^1S_0$ level of Pr^{3+} ions in $SrAl_{12}O_{19}$:Pr is situated at 6.77 eV (215 nm) [3]. Therefore, the room-temperature gap between the lowest level of the 5*d* configuration and the $^1S_0$ level is sufficiently small: $\Delta \approx 0.15$ eV. The excitation peak at 6.4 eV corresponds to transitions from the $^3H_4$, 4*f* state to levels of the mixed $4f^15d$ electron configuration. Effective excitation of the cascade photon emission at 6 eV is related to the $5d \longrightarrow {}^1S_0$ thermal relaxation process (see, e.g. [3]) followed by radiative transitions from the $^1S_0$ level. An increase in the quantum yield of the emission at 403 nm for $E > 7.5$ eV in the luminescence excitation spectrum is due to the onset of transitions from the valence to conduction band. Using the observed luminescence excitation spectrum, we can estimate the bandgap width of $SrAl_{12}O_{19}$ to be E_g = 7.4 eV.

Thus, the intensity of the emission band at 403 nm, as well as of the other short-wavelength emission bands related to transitions from the $^1S_0$ level of Pr^{3+} ions excited by X-ray radiation (or by any quanta with energy exceeding 7.5 eV), in the luminescence spectrum of $SrAl_{12}O_{19}$:Pr decreases with temperature. This decrease is apparently related to an increase in the efficiency of formation of V_k centers in the crystal. A certain contribution to the decrease in intensity of the short-wavelength emission from Pr^{3+} can also be due to temperature-induced variation of the energy gap between 5*d* and $^1S_0$ levels. The increase in the $\Delta(5d, {}^1S_0)$ value (due to a shortwave shift of the 5*d* levels) with decreasing temperature leads to a decrease in the probability of the $5d \longrightarrow {}^1S_0$ thermal relaxation process.

Acknowledgments. This study was supported by the Russian Foundation for Basic Research, project no. 01-02-17960.

REFERENCES

1. A. M. Srivastava and W. W. Beers, J. Lumin. **71**, 285 (1997).
2. P. A. Rodnyĭ, A. N. Mishin, and A. S. Potapov, Opt. Spektrosk. (2002) (in press).
3. S. Huang, L. Lu, W. Jia, *et al.*, Chem. Phys. Lett. **348**, 11 (2001).
4. P. A. Rodnyi, S. B. Mikhrin, P. Dorenbos, *et al.*, Opt. Commun. **204**, 237 (2002).
5. P. A. Rodnyi, C. W. E. van Eijk, A. N. Mishin, *et al.*, Proc. SPIE (2002) (in press).
6. S. Huang, X. Wang, R. S. Meltzer, *et al.*, J. Lumin. **94**–**95**, 119 (2001).
7. P. A. Rodnyĭ, S. B. Mikhrin, and A. N. Mishin, Pis'ma Zh. Tekh. Fiz. **26** (15), 72 (2000) [Tech. Phys. Lett. **26**, 678 (2000)].

Translated by P. Pozdeev

Technical Physics Letters, Vol. 28, No. 12, 2002, pp. 994–996. Translated from Pis'ma v Zhurnal Tekhnicheskoĭ Fiziki, Vol. 28, No. 23, 2002, pp. 44–49.
Original Russian Text Copyright © 2002 by Bessolov, Zhilyaev, Kompan, Konenkova, Kukushkin, Mesh, Raevskiĭ, Fradkov, Fedirko.

High-Temperature Annealing of Bulk GaN Layers

V. N. Bessolov, Yu. V. Zhilyaev, M. E. Kompan,
E. V. Konenkova, S. A. Kukushkin, M. V. Mesh, S. D. Raevskiĭ,
A. L. Fradkov, and V. A. Fedirko

Ioffe Physicotechnical Institute, Russian Academy of Sciences, St. Petersburg, 194021 Russia
Institute of Machine Science, Russian Academy of Sciences, St. Petersburg, Russia
Moscow State Technological University "Stankin," Moscow, Russia

Received July 16, 2002

Abstract—The influence of high-temperature (1010°C) annealing in a flow of gaseous ammonia on the properties of bulk GaN layers, grown by chloride–hydride VPE and then separated from SiO_2 substrates, was studied using atomic force microscopy. The bulk (~360-μm-thick) epitaxial GaN layers were synthesized in two steps: a first stage of nucleation and growth at a low temperature (530°C) followed by epitaxy at a high temperature (970°C). It was found that the annealing increases the nanorelief height and activates the donor–acceptor recombination on the surface of a GaN layer grown at the lower temperature and decreases the intensity of photoluminescence from the layer grown at the higher temperature. *© 2002 MAIK "Nauka/Interperiodica".*

The heteroepitaxial growth of gallium nitride layers by vapor phase epitaxy (VPE) has been studied for more than three decades [1], but it was only recently established [2] that high-quality epitaxial layers can be obtained using a metalorganic chemical vapor deposition technique involving a low-temperature initial growth stage followed by high-temperature epitaxy. The development of a two-step process, whereby the main bulk material is grown at a high temperature above the initial thin layer nucleated and grown at a low temperature on a sapphire substrate, has allowed GaN layers of significantly improved quality to be obtained using a chloride– hydride VPE process [3].

By studying the properties of GaN layers grown in the low-temperature and high-temperature stages (LT-GaN and HT-GaN, respectively), it is possible to determine the influence the temperature of the process on the character of nucleation and epitaxial growth and to elucidate features of the growth mechanism. The aim of this work was to study the influence of high-temperature annealing on the properties of GaN layers, including both the LT-GaN layer formed under the conditions of three-dimensional nucleation in the course of heteroepitaxy and the HT-GaN layer grown under the conditions of homoepitaxy.

The heteroepitaxial growth of GaN was performed on preliminarily oxidized Si(111) wafers with a diameter of 50 mm rotated in a flow of hydrogen at a rate of 1 Hz. The ratio of the H_2/NH_3 component fluxes was 2 : 1. The samples were grown in two steps. In the first stage, a low-temperature buffer layer of GaN (LT-GaN) was grown by epitaxy at 530°C for 100 h, after which a 360-μm-thick HT-GaN layer was grown in the second stage of epitaxy proceeding for 3 h at a temperature of 970°C. After growth, the substrate was removed through dissolution in a standard etchant to leave a thick bulk GaN layer.

The bulk GaN layers obtained as described above were annealed for 4 h at 1010°C in the flow of an NH_3–$2H_2$ mixture. Then, the sample was studied from the LT-GaN side (exposed after removal of the substrate) using the atomic force microscopy (AFM) and photoluminescence (PL) methods (Fig. 1), while the HT-GaN side was only characterized using PL. The AFM investigations were performed on an NT–MDT instrument equipped with standard silicon nitride cantilevers. The PL spectra were excited by pulsed radiation of a nitrogen laser operating at λ = 337 nm and a pulse duration of 6 ns. The measurements were performed at liquid nitrogen temperature.

A comparative analysis of the AFM images showed that, immediately after removal of the Si substrate, the nanorelief height *h* on the LT-GaN surface did not exceed 10 nm. After high-temperature annealing of the sample, the relief height *h* increases by a factor exceeding 10 (Fig. 2). The PL measurements on the sample surface from which the substrate was removed showed

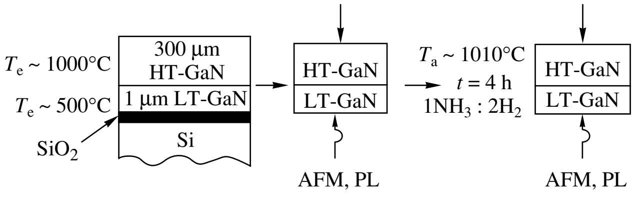

Fig. 1. Schematic diagrams illustrating the preparation (epitaxial growth), characterization (AFM, PL), and treatment (annealing) of the LT- and HT-GaN layers.

1063-7850/02/2812-0994$22.00 © 2002 MAIK "Nauka/Interperiodica"

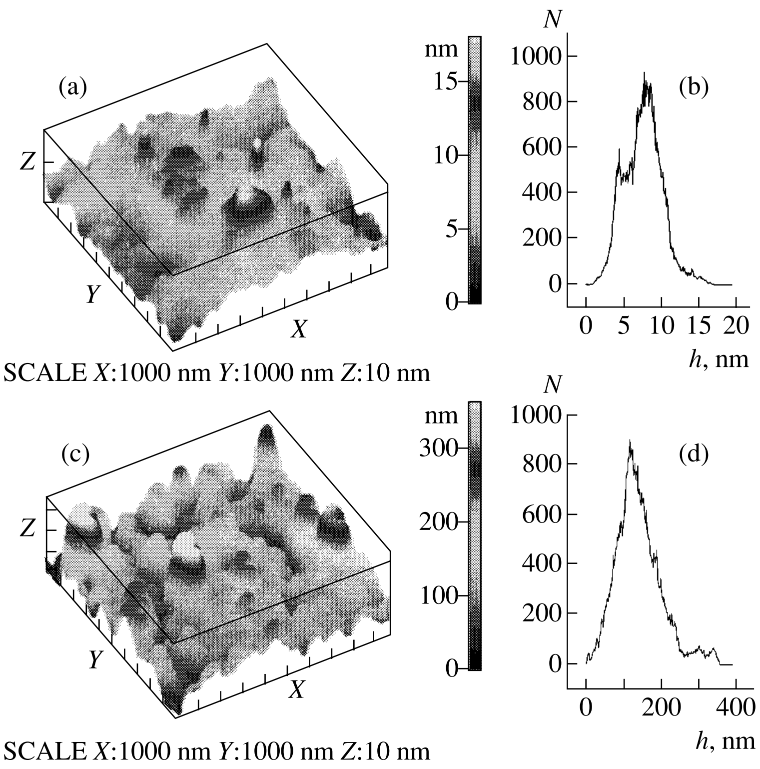

Fig. 2. (a, c) AFM profiles of the LT-GaN layer surface and (b, d) the GaN nucleus size distribution functions before (a, b) and after (c, d) high-temperature annealing of the samples.

that the photon energy at the maximum of the PL spectrum of LT-GaN was $h\nu = 3.46$ eV (at 80 K). This peak is probably related to the interband recombination process. After the high-temperature annealing, the PL intensity increased and the position of the emission maximum shifted toward longer wavelengths, up to a quantum energy of $h\nu = 3.28$ eV (80 K). The PL band at $h\nu = 3.28$ eV is attributed to the donor–acceptor recombination (Fig. 3a).

The PL measurements on the surface of the bulk epitaxial layer showed the maximum emission to take place at $h\nu = 3.46$ eV (80 K) both before and after the high-temperature annealing, while the intensity of this band somewhat decreased upon this treatment (Fig. 3b). Prior to the annealing, the PL intensity of HT-GaN was several times greater than that of the LT-GaN layer.

In order to explain the results presented above, let us consider features of the nucleation and growth of GaN layers. As is known for the heteroepitaxy of GaN from a vapor phase on a foreign substrate (sapphire, Si), the film is nucleated as result of a chemical reaction between gallium chloride and ammonia, which leads to the formation of three-dimensional islands with an average size of ~10 nm [4]. An analysis of the AFM images showed that the height of a nanorelief exposed on the LT-GaN surface after removal of the Si substrate is 4–8 nm, which corresponds to the size of islands representing the GaN nuclei (Fig. 2a). Apparently, the nucleation of GaN at a low temperature has a disordered character. During the subsequent annealing at $T_a = 1010°C$ in gaseous ammonia, the amorphous nuclei transform toward stoichiometric composition, i.e., toward of healing excess structural defects in the GaN structure. Under high-temperature conditions, the nuclei become involved in mass exchange. As a result, smaller nuclei tend to disappear and coarse ones grow so that the height of the surface nanorelief increases by one order of magnitude to reach 100–200 nm (Fig. 2b).

The PL spectra of LT-GaN layers measured after removal of the Si substrate were characterized by a relatively low emission intensity. The PL band maximum observed at $h\nu = 3.46$ eV (80 K) probably corresponds to the interband recombination of the minority charge carriers. The high-temperature annealing leads to a shift in the PL peak position by 0.18 eV toward longer wavelengths: $h\nu = 3.28$ eV (80 K). This value almost coincides with that previously reported by Katsavets *et al.*, $h\nu = 3.29$ eV (10 K) [5], and attributed to the recombination of nonequilibrium electrons and holes localized on the acceptor levels. It should be noted that the level at $E_c = 0.18$ eV was also reported in [6], where it was attributed to nitrogen defects.

Apparently, the initial growth stage involves the formation of an LT-GaN island layer, the luminescent properties of which are determined by the mechanism of interband recombination. The high-temperature annealing of this layer leads to activation of the donor–

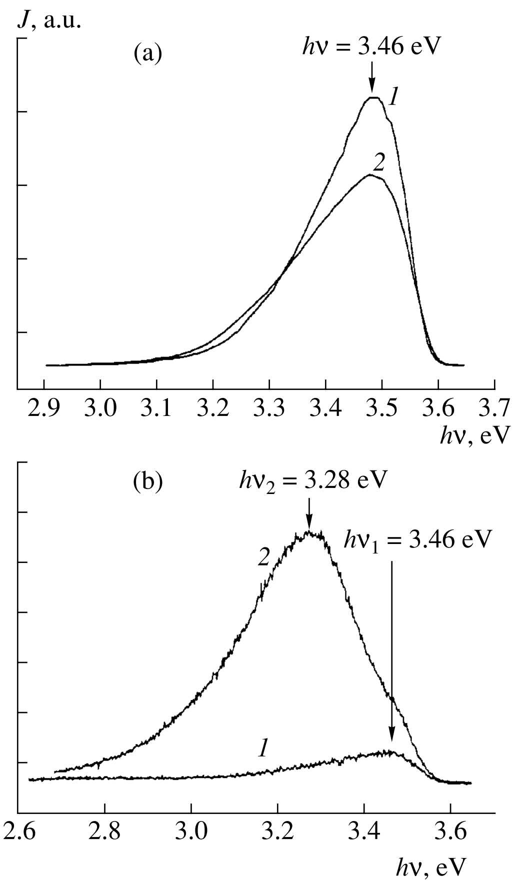

Fig. 3. The PL spectra of (a) HT-GaN and (b) LT-GaN layers (*1*) before and (*2*) after high-temperature annealing.

acceptor recombination mechanism (Fig. 3b). Further layer growth under high-temperature epitaxy conditions is controlled by the chemical reaction of GaN synthesis, which provides for the formation of rather perfect layers with a dislocation density of $\sim 10^8$ cm^{-2}. Annealing of the HT-GaN layer in gaseous ammonia at a temperature close to that of the epitaxial growth does not change the PL peak position but decreases the PL intensity. This is probably due to the structural defects, whose appearance is related to the relaxation of stresses (developed in the substrate–film system) in the course of prolonged annealing and subsequent cooling (Fig. 3a).

The observed difference in behavior of the LT- and HT-GaN layers subjected to high-temperature annealing is related to the different nature of these layers. The LT-GaN layer was formed by three-dimensional nucleation of GaN islands in the course of heteroepitaxy on the oxidized silicon substrate surface, while the HT-GaN layer was grown under the conditions of homoepitaxy at a sufficiently large distance (300 μm) from the heterojunction. The island layer is subject to considerable changes in the course of the high-temperature annealing.

Thus, the effect of annealing, which is more pronounced in the low-temperature than in the high-temperature GaN layers, is manifested by an increase in the surface nanorelief height and by activation of the donor–acceptor recombination mechanism in the GaN layer grown under the low-temperature epitaxy conditions.

Acknowledgments. The authors are gratefully for the support of the St. Petersburg Scientific Center of the Russian Academy of Sciences, the Ministry of Science and Technology of the Russian Federation (project no. 40.012.1.1.1153), and the Presidium of the Russian Academy of Sciences (project 17). One of the authors (E.V.K.) also received support from the Russian Foundation for Basic Research (project MAS-00-02-16989).

REFERENCES

1. H. P. Maruska and J. J. Tietjen, Appl. Phys. Lett. **15**, 327 (1969).
2. S. Nakamura, T. Mukai, M. Senoh, and N. Iwasa, Jpn. J. Appl. Phys. **31**, 139 (1992).
3. P. R. Tavernier, E. V. Etzkom, Y. Wang, and D. R. Clarke, Appl. Phys. Lett. **77**, 1804 (2000).
4. V. N. Bessolov, Yu. V. Zhilyaev, E. V. Konenkova, *et al.*, Pis'ma Zh. Tekh. Fiz. **27** (23), 60 (2001) [Tech. Phys. Lett. **27**, 1010 (2001)].
5. N. I. Katsavets, G. M. Laws, I. Harrison, *et al.*, Fiz. Tekh. Poluprovodn. (St. Petersburg) **32**, 1175 (1998) [Semiconductors **32**, 1048 (1998)].
6. Z.-Q. Fang, D. C. Look, P. Visconti, *et al.*, Appl. Phys. Lett. **78**, 2178 (2001).

Translated by P. Pozdeev

Technical Physics Letters, Vol. 28, No. 12, 2002, pp. 997–1000. Translated from Pis'ma v Zhurnal Tekhnicheskoĭ Fiziki, Vol. 28, No. 23, 2002, pp. 50–57.
Original Russian Text Copyright © 2002 by Dedkov, Kyasov.

On the Heat Exchange between a Probing Nanoparticle and a Surface through Near-Field Modes of a Fluctuational Electromagnetic Field

G. V. Dedkov and A. A. Kyasov
Kabardino-Balkarian State University, Nalchik, Kabardino-Balkaria, Russia
e-mail: gv.dedkov@mail.ru

Received June 27, 2002

Abstract—Heat exchange between a nanoparticle (representing the probe of a scanning microscope) and a solid surface in a range of distances from zero to several microns is considered in a relativistic approximation. It is shown that the role of the time lag increases with the conductivity of materials and the distance from particle to surface. The heat flux is always smaller than that obtained in the nonrelativistic approximation. Maximum heating is expected for high-resistivity materials. *© 2002 MAIK "Nauka/Interperiodica".*

In recent years, the problem of a fluctuational-dissipative interaction between a nanoparticle and a solid surface has drawn the attention of several groups of researchers [1–12]. The problem has two important aspects, related to calculation of (i) the normal and tangential forces acting upon the moving particle [1–8] and (ii) the heat exchange between particle and surface via the near-field modes of the electromagnetic field [7, 9–12]. In particular, it has been repeatedly pointed out that local heating of the surface by the point of a scanning probe microscope (SPM) can offer an effective means of modifying the surface [10, 11].

Volokitin and Persson [11] obtained expressions describing a heat flux between two flat surfaces spaced apart by a gap with width d or between a nanoparticle and a flat surface (in the absence of relative motion). The results of numerical calculations using these expressions lead to the rather unexpected (from the standpoint of physics) conclusion that a dominating contribution to the heat flux comes from the magnetic component related to the nonradiative modes of a fluctuational electromagnetic field, which appears when allowance is made for the time lag even at small distances between objects: $d \approx 1$ nm for two flat surfaces and $d \approx 10$ nm for a nanoparticle and a flat surface (both possessing metallic conductivity). More recently, the same researchers [8] made an analogous conclusion concerning the tangential dissipative force acting upon a body moving near a surface. In particular, it was asserted that the contribution of the magnetic field component to the friction force exceeds the contribution of the electric field calculated in a nonrelativistic limit without taking into account the time lag.

Below, we will demonstrate, based on our recent results obtained within the framework of a consistent relativistic description [13, 14], that the aforementioned conclusions made in [11] are incorrect. The reasons are as follows: (i) the contribution due to the magnetic component of the fluctuational electromagnetic field is always smaller than the contribution due to the electric field component and (ii) correct allowance for the time lag leads to a general decrease in the heat flux as compared to that in the nonrelativistic limit for distances between the two bodies ranging from zero to several microns.

In the problem under consideration, the role of the time lag is described by a dimensionless parameter $\xi = 4\pi\sigma z_0/c$, where σ is the conductivity of the surface material, z_0 is the distance from particle to surface, and c is the speed of light. For poor conductors ($\sigma \ll 10^{17}$ s^{-1}), we obtain $\xi \ll 1$; the region of applicability of a nonrelativistic approximation increases in inverse proportion to the value of σ. Eventually, this approximation is justified in most of the practically important cases encountered in the SPM operation. This agrees with our earlier conclusions [5] and with the results obtained in [10].

For normal metals ($\sigma \approx 10^{17}$ s^{-1}), $\xi \gg 1$ even for $z_0 >$ 1 nm and, hence, allowance for the time lag is necessary in principle. However, as will be shown below, the total heat flux $\dot{Q}$ related to both nonradiative and radiative modes of the electromagnetic field in this case is significantly smaller than that for the contact of two poor conductors (although $\dot{Q}$ can still exceed the blackbody radiation flux).

In contrast to [10, 11], where the heat flux was calculated for a static probe, we obtained the general relativistic formulas for determining the flux $\dot{Q}$ between a moving probe and a solid surface [13, 14]. Restricting our consideration to the case of an immobile probe ($V = 0$) and a nonmagnetic surface, let us first assess the net time-lag effect. In this special case, the formula for the heat flux can be written as

$$\dot{Q} = -\frac{2\hbar}{\pi}\int_0^\infty d\omega\,\omega\left[\frac{1}{\exp(\hbar\omega/k_BT_1)-1} - \frac{1}{\exp(\hbar\omega/k_BT_2)-1}\right]$$

$$\times \int\limits_{k>\omega/c} dk k^3\frac{\exp(-2q_0z_0)}{q_0}\left\{2\alpha''(\omega)\Delta_e''(\omega)\right. \quad (1)$$

$$\left. + \left(\frac{\omega}{kc}\right)^2\alpha''(\omega)[\Delta_m''(\omega)-\Delta_e''(\omega)]\right\} + \dot{Q}_{\mathrm{rad}},$$

$$q_0 = (k^2-\omega^2/c^2)^{1/2}, \quad q = (k^2-\varepsilon(\omega)\omega^2/c^2)^{1/2}, \quad (2)$$

$$\Delta_e(\omega) = \left(\frac{\varepsilon(\omega)q_0-q}{\varepsilon(\omega)q_0+q}\right), \quad \Delta_m(\omega) = \left(\frac{q_0-q}{q_0+q}\right), \quad (3)$$

where z_0 is the distance from particle to surface; $\alpha(\omega)$ is the particle polarizability; $\varepsilon(\omega)$ is the surface permittivity; T_1 and T_2 are the particle and surface temperatures, respectively; and $\dot{Q}_{\mathrm{rad}}$ is the contribution of radiative modes ($k < \omega/c$), which is expressed by the same integral as that for the nonradiative modes (the first term in Eq. (1)) with the following substitution:

$$\exp(-2q_0z_0)/q_0$$

$$\longrightarrow -\sin(2\sqrt{\omega^2/c^2-k^2}z_0)/\sqrt{\omega^2/c^2-k^2}.$$

In what follows, we will consider the probe as "hot" and the surface as "cold" by assuming that $T_1 = T$ and $T_2 = 0$. For the sake of simplicity, the probe and surface are assumed to be made of the same material. Note that, in the integrand of Eq. (1), the terms proportional to $\Delta_e''(\omega)$ are related to the contribution of the electric component of the electromagnetic field, while the terms proportional to $\Delta_m''(\omega)$ refer to the magnetic component (the *P*- and *S*-polarized waves in the notation of [10, 11]). The contribution related to the time lag is determined by the second term (in braces) of the integrand in Eq. (1).

Let us write the dielectric function as $\varepsilon(\omega) = 1 + 4\pi\sigma i/\omega$, introduce the new variable $t = kc/\omega$, and separate the internal integral in Eq. (1) into three integrals taken over the intervals $0 \le t \le 1$, $1 \le t \le \sqrt{4\pi\sigma/\omega + 1}$, and $t \ge \sqrt{4\pi\sigma/\omega + 1}$. In each of these intervals, the imaginary components of the functions $\Delta_e(\omega)$ and $\Delta_m(\omega)$ are uniquely expressed, provided the sign at the square root is selected appropriately:

(i) $0 \le t \le 1$

$$\Delta_e'' \approx \sqrt{\frac{2}{a}}(1+3t^2/4), \quad \Delta_m'' \approx \sqrt{\frac{2}{a}}(1+t^2/4), \quad (4)$$

(ii) $1 \le t \le \sqrt{a+1}$

$$\Delta_e'' \approx \frac{u}{2b}\frac{(4ab^2+au^2+4b^2-u^2)}{(u+b+u^2/4b)^2+(au-b+u^2/4b)^2}, \quad (5)$$

$$\Delta_m'' \approx \frac{u}{2b}\frac{(4b^2-u^2)}{(u+b+u^2/4b)^2+(b-u^2/4b)^2}, \quad (6)$$

(iii) $t \ge \sqrt{a+1}$

$$\Delta_e'' \approx \frac{2a}{4+a^2} + \frac{a(3a^2+4)}{(4+a^2)^2}\frac{1}{t^2}, \quad \Delta_m'' \approx \frac{a}{4t^2}, \quad (7)$$

where $u = \sqrt{t^2-1}$, $a = 4\pi\sigma/\omega$, and $b = \sqrt{a/2}$.

For a small metal particle with radius *R*, the polarizability is

$$\alpha(\omega) = R^3\frac{\varepsilon(\omega)-1}{\varepsilon(\omega)+2}. \quad (8)$$

Using formulas (3) and (4) and taking into account the condition that $\eta = \frac{2z_0k_BT}{c\hbar} \ll 1$, we obtain the following expression for the radiative contribution to $\dot{Q}$ (the minus sign corresponds to cooling of the probe):

$$\dot{Q}_{\mathrm{rad}} \approx -36\frac{\hbar R^3 z_0}{\sigma^{3/2}c^4}\left(\frac{k_BT}{\hbar}\right)^{15/2}, \quad (9)$$

where $\eta = 1$ for $z_0 = 4000$ nm, $\sigma \approx 10^{17}$ s^{-1}, and $T = 300$ K.

It would be of interest to compare the obtained $\dot{Q}$ values to those in a nonrelativistic approximation. Passing in Eq. (1) to the limit $c \longrightarrow \infty$, accomplishing integration, and taking into account that $k_BT/\hbar \ll 2\pi\sigma$, we obtain for normal metals at typical temperatures the same formula as in [10, 11]:

$$\dot{Q}_{\mathrm{nr}} = -\frac{3\pi}{40}\frac{\hbar R^3}{z_0^3\sigma^2}\left(\frac{k_BT}{\hbar}\right)^4. \quad (10)$$

Using formulas (9) and (10) and the parameters indicated above, we obtain $\dot{Q}_{\mathrm{rad}}/\dot{Q}_{\mathrm{nr}} = 1.5 \times 10^{-12}\left(\frac{z_0}{c}\right)^4\left(\frac{k_BT}{\hbar}\right)^{7/2}\sigma^{1/2} = 1$ for $z_0 \approx 800$ nm. At smaller distances, $\dot{Q}_{\mathrm{rad}} \ll \dot{Q}_{\mathrm{nr}}$. At the same time, it would be of interest to compare the quantity (10) to the blackbody radiation flux. Assuming that the cold surface area effectively heated by the probe equals approximately R^2 and using the Stefan law

$$\dot{Q}_{\mathrm{BB}} \approx -\frac{\pi^2}{60}\frac{\hbar R^2}{c^2}\left(\frac{k_BT}{\hbar}\right)^4, \quad (11)$$

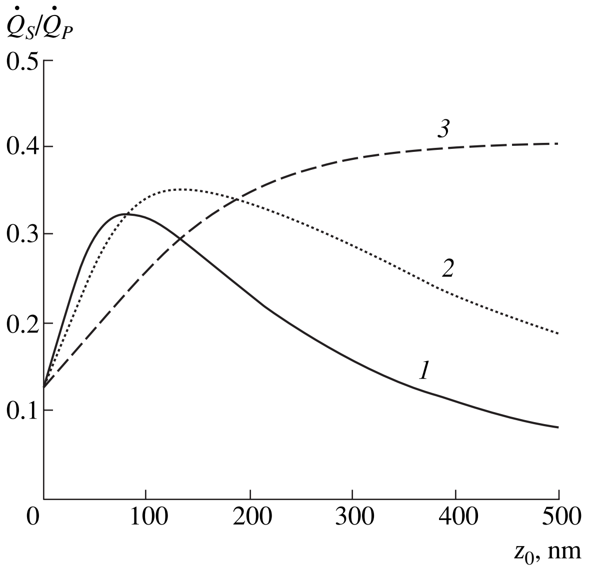

Fig. 1. Plots of the relative contributions to the heat flux due to magnetic $\dot{Q}_S$ and electrical ($\dot{Q}_P$) components of the fluctuational electromagnetic field versus distance z_0 from particle to surface for various values of the parameter $p = 2\pi\sigma\hbar/k_BT = 0.8 \times 10^4$ (*1*), 1.59×10^4 (*2*), and 7.95×10^4 (*3*).

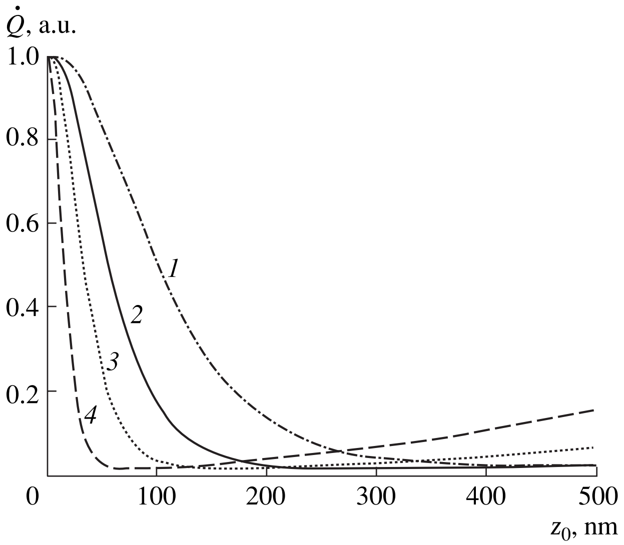

Fig. 2. Plots of the heat flux from probe to surface calculated with allowance for the time lag, normalized to the value determined in a nonrelativistic approximation (10), versus the distance z_0 from particle to surface for various conductivities and temperatures: (*1*) $\sigma = 10^{16}$ s^{-1}, $T = 300$ K; (*2*) $\sigma = 10^{17}$ s^{-1}, $T = 100$ K; (*3*) $\sigma = 10^{17}$ s^{-1}, $T = 300$ K; (*4*) $\sigma = 5 \times 10^{17}$ s^{-1}, $T = 300$ K.

we obtain for a normal metal $\dot{Q}_{\rm nr}/\dot{Q}_{\rm BB} \approx 13R/z_0^3$ (here, R and z_0 are expressed in nanometers). For $R \approx z_0 \approx 1$, this implies that $\dot{Q}_{\rm nr} > \dot{Q}_{\rm BB}$, although the excess is not very large. However, a tenfold decrease in the conductivity leads to a 100-fold increase in $\dot{Q}_{\rm nr}$.

Now, let us exactly estimate the contribution of the nonradiative modes in accordance with Eqs. (1)–(8). Figure 1 presents the results of a numerical calculation of the contributions to the heat flux due to the magnetic (S) and electric (P) field components. As the distance z_0 increases, the relative contribution of the S wave grows (but never exceeds unity). Figure 2 shows the total heat flux calculated with allowance for both radiative and nonradiative modes with respect to $\dot{Q}_{\rm nr}$. As can be seen, the time lag leads to a sharp drop in $\dot{Q}$ even at a distance of several dozens of nanometers. However, as the conductivity (or the temperature) decreases, the domain of applicability of the nonrelativistic approximation significantly increases.

At a distance on the order of several microns, the relativistic effects lead to a local increase in $\dot{Q}$ up to a level on the order of $\dot{Q}_{\rm nr}$ due to the linearly increasing radiative contribution ($\dot{Q}_{\rm rad}$). In this range of distances, formula (9) is no longer valid. However, according to Eq. (1) (see text), the rapidly oscillating term proportional to $\sin(2\sqrt{\omega^2/c^2 - k^2}\,z_0)$ in the integrand leads to truncation of the $\dot{Q}$ value. As a result, formula (10) can be used for evaluation of the upper boundary of the heat flux for distances from probe to surface ranging from zero to several microns.

From the standpoint of the optimum selection of contacting materials ensuring maximum surface heating, it is recommended to use high-resistivity materials with a conductivity on the order of $\sigma \approx k_BT/2\pi\hbar$. While we agree with this conclusion from [10, 11], we would like to emphasize the difference in the character of the dependence of $\dot{Q}$ on T (and on σ) [7, 12]: for $2\pi\sigma < k_BT/\hbar$ and $c \longrightarrow \infty$, Eq. (1) yields (cf. (10))

$$\dot{Q} = -\frac{4}{5}k_BT\frac{R^3}{z_0^3}\sigma. \tag{12}$$

Calculation of the heat flux from a moving probe requires separate consideration. However, even a nonrelativistic approximation reveals interesting features, for example, the possibility of a resonance heat exchange or heating of the hot probe (see [12] for details). In addition, formula (8) for the polarizability of a spherical metal particle requires correction for the contribution from electron gas screening (see, e.g., [15]).

REFERENCES

1. J. B. Pendry, J. Phys. C **9**, 10301 (1997).
2. M. S. Tomassone and A. Widom, Phys. Rev. B **56**, 4938 (1997).

3. B. N. J. Persson and Zh. Zhang, Phys. Rev. B **57**, 7327 (1998).
4. A. I. Volokitin and B. N. J. Persson, J. Phys.: Condens. Matter **1**, 345 (1999).
5. G. V. Dedkov and A. A. Kyasov, Phys. Lett. A **259**, 38 (1999).
6. I. A. Dorofeyev, H. Fuchs, and J. Jersch, Phys. Rev. B **64**, 35403 (2001).
7. G. V. Dedkov and A. A. Kyasov, Pis'ma Zh. Tekh. Fiz. **28** (8), 79 (2002) [Tech. Phys. Lett. **28**, 346 (2002)].
8. A. I. Volokitin and B. N. J. Persson, Phys. Rev. B **65**, 115419 (2002).
9. I. A. Dorofeyev, J. Phys. D **31**, 600 (1998).
10. J. B. Pendry, J. Phys.: Condens. Matter **11**, 6621 (1999).
11. A. I. Volokitin and B. N. J. Persson, Phys. Rev. B **63**, 205404 (2001).
12. G. V. Dedkov and A. A. Kyasov, Fiz. Tverd. Tela (St. Petersburg) **44** (10), 1729 (2002) [Phys. Solid State **44**, 1809 (2002)].
13. A. A. Kyasov, in *Proceedings of the International Workshop on Scanning Probe Microscopy-2002, Nizhni Novgorod, 2002.*
14. A. A. Kyasov and G. V. Dedkov, Nucl. Instrum. Methods (2002) (in press).
15. M. B. Smirnov and V. P. Krainov, Laser Phys. **9**, 943 (1999).

Translated by P. Pozdeev